

Description and Quantification of Debris Tongue Movement in a
Retrogressive Thaw Slump Using Aerial and Terrestrial
Photogrammetry

By

Ryan Parker

A thesis submitted to the Faculty of Graduate and Postdoctoral Affairs in partial fulfillment of
the requirements for the degree of

Master of Science

in

Geography,

Data Science Specialization

Carleton University

Ottawa, Ontario

© 2021

Ryan Parker

Abstract

Retrogressive thaw slumps can modify large areas of the landscape and pose a significant threat to linear infrastructure in the Arctic. There is little published information on how retrogressive thaw slump debris tongues develop. This thesis demonstrates a novel technique for combining information acquired from near-monthly structure-from-motion surveys and hourly frequency terrestrial photogrammetry to reconstruct the development of a retrogressive thaw slump over one thaw season. The study was conducted during the 2019 thaw season at Slump CRB, a retrogressive thaw slump located along the Dempster Highway in the Northwest Territories. It was found that material deposited in previous years did not move or change and the new debris tongue material flows over the previous deposits. In addition, two debris tongue development stages are outlined to describe the spatial and temporal variability of debris tongue movement and deposition in the early and late thaw season.

Acknowledgements

First off, I would like to thank my supervisors Murray Richardson and Stephan Gruber. Without your insight, guidance, and constructive criticism of my work this thesis would be a fraction of the quality that it is. I would also like to thank Derek Mueller and Rob Fraser for the time and effort they put in to review my work and provide meaningful feedback. I would like to thank the Northern Scientific Training Program for its financial contribution to my field work. I would also like to thank the Northwest Territories Geological Survey (NTGS) for financially supporting my work as well as sorting out most of the field work logistics, there's no way I could have done this work without that assistance. In particular, I would like to thank Steve Kokelj and Ashley Rudy from the NTGS for graciously allowing me to tag along during your field campaigns and guiding me through the sometimes hectic world of field work. I would also like to thank Jurjen van der Sluijs from the Northwest Territories Centre for Geomatics for designing and conducting the aerial photo surveys that were a part of this work. I would also like to thank him for providing me with an immense amount of practical knowledge when it comes to conducting SfM surveys, I think I learned more while chatting with you over beers than I ever could have by reading papers. I would also like to thank everyone at the Aurora Research Institute in Inuvik for being nothing but helpful, friendly, and inviting during my field work. I would like to thank Chris Burn and Peter Morse for sparking my interest in permafrost research and showing me it's so much cooler than just looking at frozen dirt. I'd especially like to thank my family as well as my partner Victoria for the constant support and reminders to quit slacking off. Finally, I'd like to thank all of my friends for your constant invites to go on ridiculous adventures often involving skateboarding, snowboarding, or rock climbing. It may have slowed down progress on my thesis, but it was well worth it, and it helped me keep what little sanity I have.

Table of Contents

Abstract	ii
Acknowledgements	iii
Table of Contents	iv
List of Figures	vi
List of Tables	viii
List of Acronyms	ix
1 Introduction	1
1.1 Context.....	1
1.2 Research Objectives	5
1.3 Approach.....	6
1.4 Thesis Structure	7
2 Background	8
2.1 Retrogressive Thaw Slumps	8
2.2 Structure-from-Motion	10
2.3 Topographic Change Detection.....	12
2.3.1 Difference of DEM.....	13
2.3.2 Multiscale Model to Model Cloud Comparison and the Precision Map Variant	15
2.4 Image Feature Tracking	20
2.5 Precise Position Derivation	21
3 Study Area.....	24
4 Methods.....	28
4.1 Field Instruments.....	28
4.1.1 GNSS Survey	28
4.1.2 Aerial Photo Surveys.....	28
4.1.3 SPi Cams	28
4.2 Field Methods	30
4.2.1 Aerial Survey	30
4.2.2 Terrestrial Survey Planning and Camera Deployment	33
4.3 Data Pre-Processing.....	34
4.3.1 GNSS Data.....	34
4.3.2 Aerial Survey	35
4.3.3 SPi Cam Lens Calibration	36
4.4 Aerial Structure-from-Motion Analysis.....	36
4.5 Change Detection Analysis	38
4.5.1 Aerial Survey M3C2-PM Analysis	38

4.5.2	SPi Cam PyTrx Analysis.....	40
5	Results.....	44
5.1	GNSS Surveys	44
5.1.1	PPP Base Station Corrections	44
5.1.2	PPK Corrected Positions	44
5.2	Aerial Surveys	46
5.3	SPi Cameras	50
5.3.1	Preliminary Viewshed Analysis.....	50
5.3.2	Field Complications	50
5.3.3	Comparison to Commercial Trail Cameras.....	53
5.4	M3C2-PM Analysis	54
5.5	PyTrx Analysis and Imagery Observations	67
6	Interpretation	72
6.1	Debris Tongue Development	72
6.1.1	Early Season Development	73
6.1.2	Late Season Development	74
6.2	Other Observations.....	75
6.2.1	Surface Property Changes.....	75
6.2.2	Volumetric Changes.....	76
6.2.3	Observations Related to the August 7 th Imprecisions.....	77
7	Discussion	79
7.1	Material Deposited in Previous Years	79
7.2	Debris Tongue Development	79
7.3	Limitations.....	81
8	Conclusion.....	83
	References.....	85
	Appendix A: Additional Figures	88
	Appendix B: SPi Cam Photos.....	99

List of Figures

Figure 1: A visual representation of the data processing workflow of this of this thesis. The M3C2-PM algorithm is a method of performing topographic change detection. PyTrx is a tool for performing time-lapse photogrammetry.	7
Figure 2: Annotated image of the upper portion of slump CRB, a medium-sized highly-active retrogressive thaw slump taken in July 2019	9
Figure 3: A visual representation of the M3C2 and M3C2-PM algorithms. Redrawn based on Figure 3a in Lague et al. (2013) and Figure 4 in James et al. (2017).	16
Figure 4: Illustration of why nonparallel vectors are not optimal for volume calculations	17
Figure 6: June 20th orthoimage and location of slump CRB.	27
Figure 7: Pseudocode for how the SPi Cam code operated. The orange box indicates the Sleepy Pi C++ code; the green box indicates the Raspberry Pi Python code; and the blue outline indicates the infinite loop the Raspberry Pi would repeat until it was shut off.	30
Figure 8: The flight path of the August 7 th aerial survey.	32
Figure 9: Locations of the PyTrx summary zones.	43
Figure 10: Precision map generated from the Monte Carlo analysis of the July 7 th survey.	48
Figure 11: Precision map generated from the Monte Carlo analysis of the August 7 th survey... ..	49
Figure 12: Viewshed analysis results showing optimal SPi Cam positions. The numbers correspond to the following cameras (ordered form N-S): 20-Jaws, 19-Largo, 10-Klebb, 15-Goldfinger, 11-Le Chiffre, 8-Dr No, 12-Blofeld, 6-Orlov, 16-Zorin, 7-Kristatos, 13-Kananga, 17-Drax, 9-Scaramanga.....	51
Figure 13: Timeline of live SPi Cams over the deployment period, this does not show if or when the cameras rotated. A shows the total number of live SPi Cams at a given time. B shows the timeline of each individual camera derived from the log files. Where the lines are in the upper position the camera was collecting data where they are in the lower position the camera was not collecting data. The vertical red lines indicate the dates the aerial surveys were conducted	52
Figure 14: A comparison of image quality between the SPi Cams and the Reconyx Ultrafire. .	53
Figure 15: Level of detection map for the June 5 th and June 20 th aerial survey change detection pair.	59
Figure 16: Level of detection map for the August 7 th and September 20 th aerial survey change detection pair.....	60

Figure 17: Significant topographic change that occurred between the June 5th survey and the June 20th survey. The numbered circles are the four summary zones. 61

Figure 18: Distribution of vertical topographic change pixel values within the slump extent for the change that occurred between the June 5th survey and the June 20th survey. Note that an exponential y-axis used..... 62

Figure 19: Distribution of vertical topographic change pixel values within the slump extent for the change that occurred between the June 20th survey and the July 7th survey. Note that an exponential y-axis used..... 62

Figure 20: Significant topographic change that occurred between the June 20th survey and the July 7th survey. The numbered circles are the four summary zones. 63

Figure 21: Significant topographic change that occurred between the July 7th survey and the August 7th survey. The numbered circles are the four summary zones..... 64

Figure 22: Distribution of vertical topographic change pixel values within the slump extent for the change that occurred between the July 7th survey and the August 7th survey. Note that an exponential y-axis used..... 65

Figure 23: Distribution of vertical topographic change pixel values within the slump extent for the change that occurred between the August 7th survey and the September 20th survey. Note that an exponential y-axis used..... 65

Figure 24: Significant topographic change that occurred between the August 7th survey and the September 20th survey. The numbered circles are the four summary zones. 66

Figure 25: The filtered velocity (bottom) and direction (top) of the displacement measured by PyTrx that occurred in summary zone three. The grey regions highlight the two movement events 70

Figure 26: The filtered velocity (bottom) and direction (top) of the displacement measured by PyTrx that occurred in summary zone four. The grey regions highlight the two movement events 71

List of Tables

Table 1: PPP corrected base station positions and associated errors.	44
Table 2: PPK corrected positions. The associated errors are in addition to the June 7 th PPP error. Aerial survey GCPs marked with * are the ones used for independent validation.....	45
Table 3: Aerial survey georeferencing errors assuming the GCP positions are stable in both time and space.	46
Table 4: Relative registration errors of the aerial survey change detection pairs.....	54
Table 5: Change metrics calculated from the M3C2-PM significant change results within the extent of the slump. Values in brackets are the 95% confidence intervals.....	56
Table 6: Change metrics for each summary zone M3C2-PM significant change results. Values in brackets are the 95% confidence intervals.	56
Table 7: A summary of the errors associated with the PyTrx analysis	68

List of Acronyms

DEM	Digital elevation model
DoD	Difference of DEM
GCP	Ground control point
GNSS	Global navigation satellite system
LoD	Level of detection
M3C2	Model to model multiscale cloud comparison
M3C2-PM	Model to model multiscale cloud comparison precision map variant
PPP	Precise point positioning
RTK	Real-time kinematic
PPK	Post-processed kinematic
RTS	Retrogressive thaw slump
SfM	Structure-from-motion
SPi Cam	Spatial Raspberry Pi camera
TCD	Topographic change detection
UAV	Unmanned aerial vehicle

1 Introduction

This thesis investigates the development of a debris tongue belonging to a highly-active medium-sized retrogressive thaw slump located in the Northwest Territories over the course of the 2019 thaw season. It builds on the current knowledge by improving monitoring techniques and employing emerging data processing techniques to produce data with high spatial and temporal resolution and quantified detection limits. This provides new insight on the characteristics and timing of the debris tongues movement.

1.1 Context

Retrogressive thaw slumps are thermokarst mass movement features which have the ability to grow larger than 20 ha and transport upwards of $1 \times 10^6 \text{ m}^3$ of sediment over their lifetime (Lacelle et al., 2015; van der Sluijs et al., 2018). Thermokarst activity has increased as the Arctic climate has warmed and become more wet (Kokelj & Jorgenson, 2013). With these climatic changes predicted to continue (IPCC, 2019), a deeper understanding of how retrogressive thaw slumps develop is required to understand how they will impact the environment.

Retrogressive thaw slumps can pose a significant threat to both the man-made and natural environment as they are able to modify large areas of the landscape. Some roads in the Arctic are particularly vulnerable to this threat as they cross regions favourable to retrogressive thaw slump development. These roads can be eroded due to back wasting of a retrogressive thaw slump headwall or become buried in debris tongue material. Both of these possibilities would not only be expensive to fix but could have a large impact on the communities that rely on the road for the resources to survive.

Past research on retrogressive thaw slumps has focused on headwall retreat rates and thermal regimes. Numerous studies have focused on the headwall portion of retrogressive

thaw slumps across the Western Canadian Arctic. Burn and Lewkowicz (1990) reported headwall retreat rates up to 16 m per year. Lacelle et al. (2015) reported average retreat rates of 7.2 to 26.7 m per year with the larger retreat rates associated with 'mega-slump' features larger than 20 ha. Wang et al. (2016) also reported a similar range of retreat rates, 8 to 15 m per year, however their data did not include any mega-slumps. Lantz and Kokelj (2008) reported that retreat rates from 1973-2004 were 1.4 times higher than rates from 1950-1973. Lewkowicz (1987) found that headwall retreat rates can be accurately predicted based on meteorological measurements including air temperature and wind speed. Additionally, correlations between rainfall measurements and both ordinal thaw slump activity measurements in the Aklavik Plateau (Lacelle et al., 2010) and ordinal measurements of debris tongue movement in the Peel Plateau (Kokelj et al., 2015) have been identified. Researchers have also focused on the thermal regime of these features and how the disturbances affect the surrounding permafrost. Burn (2000) reported that in a thaw slump near Mayo, Yukon the thermal disturbance caused by the slump was sufficient to degrade permafrost. Kokelj et al. (2009) investigated the polycyclic nature of lakeside thaw slumps using a two-dimensional thermal model. In addition to this, van der Sluijs et al. (2018) noted that the total change in volume between two digital elevation models (DEMs) collected on different dates can be a rough estimation of ground ice loss over that period.

Although the work mentioned above answers many questions about the processes involved in retrogressive thaw slump activity, a gap in the research still exists around the quantification and understanding of the debris tongue's movement (Kokelj et al., 2013). The main reason this gap in knowledge persists is that until recently, performing a study of this nature was very difficult. However, recent advances in technology and computing power have begun to reduce those barriers. An increase in quantitative data on this topic can contribute to the creation of numerical models describing retrogressive thaw slump development and

advanced early warning systems for the potential threat these features pose on infrastructure and human safety. In the case of highways these early warning systems would be able to notify road maintenance teams when a thaw slump is more likely to impact the road. This would allow them to pre-emptively close the road to prevent an accident and either excavate the debris tongue material from the road or fill in where the headwall has eroded.

Two studies have begun to address this knowledge gap by employing new methods related to photogrammetry. Kokelj et al. (2015) linked rainfall events to larger magnitude debris tongue pulses using time-lapse trail cameras, however, their measurement of movement was qualitative and therefore unable to describe the rate of material transport. van der Sluijs et al. (2018) used the COSI-Corr algorithm to obtain vectors describing the direction and magnitude of debris tongue movement over a 24 hour period from two aerial photo surveys. However, these vectors only provide a snapshot in time and cannot be extrapolated to describe how the debris tongue develops over a longer period. With the accessibility of advanced computing power, structure-from-motion (SfM) and time-lapse photogrammetry have become two promising techniques for filling in the quantitative information and knowledge gaps around the development of retrogressive thaw slump debris tongues.

SfM recreates a three-dimensional (3D) surface from a large number of overlapping two-dimensional (2D) images of the same object taken from multiple viewpoints (Westoby et al., 2012). In recent years it has been widely adopted by physical geographers as an inexpensive method of acquiring an accurate 3D topographic survey (Smith et al., 2015). For example, researchers are using SfM to monitor and detect change across a wide variety of environments including ice-marginal lakes (Mallalieu et al., 2017), fluvially eroded badlands (James et al., 2017), and permafrost terrain including retrogressive thaw slumps (Swanson & Nolan, 2018; van der Sluijs et al., 2018). The two most common methods of acquiring the image data for SfM involve either taking aerial photos, typically from an unmanned aerial

vehicle (UAV), or using multiple cameras positioned at different locations to photograph the same feature, possibly in time-lapse mode (Armstrong et al., 2018; Mallalieu et al., 2017).

UAVs are popular in for aerial SfM due to their relatively low cost and the ability for researchers to program a predetermined flightpath. The use of UAVs to conduct aerial photo surveys for SfM purposes over various types of terrain is well documented in the literature (e.g., Mancini et al. (2013); Lucieer et al. (2014); Turner et al. (2015); James et al. (2017); Swanson and Nolan (2018); van der Sluijs et al. (2018)).

Terrestrial SfM is a relatively new approach for detecting and monitoring change, which requires additional development. However, a refinement of this approach could lead to the automated acquisition of data for generating elevation models of a study site at the hourly or daily time scale. This method is limited by the ability to only survey smaller regions due to the viewing extent of the camera and the unpredictable drifting of the camera's internal clock that causes the cameras to capture photos at different times (Armstrong et al., 2018; Mallalieu et al., 2017; Smith et al., 2015). This becomes an issue when the subject of the photos is a dynamic feature because each camera will capture the feature in a slightly different state which causes errors when relating key points. Armstrong et al. (2018) and Mallalieu et al. (2017) used remote time-lapse cameras focused on a retrogressive thaw slump and a glacial ice margin respectively. Both studies were impacted by issues stemming from the internal camera clocks drifting over long periods of time as well as image compression issues which degraded the quality of the photos. A key conclusion put forth in both studies was the need to address this internal clock issue, including the suggestion to use GPS receivers in conjunction with cameras for time corrections. Such an approach has yet to be reported in the scientific literature.

An alternative to avoid the clock drift issues experienced in the SfM workflow is to use photogrammetry toolsets that are able to measure the displacement of a moving object between two images taken by the same camera. This time-lapse photogrammetry approach

mirrors the experimental set up of terrestrial SfM but because it does not compare images taken by separate cameras it is not limited by the camera drift issue. In addition, if this technique is applied to data from multiple cameras with overlapping fields of view there can be some assessment of uncertainty. How et al. (2020, 2018) demonstrated this time-lapse photogrammetry approach, by presenting velocity measurements of two tidewater glaciers measured from time-lapse cameras. A similar approach has yet to be applied to the quantitative study of retrogressive thaw slump dynamics.

1.2 Research Objectives

The aim of this thesis is to quantify the movement of a debris tongue belonging to a highly-active medium-sized retrogressive thaw slump. This will be done at the daily and monthly time scales and metre-level spatial scale over the course of one thaw season. This thesis will address two technical objectives (T1 and T2) designed to answer two research questions (R1 and R2).

- T1) Implement an uncertainty-based structure-from-motion change detection workflow to identify the stable and active regions of motion in a landscape and use the change detection results of near-monthly aerial photo surveys to identify larger scale movement and material deposition patterns.
- T2) Develop a terrestrial camera system and photogrammetry workflow to capture and quantify landscape movement during the periods between the near-monthly aerial photo surveys.
- R1) How does the material deposited by the debris tongue in previous years move or change?
- R2) How does the rate and timing of debris tongue movement as well as material deposition vary spatially and temporally during the thaw season?

1.3 Approach

This thesis has two sections, each addressing a research question whose results will describe the debris tongue behaviour at monthly and daily time scales (see Figure 1). One section will focus on the aerial photo surveys conducted at near-monthly intervals that cover the entire study site at a high spatial resolution and will comprise a spatially complete dataset. The data will then be processed using an uncertainty based SfM workflow followed by the M3C2-PM algorithm to produce confidence bounded metrics on changes in elevation and volume. These will then be used to analyze how the debris tongue evolved at a monthly time scale.

The other section will be focused on a proof of concept using the data collected from two of twelve custom built terrestrial time-lapse cameras. This data provides a significantly higher temporal resolution compared to the aerial photo survey data but only captures the development of the upper portion of the debris tongue and includes areas of 'no data' due to occlusion. This data will be processed using the PyTrx Python toolbox to produce vectors describing the displacement of material within the debris tongue at the hourly and daily timescale. These vectors will then be summarized to demonstrate how the debris tongue developed at the daily time scale.

An alternative plan for the data collected by the terrestrial cameras was to implement an SfM change detection workflow to produce metrics on the daily debris tongue development. However, after preliminary analysis, it was found that although this method had potential to produce usable results, the level of detection (LoD) calculated using M3C2-PM was approximately 1 m, too large to detect changes that occurred over the high frequency time scale of interest. Subsequently the data was processed using the PyTrx Python toolbox because it was able to produce more meaningful results.

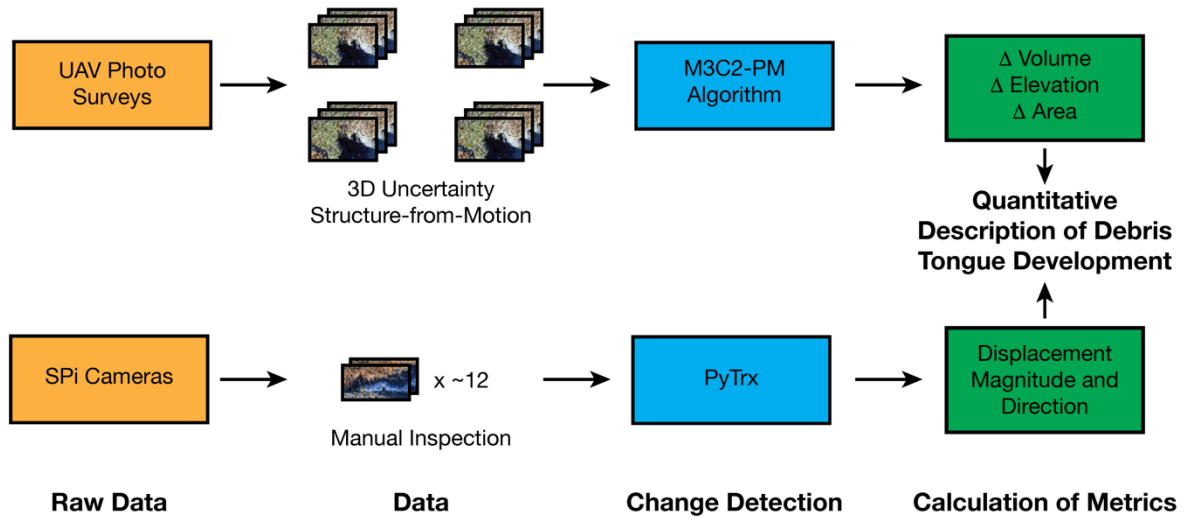


Figure 1: A visual representation of the data processing workflow of this of this thesis. The M3C2-PM algorithm is a method of performing topographic change detection. PyTrx is a tool for performing time-lapse photogrammetry.

1.4 Thesis Structure

This thesis is composed of eight chapters. Chapter 2 provides the background knowledge for the work being presented. Chapter 3 provides a detailed description of the study site and highlights why it is an optimal candidate for this study. Chapter 4 provides a description of the field work and data processing steps performed to produce the results presented in Chapter 5. Chapter 6 presents the interpretation of the key results and how they apply to the research objectives. Chapter 7 discusses the implications of this work and how it builds off the current knowledge base presented in the literature. Chapter 8 briefly summarizes the work and highlights the key points of this thesis.

2 Background

2.1 Retrogressive Thaw Slumps

Retrogressive thaw slumps are the most dynamic features in permafrost terrain (Burn & Lewkowitz, 1990). They are composed of a headwall and a debris tongue (Figure 2). The headwall section can be further subdivided into an upper active layer portion at the top of the headwall composed of ice-poor material (Lewkowitz, 1987). And, the headwall face that is often much larger and composed of ice-rich material that can often be classified as massive ice (Kokelj et al., 2013; Lewkowitz, 1987). The angle of the headwall can be anywhere from 20°-80° and often varies across a slump (Burn & Lewkowitz, 1990). The debris tongue section is a slurry-like accumulation of thawed headwall material (Kokelj et al., 2013). This slurry has the ability to mobilize and turn into a low angle mudflow if the material is sufficiently saturated (Burn & Lewkowitz, 1990; Kokelj et al., 2013).

Retrogressive thaw slumps can be initiated by a number of processes including mechanical or thermal erosion from fluvial processes, thermal subsidence, or mass wasting events (Lacelle et al., 2015). These all result in ice-rich permafrost being exposed and thawing while air temperatures are above freezing (Burn & Lewkowitz, 1990). As the thawing occurs so does progressive back-wasting of the exposed ice-rich face thus forming the headwall of the feature (Kokelj et al., 2013). The thawed headwall material typically has a high water content due to the high excess ice content of the headwall and begins to pool at the base of the headwall. As this material accumulates due to the continued thawing of the headwall it can begin to flow down slope (Kokelj et al., 2013). This movement of debris tongue material acts as a conveyor belt transporting newly thawed material away from the headwall base and ensuring that the headwall cannot be reinsulated by the thawed material. As the material moves away from the headwall it typically begins to lose momentum and will eventually come to a stop, at

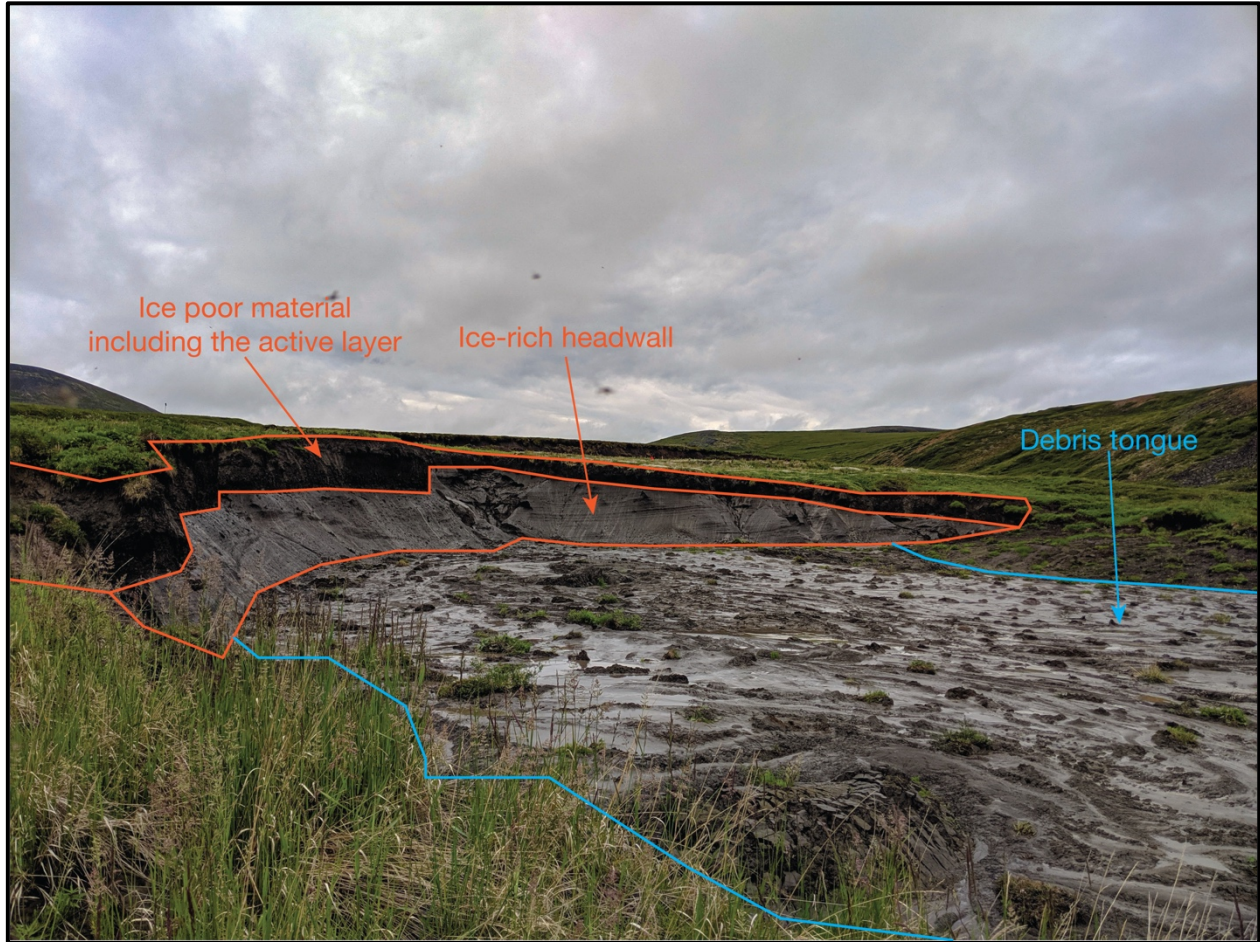


Figure 2: Annotated image of the upper portion of slump CRB, a medium-sized highly-active retrogressive thaw slump taken in July 2019

this point the soil material is deposited and will begin to stabilize. This process of thaw and material transport can continue throughout the thaw season for many decades resulting in developed features modifying vast areas of the landscape (Burn & Lewkowicz, 1990; Kokelj et al., 2013). It is possible for these features to stabilize and become dormant if the transport of thawed material slows, allowing for material to be deposited and reinsulate the headwall from the above freezing summer temperatures or if the availability of ice-rich material in the headwall is exhausted (Burn & Lewkowicz, 1990; Lacelle et al., 2010). If the former occurs, it is possible for the features to reactivate due to a number of reasons including rainfall, snow melt, or a change in thermal regime (Kokelj et al., 2009; Kokelj & Jorgenson, 2013).

2.2 Structure-from-Motion

There are six steps that make up the SfM technique used to produce a 3D model from raw image data. The first step involves detecting key-points within each image that are invariant to changes in scale, rotation, illumination, and the addition of image noise (Lowe, 2004). The scale invariant feature transform (SIFT) algorithm is most commonly used for this step as it is able to identify large numbers of key-points within an image and uses 128 vectors to describe each point's unique characteristics (Smith et al., 2015). The quality of the images greatly affects the ability of the SIFT algorithm to identify key-points. Therefore, the success and output quality of the entire SfM workflow is highly dependent on the quality of the input imagery (Westoby et al., 2012).

The second step is known as key-point correspondence and involves matching key points from different images. Typically, this is done by comparing the descriptive vectors of two key-points from different images and identifying pairs that have a 'distance-ratio' below a certain threshold. The 'distance-ratio' is defined as the ratio between the Euclidean distance of the descriptive vector nearest neighbour and the second nearest neighbour (Smith et al., 2015).

The third step involves filtering out geometrically inconsistent key-point matches. The random sample consensus (RANSAC) method is typically used for this (Smith et al., 2015). This method is conceptually similar to cross validation, where the minimum number of key-points required to fit a function are randomly selected and the function is fit to those points. The deviations from that function for all of the other key-points are then calculated. If there are enough suitable key-points whose deviations are below a threshold specified within the algorithm, then a least squares regression is applied to the function using all suitable key-points to improve the fit of the function. All unsuitable key-points whose deviations are above the set threshold are then labeled as erroneous and removed. If there are not enough suitable key-points then a new random sample is selected, the function is recalculated and the process

repeats (Fischler and Bolles, 2002). In the case of SfM, the function is an eight-point algorithm developed by Longuet-Higgins (1987) for reconstructing a scene from two projections or viewpoints.

The fourth step is where structure-from-motion gets its name and is also known as the bundle adjustment step (Smith et al., 2015). In this step the scene geometry, camera positions, and camera parameters are simultaneously estimated using the key-point correspondences and the redundancy of having a large number of overlapping images. The bundle adjustments work as a non-linear least squares model to minimize the distance between corresponding key points which reconstructs the surface and allows the other variables to be calculated (Snavely et al., 2006). This step produces a sparse point cloud made up of the relative 3D positions of all matched key-points across all of the images (Smith et al., 2015).

The fifth step is where the sparse point cloud is georeferenced and transformed from its relative 'feature space' to real-world coordinates (Snavely et al., 2006). There are two ways of doing this depending on how the photo survey was conducted: direct georeferencing, or the use of ground control points (GCPs). With direct georeferencing the 3D position of the camera at the moment of each image capture is resolved to a high degree of accuracy by combining a high precision differential GPS signal and inertial measurement unit data from the aircraft and onboard camera system (James et al., 2017). Therefore, georeferencing can be performed during the previous bundle adjustment step using the known camera positions, to produce a georeferenced point cloud without the need for GCPs (Smith et al., 2015). Alternatively, without direct georeferencing, high-contrast GCP targets are placed throughout the survey region and surveyed with a high precision and accuracy differential GPS system. These known point positions are then used to transform and position the sparse point cloud so that it can be given real-world coordinates (Lucieer et al., 2014; Smith et al., 2015).

The sixth and final step involves increasing the point density of the point cloud typically by at least two orders of magnitude. The most common method of performing this step is using a patch-based multi-view stereo (PMVS) image matching algorithm (Smith et al., 2015). These algorithms build out from the matched key-points identifying texture and pixel-level correspondences in multiple images and these correspondences are then used to generate new points surrounding the existing key-points. The clusters of new points surrounding the key-points continue to grow as the algorithm works outwards producing a dense point cloud (Furukawa and Ponce, 2010).

To summarize, key-points in each input image are first identified and described. Next, similar key-points from multiple images are matched using their descriptive vectors. Those matched key-points are then filtered for geometric consistency with any non-conforming key-point matches being removed. A bundle adjustment is then run which reconstructs the surface geometry as a sparse point cloud using the matched key-points. The sparse point cloud is then transformed from relative 'feature space' to a real-world coordinate system. Finally, the sparse point cloud is densified to generate the final point cloud.

2.3 Topographic Change Detection

Topographic change detection (TCD) is an analysis technique to identify and measure the difference between two topographic datasets. It is also important to quantify, using statistical methods, whether the observed differences are true changes or a product of errors in the datasets. This is determined using a universal or a spatially varying level of detection (LoD), wherein a change that exceeds the level of detection value is considered real (statistically significant) change (James et al., 2017; Lague et al., 2013). However, the ability to detect change is governed by multiple factors including the monitoring interval which is the time between the two topographic datasets were collected. For example, suppose the elevation of a given feature was changing at a rate less than 10 cm/day. If that feature is

monitored at a daily or sub-daily interval and the best possible change detection methods can only produce LoD values around 10 cm little to no change will be identified. But if the monitoring period were increased to a weekly interval then the elevation change of the feature would be higher than the LoD and therefore identified as statistically significant change. The ability to detect topographic change is therefore a function of (1) the data quality, which determines the LoD value(s); (2) the monitoring interval; and (3) the rate at which the feature is changing.

There are numerous methods using various algorithms but the most common is the Difference of DEM (DoD) method. There are, however, some issues related to the fact that DoD is a 2D analysis of a 3D change which can result in either an over or under estimation of the change that occurred. New TCD methods have been put forward in an attempt to improve upon the weaknesses of DoD. One of these is the model to model multiscale cloud comparison (M3C2) algorithm however this method makes invalid assumptions concerning the spatial autocorrelation of point cloud errors in SfM generated point clouds. A variant of this method incorporating maps of survey precision (M3C3-PM) has recently been presented which addresses this issue and is presented as a viable replacement for the DoD method.

2.3.1 Difference of DEM

The DoD method is the most commonly used method of TCD in earth sciences (Lague et al., 2013). It requires two DEM raster datasets that represent the topography of a location. The difference between the two datasets is then calculated on a pixel-by-pixel basis and the result is an estimate of the amount of elevation change that has occurred at each pixel. These DEMs are often generated by interpolating a point cloud generated from SfM or LiDAR and because of this the raster cell size limits the level of detail that can be retained within the input datasets (Lague et al., 2013).

One of the major issues with the DoD method is that it is 2D analysis of a 3D change and it assumes that all change occurs orthogonally to the surface, which in most cases is in the vertical direction. This is not realistic because the direction of change is dependent on the environmental process under investigation. But, due to the fact that the input datasets are 2D there is no way to improve this. Additionally, because the input datasets are 2D, only vertical measurement errors can be determined and the horizontal measurement error within the dataset is ignored (James et al., 2017). Because of this the validity of the results, especially in steep terrain, can be questionable as a small horizontal offset in steep topography can result in a large vertical change and can lead to incorrect conclusions on how the landscape is changing.

Another issue with the DoD method is that determining what change is statistically significant and what is not is often inadequate. This is also a product of the format of the input datasets. Typically, each raster dataset is given a constant vertical measurement error by comparing it to independently surveyed locations then using these errors from both datasets a LoD value can be calculated (James et al., 2017). This LoD can then be used as a threshold where all changes found to be larger than the LoD are statistically significant and all changes smaller are disregarded. This however is not optimal because it is well known that different surveying techniques perform better or worse in various terrains, for example SfM surveys have difficulty reconstructing the ground surface in regions of dense vegetation (Westoby et al., 2012). Therefore, although the blanket vertical error is helpful in determining the overall survey performance it does not highlight how the error varies spatially (James et al., 2017). This means that the given vertical error could greatly underestimate the actual vertical error for a specific region of the dataset causing the LoD to be set too low and “false-positive” change to be identified.

2.3.2 Multiscale Model to Model Cloud Comparison and the Precision Map Variant

The M3C2 method of conducting TCD was first presented in Lague et al. (2013). The paper presents the M3C2 algorithm for comparing two 3D point clouds and then goes on to show how it can be used to accurately quantify the topographic change occurring in a rapidly eroding bedrock river channel. The immediate benefit of this technique over the DoD method is that it removes the requirement to interpolate the datasets prior to the analysis thus preserving the detail of the datasets.

The M3C2 algorithm has two main steps. First, a vector perpendicular to the point cloud surface (normal vector) is calculated for every point (i) within the reference point cloud (S_1). This is done by fitting a plane through the points within a given radius ($D/2$) of the initial point (i). The orientation of this plane is then used to calculate a normal vector (N) in the positive direction (Figure 3-1). Because point clouds generated from terrestrial LiDAR and SfM have the ability to be far denser than 100 points per square meter (ppsm) it can be time consuming to calculate a normal vector for every point. To mitigate this, the point cloud is often subsampled to a regular spaced core point cloud with a density ranging from 1 to 10 ppsm that is intended to capture the relevant variability of the data set in a significantly reduced number of points. This core point cloud is used in the first step of the M3C2 algorithm to reduce computation time without sacrificing the quality of the results.

The second step is to calculate the Euclidean distances between the two point clouds of interest. For each point (i) the algorithm defines a cylinder which is centered on the point (i), oriented along the normal vector (N), and has a given radius ($d/2$). The points of both the reference (S_1) and the compared point cloud (S_2) falling within the cylinder are then used to calculate the average positions ($i_{1,2}$) and standard deviations ($\sigma_{1,2}(d)$). The distance along the normal vector (N) from the average reference position (i_1) to the average compared position (i_2) is then recorded as the M3C2 Euclidean distance at that location ($L_{M3C2}(i)$) (Figure 3-2). The

standard deviations ($\sigma_{1,2}(d)$) are a representation of surface roughness oriented along the normal vector (N). A point specific LoD oriented along the normal vector (N) can then be calculated using the standard deviations and an isotropic and spatially uniform value quantifying the registration error between the two datasets. Using this point specific LoD the significance of the M3C2 Euclidean distances can be determined.

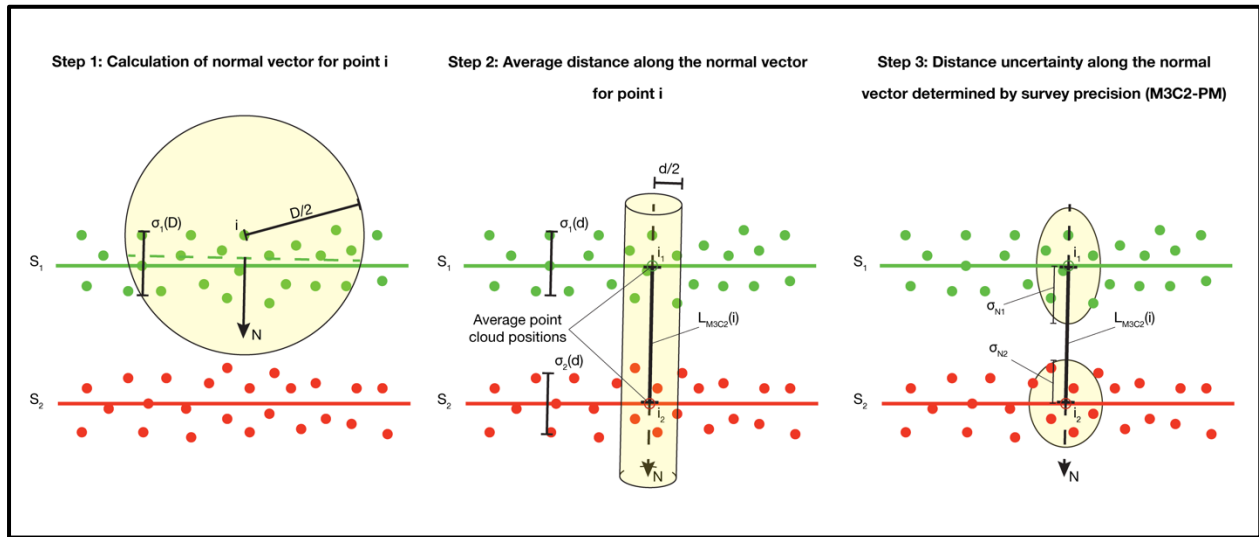


Figure 3: A visual representation of the M3C2 and M3C2-PM algorithms. Redrawn based on Figure 3a in Lague et al. (2013) and Figure 4 in James et al. (2017).

Although this is optimal for detecting topographic change, accurate estimations of changes in volume cannot be obtained from these Euclidean distances because the normal vectors are not parallel thereby resulting in a biased volume estimate (Bernard et al., 2020). For example, for a convex surface the normal vectors are diverging from one another. If these vectors were used to calculate a change in volume the results would underestimate the true change due to the omission of the shadow zones. In contrast, a concave surface would have the opposite issue. In this case the change in volume would be overestimated due to the overlapping normal vectors (Figure 4). In order to obtain an accurate estimation of the change in volume the M3C2 analysis must be run where the vectors are forced to be parallel with each other. In most cases a vertical-M3C2 analysis where the vectors are forced along the vertical axis resulting is most appropriate, and is in the point cloud equivalent of the DoD method

(Bernard et al., 2020; Lague et al., 2013). This is because the vertical-M3C2 analysis produces an accurate volume estimate, due to the fact that the vectors are parallel. It also provides the best representation the spatial distribution of volumetric change. Then for areas with significant change the result of this vertical-M3C2 can be used to calculate the volume of these significant changes.

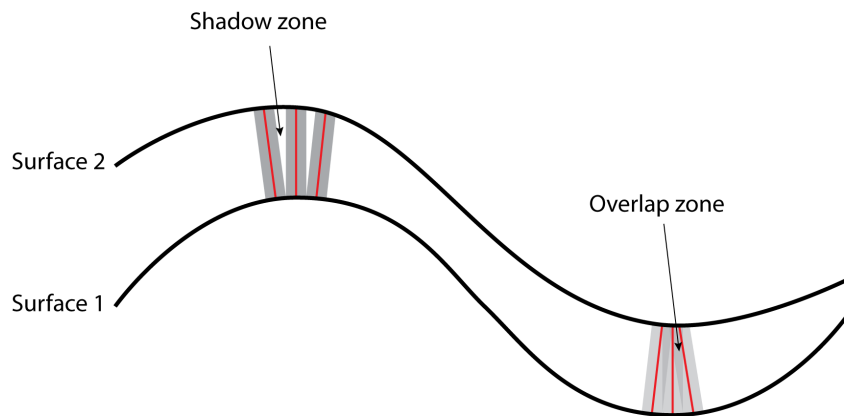


Figure 4: Illustration of why nonparallel vectors are not optimal for volume calculations

Compared to the DoD method of performing TCD using the M3C2 algorithm is superior for detecting significant topographic change for a number of reasons. First of all, it is a true 3D comparison and unlike DoD the change is not assumed to be vertical but measured normal to the local surface. Additionally, the LoD is spatially variable which is more realistic than a constant LoD for the entire dataset. The spatially variable LoD also allows for a better propagation of uncertainty in volume calculations operating under the assumption that the LoD is an estimation of uncertainty. For this, the LoD along the normal vector is used as the uncertainty of the vertical-M3C2 measurement, similar to Bernard et al. (2020). For point clouds generated by SfM, using the vertical component of the point cloud uncertainty obtained through a Monte Carlo analysis may provide a more realistic estimate of the volumetric uncertainty however, this could not be pursued in this thesis. Using the point cloud uncertainty

along the normal vector instead of the vertical component of point cloud uncertainty may result in an underestimated volumetric uncertainty in regions of steep topography.

The way the LoD is calculated is problematic when dealing with point clouds generated using SfM. When the M3C2 algorithm computes the standard deviations for the selected points within both point clouds ($\sigma_{1,2}(d)$) it is expected that the error of each point is independent of its surrounding points. This is more correct working with point clouds generated using terrestrial or aerial laser scanning but in SfM generated point clouds the errors are highly locally correlated. This means that the surface roughness calculated by the M3C2 algorithm does not accurately represent the uncertainty of point clouds generated from SfM (James et al., 2017).

A solution to this issue was presented in a paper by James et al. (2017). It involved incorporating rasterized datasets of point cloud precision in the x, y, and z directions into the M3C2 algorithm in order to obtain a more accurate spatially variable LoD. To do this the authors modified the SfM workflow to obtain estimates of photogrammetric uncertainty within the point clouds which could then be used to as a substitute for surface roughness in the M3C2 algorithm (Figure 3**Error! Reference source not found.**-3). Prior to point cloud densification the sparse point cloud is run through a Monte Carlo analysis. This analysis runs repeated bundle adjustments on the sparse point cloud randomly varying the positions of the cameras as well as the GCPs used in georeferencing the point cloud. The range in variation of each position is determined by the measured positional uncertainty of each camera or GCP. A copy of the point cloud is saved after each bundle adjustment and after a large number of iterations the uncertainty of the point cloud can be determined. By doing this the precision of each point within the point cloud is estimated using the uncertainty present in various aspects of the SfM workflow including camera position, camera orientation and network geometry. These point precisions can then be rasterized into a dataset which shows the spatial variability of survey precision in the x, y, and z directions. The point cloud densification step can then be

run, and the output dense point cloud can be used in the M3C2 algorithm. The survey precision raster datasets represent a 3D error ellipse and are used to calculate the positional uncertainty ($\sigma_{N1, N2}$) along the normal vector (N) at the average points ($i_{1, 2}$). This provides a more accurate representation of when calculating the spatially variable LoD and determining where the M3C2 Euclidean distances are statistically significant. Note that for M3C2-PM the cylinder with a radius $d/2$ is only used to calculate the average point positions ($i_{1, 2}$) and uncertainty along the normal vector is obtained directly from the survey precision datasets.

In addition to the M3C2-PM method providing accurate 3D results for TCD using SfM generated datasets, it also allows for evaluation the quality of the photo survey. The precision rasters generated from the Monte Carlo analysis provide the user insight into locations where the survey performs poorly. Using this information, the user can begin to investigate the potential causes of these performance issues such as low image overlap or key-point detection. With this insight, the planning for repeat surveys can be refined and the subsequent data collected will produce a more precise dataset.

In summary, the M3C2 algorithm is a superior method of conducting a TCD analysis compared to the DoD method. This is due to the fact that it is a true 3D comparison and uses a spatially variable LoD. Although, volume and vertical topographic change cannot be directly obtained from the M3C2 results, a vertical-M3C2 analysis provides the additional information required to produce confidence bounded volume estimates of the significant change. The calculation of the LoD is problematic when dealing with point clouds generated using SfM however, the M3C2-PM variant address this issue by using the results of a Monte Carlo analysis to calculate the LoD.

2.4 Image Feature Tracking

Time-lapse photography has been employed by researchers interested in how geographic features are changing over time (How et al., 2020; Kokelj et al., 2015; Mallalieu et al., 2017). Although many techniques exist, those employing photogrammetry and displacement analysis are currently producing the most promising results. One such procedure is to utilize the PyTrx Python toolbox created by Penelope How (How et al., 2018, 2020).

This procedure involves identifying key-points in two images, comparing the location of similar key-points, then using the key points identified on known stable features to correct for false-movement (How et al., 2018). This is a very similar process to the first two steps of the SfM technique however in this case the images are taken at significantly different times from the same camera. In order to accurately calculate the movement that occurred between the two images, the false-movement caused by motion of the camera platform needs to be accurately quantified (How et al., 2018). To do this PyTrx uses stable features such as mountain peaks to identify the false-movement between image pairs, then calculates a homography matrix which represents the transformation from the 2D image plane to 3D space (How et al., 2018). This is done by georeferencing the images using the extrinsic and intrinsic camera parameters (How et al., 2018). The extrinsic parameters are represented as a matrix describing the position and orientation of the camera in 3D space. This is calculated using the known position of the camera as well as the location of GCPs both in the images and in 3D space (How et al., 2018). The intrinsic camera parameters are also represented as a matrix and describe the conversion between 3D space and the 2D image plane. This matrix includes values such as focal length, the principal point, and camera skew. However, this assumes that the system is a pinhole camera and therefore radial and tangential distortion parameters must also be included to describe how objects are distorted by the camera lens (How et al., 2018). All of these intrinsic parameters can be calculated using a set of calibration images captured

by the camera. These reference images must be of an object with known geometry such as a black and white chessboard (How et al., 2018). Once both images have been georeferenced, the distance between corresponding key-points can be calculated in real-world coordinates. With these coordinate pairs, metrics describing the distance and direction of movement can be calculated, as well as velocity, if the time of image capture is known. In an effort to evaluate the accuracy of the calculated movement, the backtracked movement is also calculated by repeating the process and flipping the start and end images. This backtracked distance can be compared to the calculated distance and used as a reference for the accuracy of that velocity vector.

2.5 Precise Position Derivation

In both SfM and image feature tracking workflows, GCPs are required to transform the data into real-world space. To do this, the position of features captured in the images must be known to a high level of accuracy. Using modern surveying equipment and software it is possible to obtain positional information with centimetre level accuracy from global navigation satellite system (GNSS) data. The two most common methods of obtaining this information are by conducting a real-time kinematic (RTK) survey or a post-processed kinematic (PPK) survey (European Space Agency, n.d.; Wingtra, n.d.). Both survey methods require two L1/L2 GNSS receivers with one acting as a base station and the other acting as the rover (European Space Agency, n.d.). The base station is placed at a known point and continuously logs the position of that known point. The rover moves about, logging positions of unknown points and using the known position of the base station, the position of the unknown point can be determined to a high level of accuracy through differential correction. For RTK surveys this correction is done in real-time and therefore requires a constant stream of communication between the base station and the rover. In PPK surveys the corrections are done after the data from both receivers has been downloaded. Because of this there is no required communication between

the two GNSS receivers, thus simplifying field methods and making this the preferred method of conducting aerial surveys using a UAV (SenseFly, n.d.).

It is quite common for surveys to be conducted where there is no known position to place the base station and therefore no baseline to correct the rover position. A solution to this is to use a precise point positioning (PPP) algorithm to derive a precise position of the base station. This algorithm makes use of precise satellite orbits and time signals as well as the L1/L2 receiver observations to calculate the precise coordinates of the receiver (European Space Agency, n.d.). The precision of the calculated position is related to the length of time that the base station is left logging and can often take up to an hour to initially converge on a precise position (European Space Agency, n.d.). If PPP corrections are required to derive a base station position then an RTK survey cannot start until the PPP corrected position has been determined (Natural Resources Canada, n.d.). In this scenario PPK surveys are an alternative because the rover and base station can log independently without the known position of the base station. Then at a later date the rover data can be corrected after the PPP corrected position of the base station has been determined.

Although these methods are able to provide results with a high level of accuracy and precision, they are not without error. In turn, those errors influence the results of any analysis, and therefore must be described and dealt with accordingly. Here we refer to accuracy as a measure of how close a measured value is to the true position, and precision as a measure of the amount of uncertainty around a measurement. A PPP corrected base station position comes with estimated error values which describe the precision of the measured base station position, the true position is assumed to be somewhere within the quoted uncertainty. This provides a reference to the global coordinate system with a known uncertainty. Each position logged by a PPK or RTK rover also has associated precision values. However, these values describe the uncertainty of the rover position with respect to the position of the RTK/PPK base

station. Therefore, these error values do not have any reference to the global coordinate system. In order to relate the PPK/RTK rover positions to the global coordinate system, the true position of the base station must be known, or the PPP errors of the base station must be propagated.

3 Study Area

This thesis investigates Slump CRB, a highly-active medium-sized retrogressive thaw slump located near the Dempster Highway within the Peel Plateau physiographic region. The Peel Plateau is characterized by rolling hills incised by deep river valleys (Lacelle et al., 2015; O'Neill & Burn, 2017). The area is underlain by continuous permafrost with an ice content that is likely highly variable and not well characterized (Lacelle et al., 2015). Both the Permafrost Map of Canada (Heginbottom et al., 1995) and the more recent Ground Ice Maps of Canada (H. Brendan O'Neill et al., 2019) show low ground ice content for this region. However this is contradicted by field observations of ice-rich permafrost exposed in the headwalls of many retrogressive thaw slumps in the region (Lacelle et al., 2010; Malone et al., 2013). The geology of the region is predominately composed of shale from the Arctic Red Formation overlain by glacial till and moraine which can be up to 50 m thick (Duk-Rodkin & Hughes, 1992; Norris, 1985). There is no long term record of climatic data for the region but in the nearby hamlet of Fort McPherson between 1981 and 2010 the average yearly temperature was -7.3°C . The average maximum temperature of 15.2°C occurred in July and the average minimum temperature of -27.5°C occurred in January (Environment Canada, 2019). However O'Neill et al. (2015) showed that strong winter temperature inversions cause air temperatures on the plateau to be warmer than those in the lowlands surrounding Fort McPherson. The Fort McPherson climate data also shows that an average of 297.7 mm per year of precipitation fell between 1981 and 2010 with 145.9 mm of that falling as rain. July received the most precipitation with on average 46.4 mm falling as rain (Environment Canada, 2019). However, with the observed global and regional climate trends it is likely that more recent climate normal data would show warmer temperatures and increased rainfall (IPCC, 2019; Kokelj & Jorgenson, 2013). Many regional characteristics such as high ground ice content, moderate topographic

relief, and high summer precipitation create the optimal conditions for forming retrogressive thaw slumps and keeping them active (Kokelj et al., 2015).

The Dempster Highway connects Dawson, Yukon to Inuvik, Northwest Territories. It is approximately 740 km long and is the only all season road linking the Canadian Western Arctic to the rest of the country. The communities along the route rely on this transportation corridor for goods and services with Inuvik relying on the transportation of propane for power generation. Additionally, with the completion of the Inuvik to Tuktoyaktuk Highway in 2017, Canada's Arctic Coast is now accessible by road which has greatly increased tourism in the region. Approximately 40 km of the Dempster Highway runs through the Peel Plateau and has required significant maintenance due to permafrost related issues including retrogressive thaw slumps (O'Neill & Burn, 2017; van der Sluijs et al., 2018). A major closure to the Dempster Highway as a result of retrogressive thaw slump related damage could be disastrous for the communities that rely on that transportation corridor. Therefore, a full understanding of the features and their related processes that pose a threat to the highway are required to successfully implement a monitoring and early warning system.

Slump CRB is one retrogressive thaw slump that is in a position to cause damage to the Dempster Highway. It is located approximately 30 km from the Yukon border just north of the Dempster Highway within the Peel Plateau (67.181° N, 135.728° W). The main headwall curves from south to east facing and is composed predominately of massive ice. at the beginning of the 2019 thaw season the main headwall was divided into a small semi-stable upper headwall and a larger more active lower headwall, but over the 2019 thaw season the lower headwall retreated into the upper creating one large headwall. The debris tongue runs north to south towards the road and is constrained by a small pre-existing drainage valley. Two smaller sub-slumps with west facing headwalls composed of less ice-rich material have also developed on the east side of the main slump's debris tongue. These sub-slumps developed

sometime between 2015 and 2018 and have been steadily growing. The entire feature is approximately 550 m from the toe of the debris tongue to the back of headwall and approximately 200 m across at its widest point. The debris tongue is steadily approaching the Dempster Highway and as of September 2019 the toe of the debris tongue was approximately 220 m from reaching the road embankment (Figure 6 and Appendix A 1-4). This feature has become a concern for the Northwest Territories Geological Survey and the Transportation Department of the Northwest Territories Government because inundation or destruction of the Dempster Highway by the debris tongue has the potential to cause major disruptions.

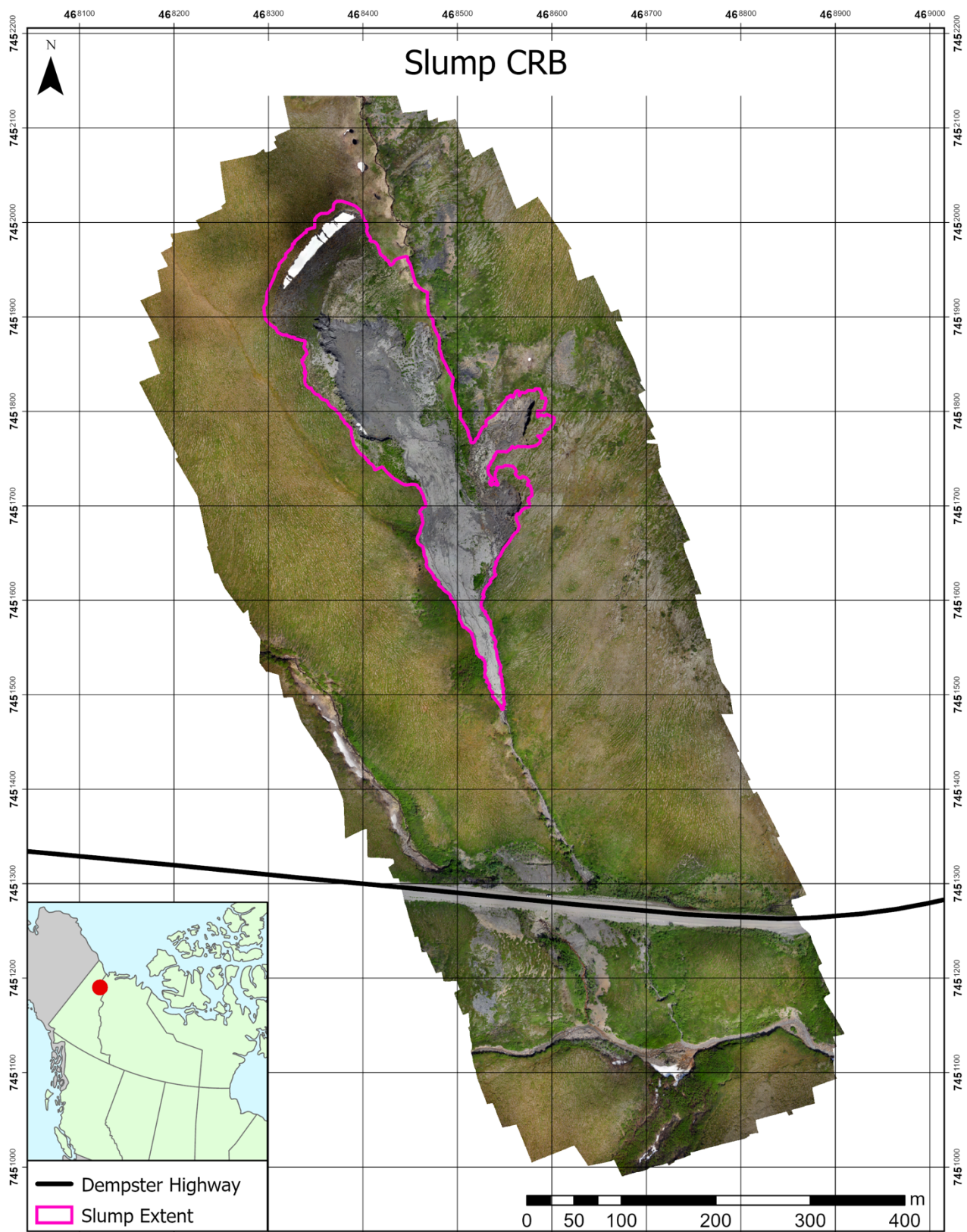


Figure 5: June 20th orthoimage and location of slump CRB.

4 Methods

4.1 Field Instruments

4.1.1 GNSS Survey

The GNSS survey points were collected using a Leica Geosystems CS20 field controller and GS14 GNSS receiver in PPK mode with another GS14 GNSS receiver set up as a base station less than a kilometer away.

4.1.2 Aerial Photo Surveys

The aerial photo surveys were conducted using a SenseFly eBee Plus RTK/PPK fixed wing drone equipped with a SenseFly SODA camera system. This system employed a 25.4 mm RGB sensor capable of capturing an image of 5472 x 3648 pixels. The system lens was a 10.9 mm fixed lens with a 2.8-11 F-stop range capable of global shutter speeds between 1/30 and 1/2000 s. The captured images were saved in JPEG format and the uncorrected position of the sensor from the onboard GNSS receiver was automatically added to the EXIF file of the image. Additionally, a Leica GS14 GNSS base receiver was also deployed during all drone flights with the exception of the August 7th flight where technical difficulties in the field prevented the receiver from establishing a reliable connection. Note that the base station was not placed in the same location for each photo survey, the implications of this will be discussed in a later section.

4.1.3 SPi Cams

The cameras used for the terrestrial photogrammetry portion of this project were custom built and named SPi Cams (Spatial Pi Cameras). Building custom cameras was the easiest and most cost effective method of overcoming the camera drift limitations outlined by Armstrong et al. (2018) and Mallalieu et al. (2017) while also improving image quality. The SPi Cams were constructed using a Raspberry Pi Zero W connected to a Raspberry Pi Camera

Module V2 chip with an which captured 2700 x 1800 pixel images. A Mikroelektronika GPS Click Board carrying a μ -blox LEA-6S positioning chip attached to an active GNSS antenna was also connected to the Raspberry Pi via the USB port. This provided the Raspberry Pi with positional data accurate to 2.5 m as well as UTC time from the satellites (MikroElektronika, n.d.). A Sleepy Pi power management Arduino board was connected to the Raspberry Pi using the general purpose input output (GPIO) pins in order to control the on/off cycles of the camera. Each camera was powered via USB from a 12V 9 Ah sealed lead acid battery connected to a charge controller. A 5 W solar panel was also connected to the charge controller to ensure the battery would remain charged while in the field. All of the components were placed in polycarbonate enclosure with an IP67 water and dust-proof rating with a clear door and a custom built lens port. To easily distinguish each camera and their data every SPi Cam was named after a villain from the James Bond franchise.

The cameras were programmed to boot on the 27th minute of every hour, acquire a GPS position, update the internal clocks of both the Raspberry Pi and the Sleepy Pi using the time from the GPS chip, take a photo at the beginning of the 30th minute, then shut down on the 31st minute of the hour. The camera would then sleep until the 27th minute of the next hour when the cycle would repeat. The cameras and GNSS chips used UTC time, so all dates and times subsequently reported are in UTC. The camera also wrote a log file that chronicled every action performed. In order for the SPi Cams to perform this cycle of tasks two scripts were written and uploaded to the controllers. The first was a C++ script instructing the Sleepy Pi Arduino board when to boot and shut down the Raspberry Pi. The second was a Python script detailing the steps the Raspberry Pi needed to take once it had booted. Figure 7 details how the two scripts interacted in order for the SPi Cams to perform their duties.

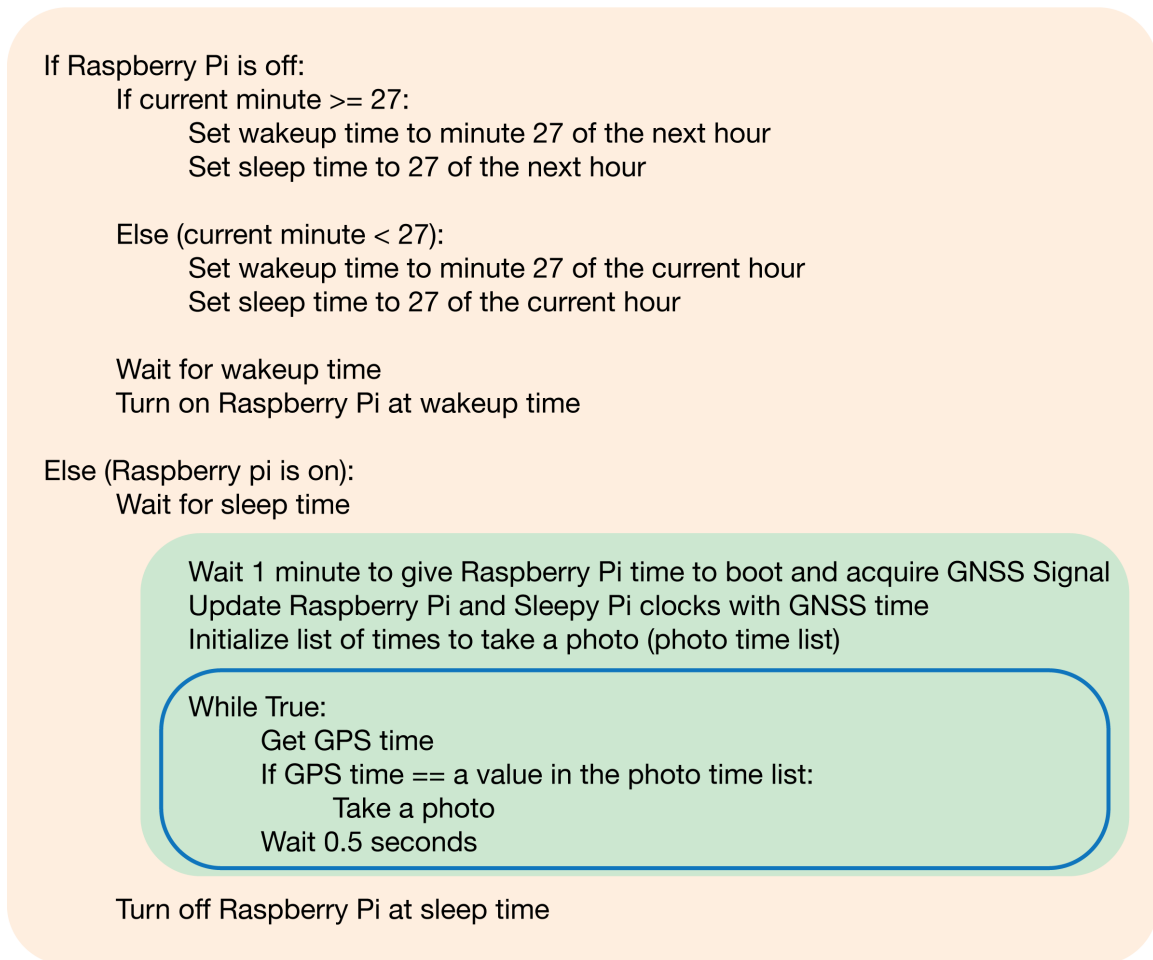


Figure 6: Pseudocode for how the SPi Cam code operated. The orange box indicates the Sleepy Pi C++ code; the green box indicates the Raspberry Pi Python code; and the blue outline indicates the infinite loop the Raspberry Pi would repeat until it was shut off.

4.2 Field Methods

4.2.1 Aerial Survey

Five aerial surveys of the study site were conducted on June 5th, 20th, July 7th, August 7th, and September 20th, 2019. Each flight was conducted by an employee of the Northwest Territories Government and followed similar data acquisition methods to van der Sluijs et al. (2018). All flights were conducted using the same automated flight plan generated using SenseFly’s eMotion 3 software. The flight was planned to provide ~80% overlap and sidelap as well as a ground resolution of ~2.3 cm/pixel. This resulted in a flight line spacing of ~25 m and a flight elevation of ~98 m above ground surface. In total, the flight consisted of 44

flight lines running east – west across the study site capturing ~25 ha and requiring ~ 32 minutes to complete (Figure 8). Each flight was flown by a licenced drone pilot in accordance with the Canadian Aviation Regulations (visual line of sight). During each survey (except August 7th) a Leica GS14 GNSS receiver was set up less than one kilometer away as a base station.

For the purposes of independent accuracy assessment as well as refining survey uncertainty seven GCPs were anchored into the surrounding stable ground within the aerial survey region. These GCPs were put out on June 5th and left in place for the entirety of the monitoring period to insure consistency between surveys. GCPs were surveyed on July 7th as a part of a larger GNSS survey of the study site.

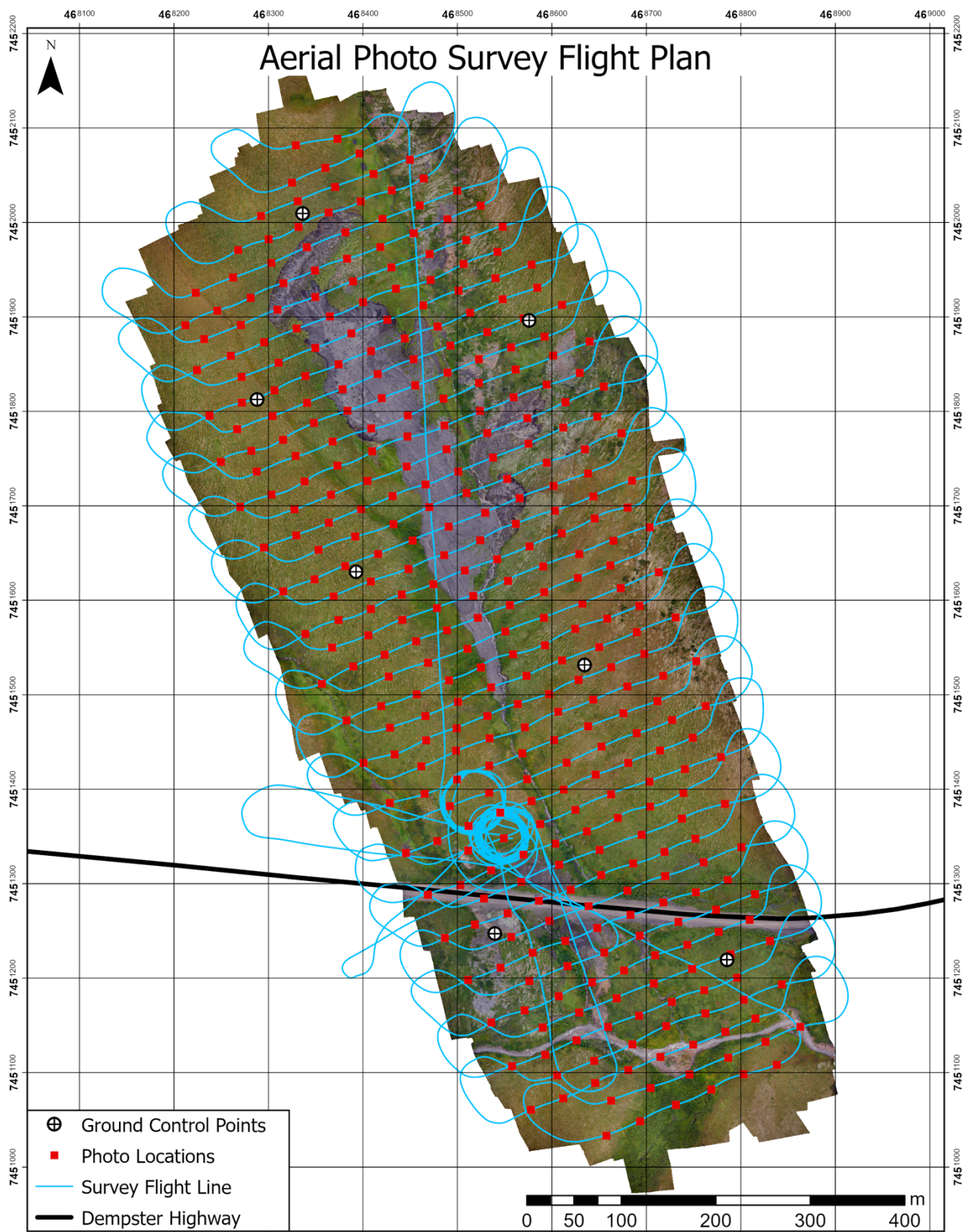


Figure 7: The flight path of the August 7th aerial survey.

4.2.2 Terrestrial Survey Planning and Camera Deployment

In order to streamline the work conducted in the field as well as ensure optimal results, the SPi Cam positions were determined prior to visiting the field site. This was by performing a viewshed analysis on a DEM of the study site from 2018. The horizontal and vertical field of view parameters calculated using the desired yaw and pitch of the camera and the sensor field of view in the x and y direction were input into the analysis as well as the rotation of the cameras. Using a manual trial and error process the position of each camera was determined to maximize photo overlap and area covered by more than six images. Once the SPi Cam positions had been determined the positions of 10 GCPs were located so that they were evenly spaced throughout the area of maximum photo overlap in areas of stable ground.

Each of the 12 SPi Cams was mounted on a 3/4 inch black steel pipe using mounting brackets fixed to the exterior of the camera case. A hole was then drilled approximately 90 cm into the ground and the camera post was placed into the hole and the void space was filled in with sand. The post locations followed the optimal camera positions determined in the viewshed analysis. However, due to the presence of bedrock in some locations the cameras needed to be moved a few meters to an area where a hole could be made for the post. After the cameras were mounted, they were all rotated to the approximate view angles determined by the viewshed analysis using a handheld compass. Two Reconyx Ultrafire trail cameras were also deployed with the SPi Cams to compare the performance of the SPi Cams to a similar commercial product. GCPs were then placed in stable ground on the opposite side of the slump in view of the SPi Cams. Each GCP was constructed out of a 15 cm bright orange PVC test cap screwed to a 60 cm tall wood stake. Each stake was hammered approximately halfway into the ground to ensure movement was minimal over the deployment period.

Once all the GCPs and SPi Cams had been deployed each was surveyed. The base of the GCPs were surveyed and the distance from the base to the centre of the GCP target was measured and recorded for post-processing. The same was done for each SPi Cam where the base of the mounting pole was surveyed and the distance from the camera lens to the ground was measured and recorded.

The above was conducted on July 7th, 2019. The SPi Cams were left to run and were checked on the next day to insure they were collecting data. Once this was confirmed they were left to run until September 20th, 2019 when the cameras were retrieved from the field and the data was collected.

4.3 Data Pre-Processing

4.3.1 GNSS Data

The base station data for June 6th, 20th, July 7th, and September 20th, 2019 was converted from Leica's proprietary format to RINEX format then uploaded to Natural Resources Canada's PPP web tool (Section 2.5). This returned PPP corrected positions with estimated horizontal and vertical errors which could then be used to PPK correct both the drone and rover positions. The process for correcting the drone positions in the aerial image EXIF tags is covered in the following section.

The rover data for July 7th, 2019 was PPK corrected in the open source RTLLIB software. The rover data was first converted from Leica's proprietary format to RINEX format. It was then input into RTKLIB along with the July 7th, 2019 base station data and the PPP correction for the base station obtained from Natural Resources Canada. The software then output a corrected position for the rover data; however, this was in the form of a line of every rover position collected on that date. To obtain corrected positions for the GCPs and SPi Cams, the time stamps for the beginning and end of data collection for each point were manually copied from the Leica Infinity software into a table. A Python script was then written

to parse through the rover position solution and extract every position collected between the start and end timestamps for each point and determined the point's position by averaging all of the positions extracted. The script then calculated the standard deviation in the x, y, and z directions for each point and converted it from decimal degrees to meters using trigonometry and the WGS84 semi-major axis radius of earth (a), flattening parameter (f) and the latitude component of the point's position (Equation 1-3). These positions and their associated standard deviations were then exported to a table for future use.

$$b = a - a \frac{1}{f}$$

Equation 1: Formula for calculating semi-minor axis radius.

$$\sigma_{x m} = \sigma_{x DD} * \frac{2\pi * a}{360} \cos(\text{latitude})$$

Equation 2: Formula for converting the standard deviation in the x direction from decimal degrees (longitude) to meters.

$$\sigma_{y m} = \sigma_{y DD} * \frac{2\pi * b}{360}$$

Equation 3: Formula for converting the standard deviation in the y direction from decimal degrees (latitude) to meters.

Due to software limitations the PPP errors were not able to be propagated through the PPK corrections and therefore this work operates in a local co-ordinate system relative to the July 7th base station position. In addition, the positions of the GCPs surveyed on July 7th, 2019 are assumed to be stable through time. Meaning no movement of these items occurred and data from different dates can be co-registered and compared.

4.3.2 Aerial Survey

After each aerial survey, the images as well as the flight log from the drone were downloaded and backed up. Once all of the surveys had been conducted, the data was processed. For each survey the log file of the drone was uploaded to Sensefly's eMotion 3 software along with the PPP corrected position of the base station. For the August 7th survey

the position of the Inuvik Canadian Active Control Station (CACS) was used because it was the closest reference point available. Next, the path of the folder containing the images collected by the drone was input into the software and the geotagged position of each photo was PPK corrected using the PPP base station position and the log file of the drone. The software then generated an Agisoft Photoscan project with the images, their corrected positions, and positional errors already imported.

4.3.3 SPi Cam Lens Calibration

To ensure the best quality results were produced using the PyTrx toolbox, each SPi Cam was calibrated after being retrieved from the field. For each camera, five images of a computer screen displaying a checkerboard pattern were taken from different viewpoints. These photos were then uploaded to Agisoft Lens which analyzed the photos and generated lens distortion parameters based on how the checkerboard pattern was distorted in the images. These parameters were then saved for each camera so that they could be applied during the processing steps.

4.4 Aerial Structure-from-Motion Analysis

The following procedure was run for each survey using the corrected data. First, the surveyed GNSS positions of the GCPs along with their uncertainties were imported into the project. Next, because both the image and GCP positional uncertainties were expressed in meters and the positions were expressed in decimal degrees, all positions were converted to the UTM Zone 8 N coordinate system. After this was done, the sparse point cloud was generated using a key point limit of 40,000 and a tie point limit of 5,000 and the accuracy parameter set to “High” (Section 2.2). Once this had been completed, the images that captured the GCPs could automatically be identified. Each image that captured a GCP was examined and the exact position of the GCP was manually identified. A copy of the Photoscan project

was then made so that the precisions of the point cloud could be determined without accidentally corrupting the original data.

In order to determine the precision of each point within the point cloud, the methods published in James et al. (2017) were followed. This involved using a Python script to run a Monte Carlo analysis where, for each iteration, the positions of the cameras and ground control points were randomly varied over a Gaussian distribution using the positional uncertainty to determine the range. It then conducted a bundle adjustment to determine the location of each point within the new point cloud with the modified camera positions, saved the point cloud, and repeated for the remaining iterations. In order to gain an insight into the overall accuracy of the survey, GCPs 3, 6, and 7 were removed from all analyses so that they could be used as independent check points. Using the remaining four GCPs, 4,000 Monte Carlo iterations were run which took approximately 24 hours for each survey. Once the Monte Carlo script had completed, the results were compiled and three raster datasets with 1 m resolution were output showing the survey precision in the x, y, and z directions (Section 2.3.2). This was done using SfM_georef, a software developed by Mike James (James et al. (2017))

The original Photoscan project was then reopened and the dense point cloud was generated at the “Ultra High” quality setting with depth filtering set to “Aggressive”. The dense point cloud was then exported so that it could be used in the change detection analysis. Additionally, the dense point cloud was used to generate a 1 m resolution DEM of the study site as well as an orthophoto. The positions of GCPs 3, 6, and 7 were manually identified from the orthophotos and DEM of each survey and along with the known PPK corrected positions the overall survey georeferencing errors were calculated using Equation 4 where σ , in this case, represents the average difference between the known PPP corrected position and the position of the GCP in the orthophoto in a given direction. With the exception of the July 7th photo survey, the base station of the photo survey was not in the same location as the base station

when the GCPs were surveyed. This complicated the georeferencing step because the GCPs and the photo positions were in two separate but very similar local coordinate systems. However, because four GCPs were used to during the generation and georeferencing of the point cloud the georeferencing error can be interpreted as such: The positional accuracy of the photo survey with respect to the local coordinate system of surveyed GCPs. In addition, it can be assumed that the photo positions are a significant contribution to the georeferencing error.

$$reg = \sqrt{\sigma_x^2 + \sigma_y^2 + \sigma_z^2}$$

Equation 4: Formula for calculating georeferencing and/or registration error in 3D. Adapted from Hugenholtz et al. (2016) Equation 2

4.5 Change Detection Analysis

4.5.1 Aerial Survey M3C2-PM Analysis

Using the point clouds generated from the five aerial surveys four separate change detection analyses following the same methods were conducted using the point clouds generated from consecutively dated aerial surveys. The first change detection analysis was conducted using the June 5th data as the reference cloud and the June 20th data as the compared cloud. The second was conducted using the June 20th data as the reference cloud and the July 7th data as the compared cloud. The third was conducted using the July 7th data as the reference cloud and the August 7th data as the compared cloud. And the fourth was conducted using the August 7th data as the reference cloud and the September 20th data as the compared cloud.

For each analysis the pair of point clouds were imported into the CloudCompare software and the M3C2 plugin was run with the clouds input as reference (S_1) and compared (S_2) respectively (Section 2.3.2). In order to cut down processing time the reference cloud was subsampled to a regular point spacing of 0.25 m. The normal vectors for each point were calculated using a plane fit to the points within a 1 m diameter ($D = 1$ m). The cylinder used to

calculate the difference between the two point clouds for each point was given a diameter of 0.5 m ($d = 0.5$ m). The M3C2 plugin took approximately 6 hours to analyze each pair of point clouds and output a new point cloud displaying the Euclidean distances between the two input point clouds. The M3C2 point cloud was then saved as a tab delimited text file as so that it could be read by SfM_georef. In addition to this, a vertical-M3C2 analysis was conducted using the same parameters and the output was saved as a 1 m resolution raster for volumetric calculations later on. The M3C2-PM calculation was then run in SfM_georef using the tab delimited M3C2 results, an image registration error (reg) of zero, and the precision maps generated from the Monte Carlo analysis of the two input point clouds to produce a new M3C2-PM point cloud. Image registration was assigned as zero because a bug was identified in the M3C2-PM calculation performed by SfM-georef. The bug caused the estimations of surface roughness along the normal vectors ($\sigma_{1,2}(d)$) to be the only values correctly exported to the M3C2-PM point cloud. A Python script was written to recalculate the M3C2-PM results using the M3C2 point cloud and the M3C2-PM point cloud both rasterized to a 1 m resolution to match the resolution of the precision rasters generated from the Monte Carlo analysis. This script took the original 'M3C2 Distance' field from the rasterized M3C2 point cloud; the precision fields 'Sigma N1' and 'Sigma N2' from the rasterized M3C2-PM point cloud, which represented the surface roughness along the normal vectors for both input point clouds; and the registration error between the two input point clouds. The registration error for each pair of point clouds was calculated by using Equation 4 and the positions of GCPs 3, 6, and 7 determined from the orthophotos of each survey. In this case, σ in Equation 4 represents the average difference between the GCP positions of the reference dataset and the compared dataset for a given direction. The python script then used Equation 5 to calculate the level of detection for each pixel.

$$LoD_{95\%} = \pm 1.96 \left(\sqrt{\sigma_{N1}^2 + \sigma_{N2}^2} + reg \right)$$

Equation 5: Formula for calculating a spatially variable level of detection. (James et al., (2017), Equation 2)

For each pixel, the absolute value of M3C2 distance was compared to the LoD for that pixel. If the M3C2 distance was larger, the change was deemed significant, otherwise the change was insignificant. This significant change raster was then exported to be analyzed and used in figures.

Volume calculations of the significant changes that occurred within the extent of the slump were then calculated using the rasterized M3C2-PM and vertical-M3C2 results. This was done by first setting the pixels in the vertical M3C2 raster deemed non-significant by the M3C2-PM analysis to null, then calculating volume using the remaining vertical-M3C2 pixel values and the pixel area. The 95% confidence intervals for these measurements were calculated by using the M3C2-PM LoD pixel values as the uncertainty of each pixel. These uncertainties were then propagated through the volume calculation. Volume calculations were performed for each change detection pair within the extent of the slump as well as within the four summary zones used in the PyTrx analysis to allow for simple relations between the aerial and terrestrial photogrammetry sections of this thesis to be drawn.

4.5.2 SPi Cam PyTrx Analysis

For the PyTrx analysis, the data collected between July 7th and August 7th by SPi Cams Kristatos and Dr No was used. By using the two survey dates as start and end reference points and only two of the twelve cameras a proof of concept for this type of analysis could be conducted focusing on the accuracy and limitations of the technique. Time constraints did not allow for more than two cameras to be processed for this thesis.

For each SPi Cam the lens calibration parameter file was first converted from the Agisoft XML format to a text file that could be read by the PyTrx code. Next the images taken by each camera were manually inspected to ensure the camera did not move significantly. If

there were movement events, then the images were divided into sets where the camera stayed relatively stable. Once the images had been divided into sets, each set was manually inspected and any photos that were dark, blurry, or where the study area was obscured by fog were removed. Next a reference image was chosen for each image set and for that reference image velocity and stable-feature masks were created. This was done by manually tracing the stable or moving features in Adobe Photoshop and overlaying the traced shape as a white object on a black background. These black and white images were then exported and converted to single-band binary JPEG images. The pixel location of each GCP captured in the image was subsequently located and paired with the real-world coordinates of that GCP. These coordinate pairs were then compiled into a text file. This data along, with the 1 m resolution DEM generated from the July 7th aerial photo survey data, was input into the PyTrx workflow. This produced over 1000 sets of velocity vectors with real-world coordinates which were then exported as line shapefiles (Section 2.4). In order to easily evaluate and draw conclusions from the massive amount of information, the data within four regions was summarized. These summary zones were drawn out as circles with a radius of 10 m and placed at different locations within the debris tongue where different displacement rates were believed to occur at different times (Figure 9). For each summary zone the mean, median, standard deviation, and variance of displacement magnitude and the direction was calculated and exported.

Upon inspection this summary dataset contained large amounts of noise so two separate methods of filtering the data were conducted. The first method employed the locally weighted scatterplot smoothing (LOWESS) filtering method which used the nearest 5% of the data to calculate a smoothed trend. The second method was a manual filter based on two assumptions of the displacement characteristics. The first assumption was that the direction of displacement was always predominately south so any data with a mean direction not between 120° and 225° were removed. The other assumption was that mean displacement never

exceeded 3 m/hour so any displacement with a mean magnitude greater than that was also removed. This filtered data was then plotted and visually inspected to insure coherence between the datasets.

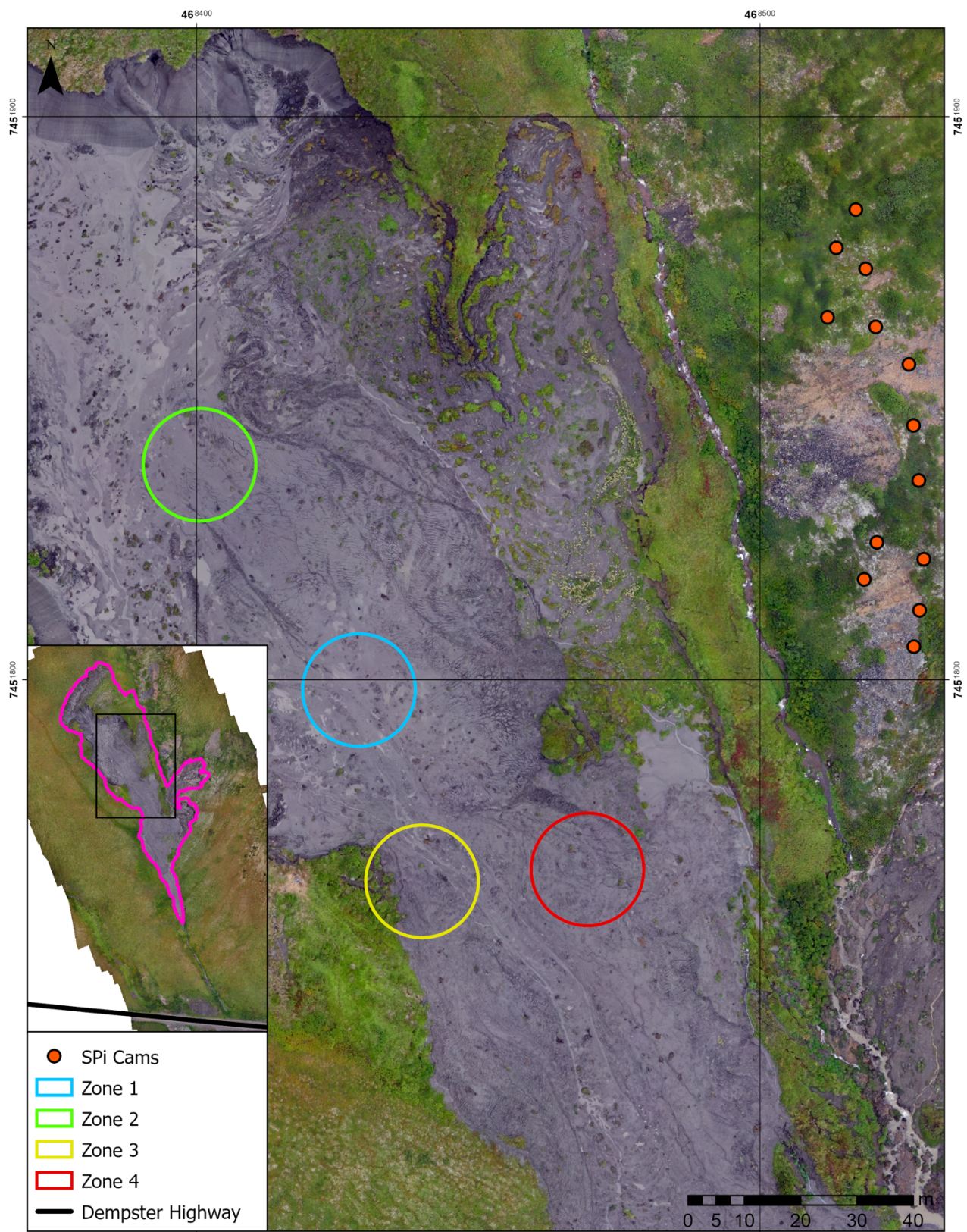


Figure 8: Locations of the PyTrx summary zones.

5 Results

5.1 GNSS Surveys

5.1.1 PPP Base Station Corrections

After the corrected base station positions had been received from the Natural Resources Canada PPP web tool, it was found that the horizontal errors were between 0.6 and 6.1 cm and vertical errors were between 1.9 and 5.1 cm. On June 20th the base station was only left logging for one hour and as a result it had the largest positional errors. The corrected base station positions as well as their associated errors can be found in Table 1.

Table 1: PPP corrected base station positions and associated errors.

Date	Latitude (deg)	Longitude (deg)	Elevation (m)	N/S Error (m)	E/W Error (m)	Elevation Error (m)
June 5 th , 2019	67.17760989	-135.72679504	576.142	0.008	0.013	0.022
June 20 th , 2019	67.17763538	-135.72683572	610.988	0.026	0.061	0.051
July 7 th , 2019	67.18122884	-135.73111697	575.944	0.007	0.008	0.019
Sept. 20 th , 2019	67.17760699	-135.72678443	575.923	0.006	0.011	0.020

5.1.2 PPK Corrected Positions

After the July 7th rover positions had been PPK corrected it was found that on average the positional errors of the SPi Cams were 0.004 m, 0.004 m, 0.005 m in the x, y, and z directions respectively. The average positional errors of the SPi Cam GCPs were found to be 0.005 m, 0.005 m, 0.017 m in the x, y, and z directions respectively. And, the average positional errors of the aerial survey GCPs were found to be 0.013 m, 0.012 m, 0.008 m in the x, y, and z directions respectively. The corrected positions as well as their associated errors can be found in Table 2 and are relative to the July 7th PPK base station position.

Table 2: PPK corrected positions. The associated errors are in addition to the June 7th PPP error. Aerial survey GCPs marked with * are the ones used for independent validation.

Group	Name	Latitude (deg)	Longitude (deg)	Elevation (m)	N/S Error (m)	E/W Error (m)	Elevation Error (m)	Group Error Summary (m)
SPi Cam GCPs	GCP01	67.18123018	-135.73016465	607.134	0.002	0.002	0.006	Average N/S: 0.005 E/W: 0.005 Elev: 0.017 Standard Deviation N/S: 0.003 E/W: 0.006 Elev: 0.014
	GCP02	67.18137077	-135.73063544	610.270	0.004	0.004	0.010	
	GCP03	67.18151274	-135.73088484	612.792	0.004	0.002	0.016	
	GCP04	67.18181319	-135.73121735	615.595	0.006	0.005	0.020	
	GCP05	67.18214991	-135.73169532	620.682	0.007	0.001	0.045	
	GCP06	67.18249687	-135.73096912	618.139	0.006	0.003	0.041	
	GCP07	67.18254529	-135.73034933	616.898	0.012	0.022	0.015	
	GCP08	67.18255336	-135.72985676	615.450	0.003	0.002	0.010	
	GCP09	67.18229618	-135.72918230	610.523	0.004	0.003	0.008	
	GCP10	67.18206796	-135.72914901	608.132	0.003	0.002	0.003	
SPi Cams	Scaramanga	67.18157836	-135.72727813	611.063	0.002	0.002	0.003	Average N/S: 0.004 E/W: 0.004 Elev: 0.005 Standard Deviation N/S: 0.003 E/W: 0.003 Elev: 0.001
	Drax	67.18163616	-135.72725675	612.815	0.007	0.009	0.004	
	Kananga	67.18168443	-135.72748512	609.141	0.002	0.002	0.004	
	Kristatos	67.18171770	-135.72724253	615.205	0.002	0.002	0.005	
	Zorin	67.18174396	-135.72743629	612.964	0.003	0.002	0.004	
	Orlov	67.18184323	-135.72726565	619.383	0.004	0.007	0.004	
	Blofeld	67.18193088	-135.72729165	621.923	0.002	0.004	0.006	
	Dr No	67.18202769	-135.72731210	623.405	0.003	0.002	0.004	
	Le Chiffre	67.18208708	-135.72745132	621.744	0.001	0.001	0.005	
	Goldfinger	67.18210142	-135.72764849	618.431	0.010	0.009	0.005	
	Klebb	67.18217930	-135.72749437	623.321	0.002	0.001	0.005	
	Largo	67.18221227	-135.72761654	621.220	0.006	0.003	0.006	
Jaws	67.18227348	-135.72753779	624.657	0.003	0.006	0.005		
Aerial Survey GCPs	DGCP01	67.17634541	-135.72116360	555.378	0.003	0.001	0.004	Average N/S: 0.012 E/W: 0.013 Elev: 0.008 Standard Deviation N/S: 0.012 E/W: 0.013 Elev: 0.006
	DGCP02	67.17656727	-135.72684857	570.265	0.037	0.039	0.020	
	DGCP03*	67.17998867	-135.73034138	600.014	0.002	0.003	0.005	
	DGCP04	67.18161403	-135.73280618	618.566	0.018	0.018	0.014	
	DGCP05	67.18338483	-135.73174814	630.223	0.008	0.005	0.005	
	DGCP06*	67.18239425	-135.72617954	633.980	0.004	0.007	0.004	
	DGCP07*	67.17912967	-135.72472793	584.083	0.013	0.016	0.005	

5.2 Aerial Surveys

The survey georeferencing errors relative to the local coordinate system of the GCPs were found to be 19 cm, 15 cm, 20 cm, 21 cm and 26 cm for the June 5th, June 20th, July 7th, August 7th, and September 20th aerial surveys respectively (Table 3). These values were heavily influenced by the elevations errors which in some cases were an order of magnitude larger than the errors in the x and y directions.

Table 3: Aerial survey georeferencing errors assuming the GCP positions are stable in both time and space.

Survey Date	N/S Error (m)	E/W Error (m)	Elevation Error (m)	Georeferencing Error (m)
June 5th, 2019	0.012	0.021	0.187	0.189
June 20th, 2019	0.006	0.036	0.145	0.149
July 7th, 2019	0.009	0.016	0.197	0.198
August 7th, 2019	0.066	0.070	0.189	0.212
September 20th 2019	0.015	0.015	0.259	0.260

The precision maps generated from the Monte Carlo analysis of each aerial survey are generally consistent between surveys with the exception of the August 7th survey (Figure 10 and Appendix A 5-7). The precision maps for the three surveys with local base stations show precision decreasing towards the edges of the survey area as well as in regions of dense vegetation such as the region on the south west edge of the debris tongue and the region on the south side of the highway. The survey precision also decreases in regions of steep topography such as the headwall of the slump and the river valley walls south of the highway. Interestingly the survey precision of the debris tongue also decreases slightly as slump activity increases between surveys.

The precision map generated from the Monte Carlo analysis of the August 7th survey showed noticeably lower precision across the entire survey area. There were two areas of moderately high precision, one around the upper headwall of the slump and the other in the

southeast corner of the survey area just south of the highway (Figure 11). Survey precision decreased with distance from either of the two higher precision areas.

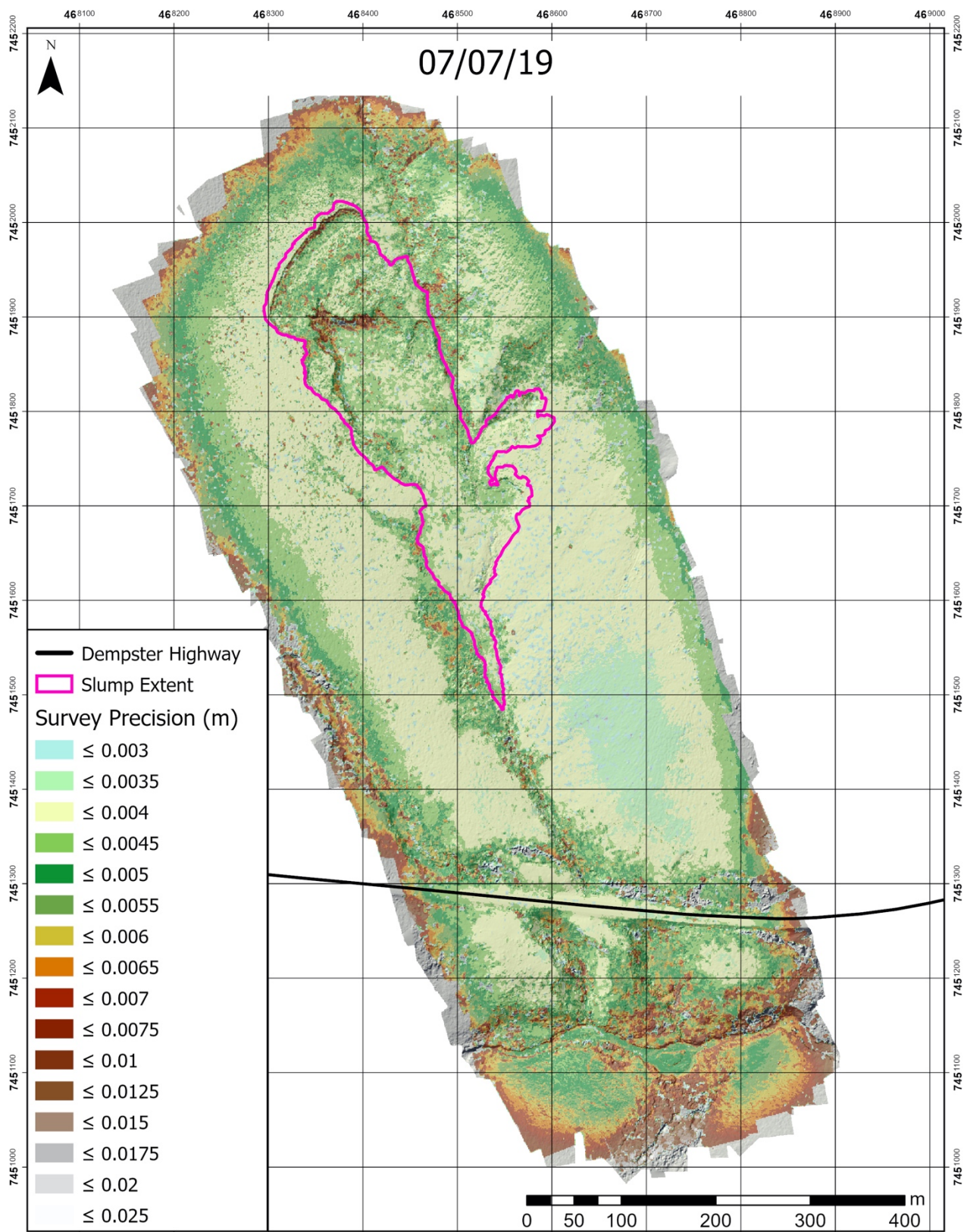


Figure 9: Precision map generated from the Monte Carlo analysis of the July 7th survey.

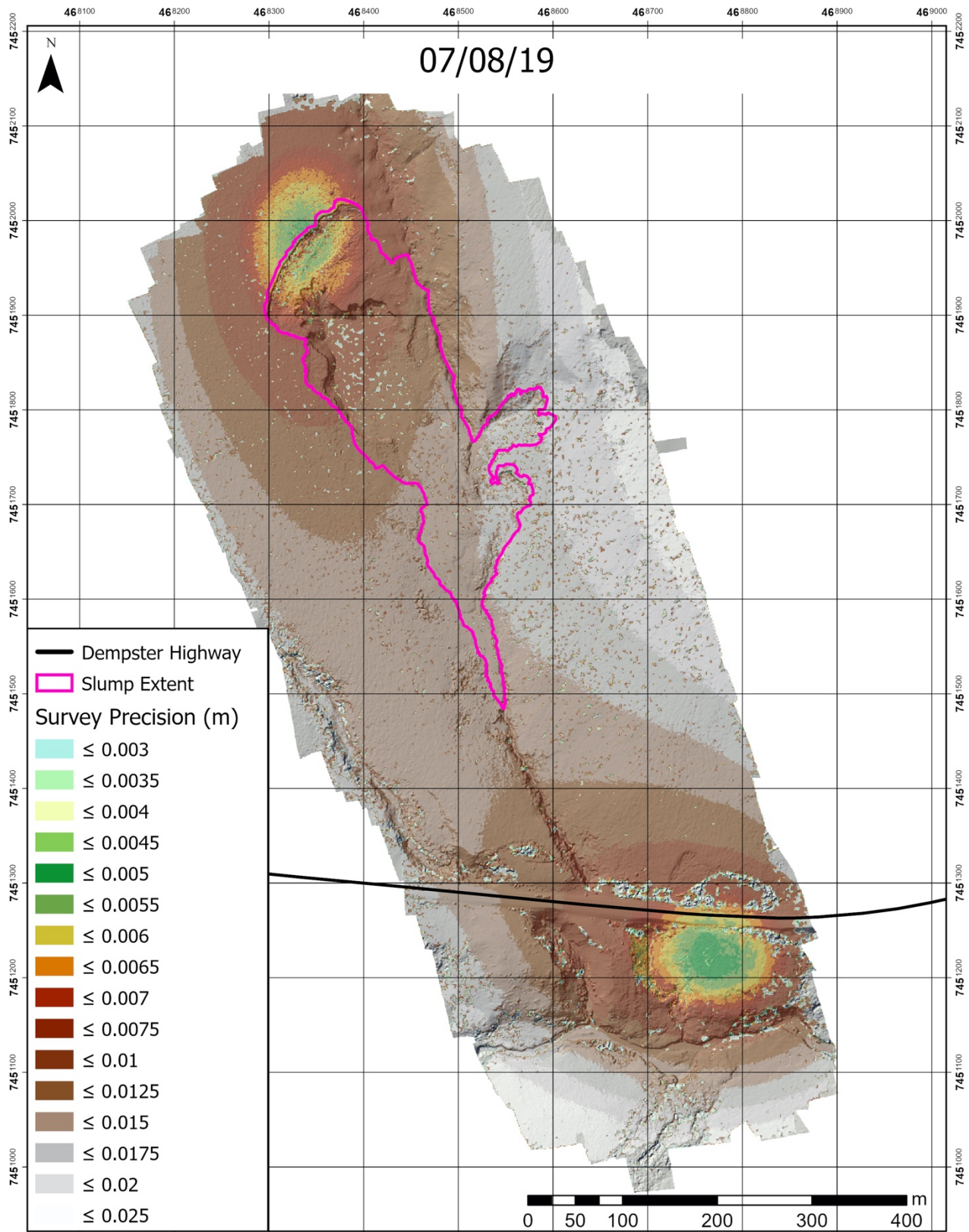


Figure 10: Precision map generated from the Monte Carlo analysis of the August 7th survey.

5.3 SPi Cameras

5.3.1 Preliminary Viewshed Analysis

Figure 12 shows the results of the viewshed analysis with the optimal camera locations and orientations as well as the locations of the GCPs used in the PyTrx analysis.

5.3.2 Field Complications

Technical issues were experienced during the operation of the SPi Cams which resulted in the SPi Cams turning off for their sleep cycles and not turning back on. As a result, the number of SPi Cams capturing information on the study area steadily decreased over the deployment period (Figure 13). This was an issue related to the code and an oversight in the equipment design. The first step when the SPi Cams powered on was to obtain a reliable GNSS signal and unfortunately the GNSS receivers of the SPi Cams were mounted upside down. Subsequently the SPi cams were not always able to obtain a reliable GNSS signal and as a result did not log that they had powered on.

Additionally, although the SPi Cams were built to withstand the elements, an additional oversight in deployment methods resulted in the cameras acting as sails in the high winds that are common during storms in the Peel Plateau. This resulted in the posts the SPi Cams were mounted to rotating within the ground and subsequently rotating the field of view of the SPi Cams. This shifted a few cameras to a point where they were no longer focused on the study area. The winds also caused a fair amount of shaking of the SPi Cams and although this did not result in image blur it did result in the failure of some of the adhesive holding the camera chip to the viewport of the enclosure.

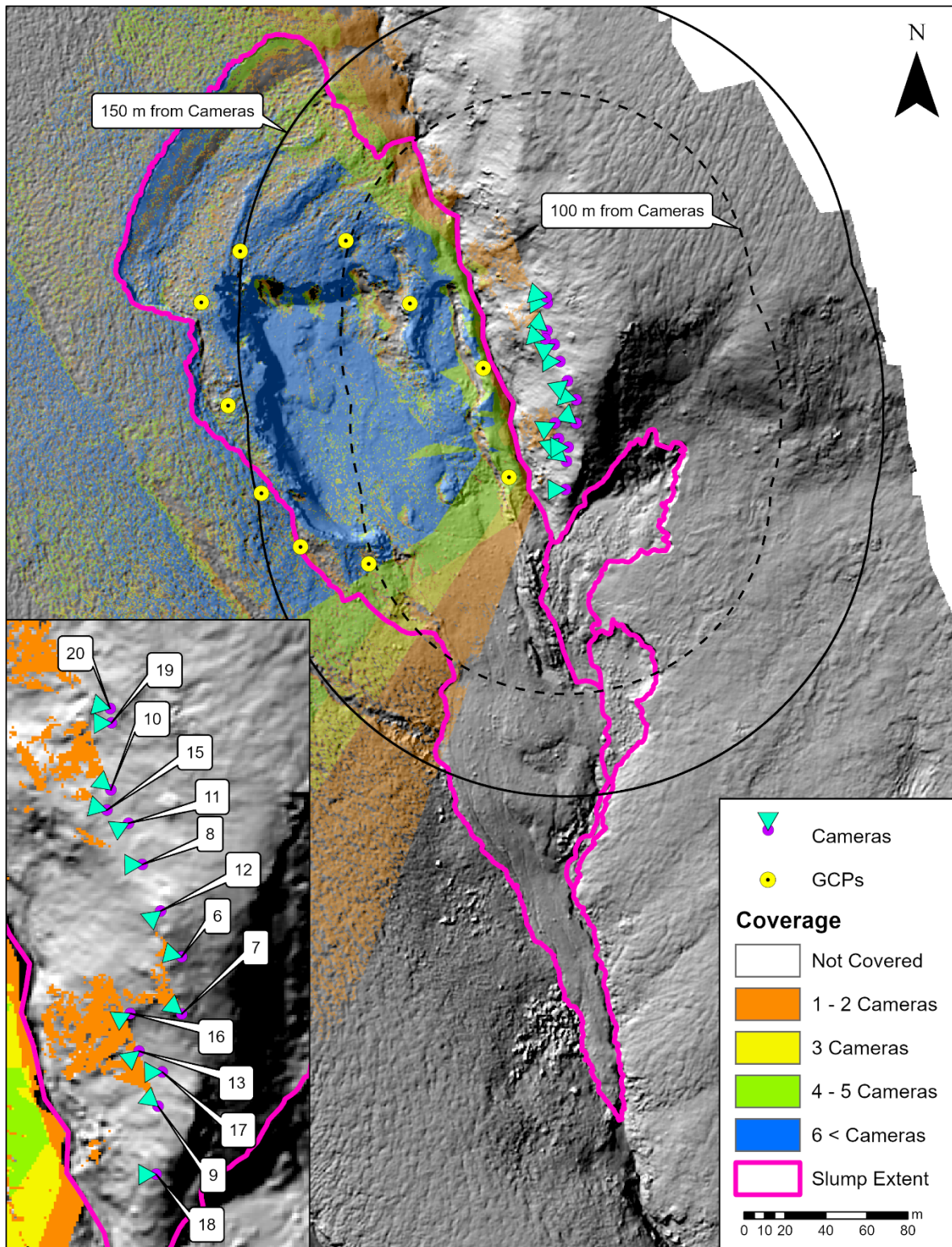


Figure 11: Viewshed analysis results showing optimal SPi Cam positions. The numbers correspond to the following cameras (ordered from N-S): 20-Jaws, 19-Largo, 10-Klebb, 15-Goldfinger, 11-Le Chiffre, 8-Dr No, 12-Blöfeld, 6-Orlov, 16-Zorin, 7-Kristatos, 13-Kananga, 17-Drax, 9-Scaramanga.

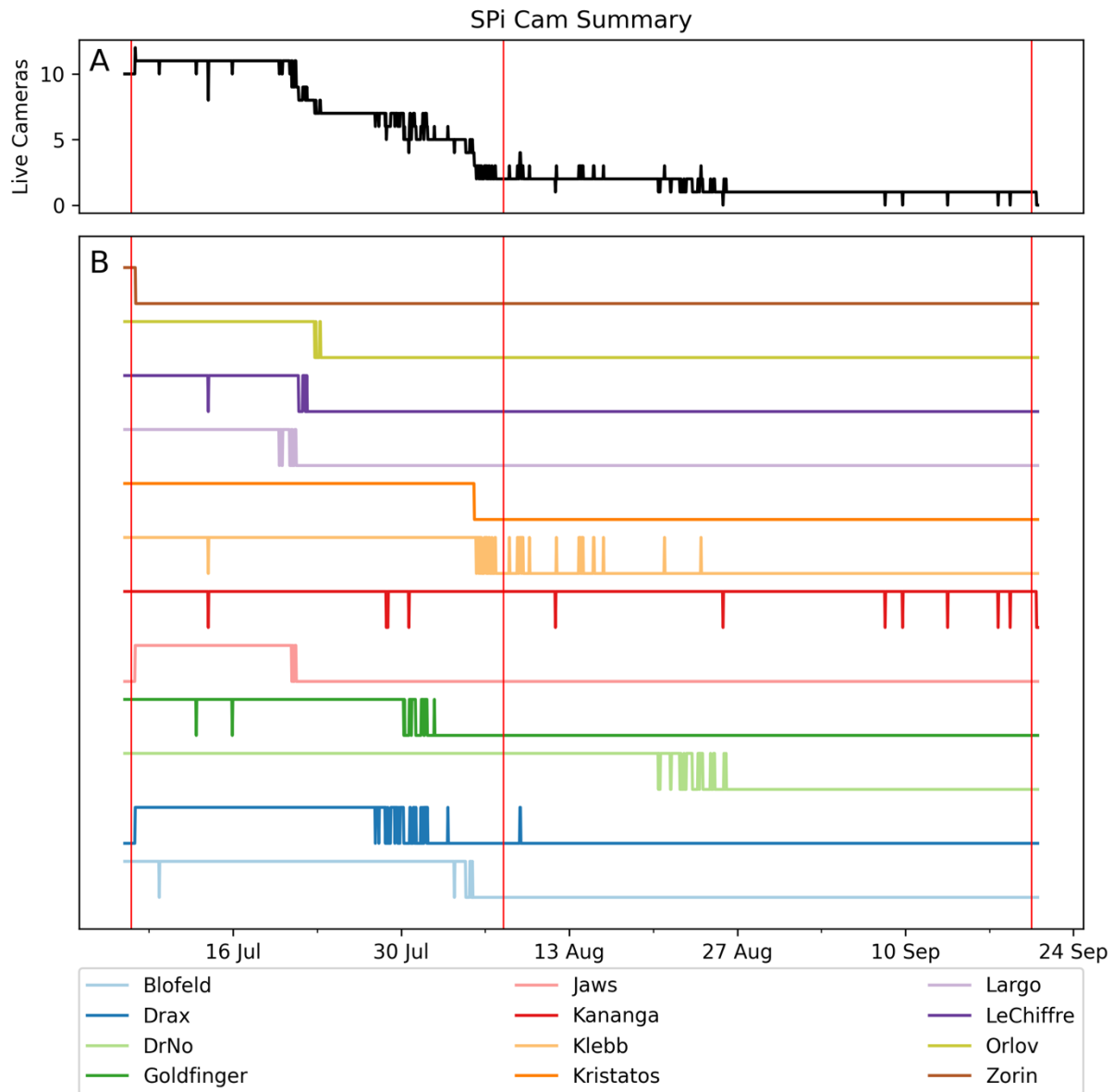


Figure 12: Timeline of live SPi Cams over the deployment period, this does not show if or when the cameras rotated. A shows the total number of live SPi Cams at a given time. B shows the timeline of each individual camera derived from the log files. Where the lines are in the upper position the camera was collecting data where they are in the lower position the camera was not collecting data. The vertical red lines indicate the dates the aerial surveys were conducted

5.3.3 Comparison to Commercial Trail Cameras

The data collected by the SPi cams was compared to the data collected by the Reconyx Ultrafire trail cameras. After comparing images taken by both camera systems at approximately the same time it was found that the SPi Cam image quality was better compared to the Reconyx image. The GCPs set out were not visible in the Reconyx image but clearly visible in the image captured by the SPi Cam (Figure 13). In contrast however the Reconyx cameras did not suffer the same field complications experienced by the SPi Cams and therefore captured data continuously for the entire deployment period.

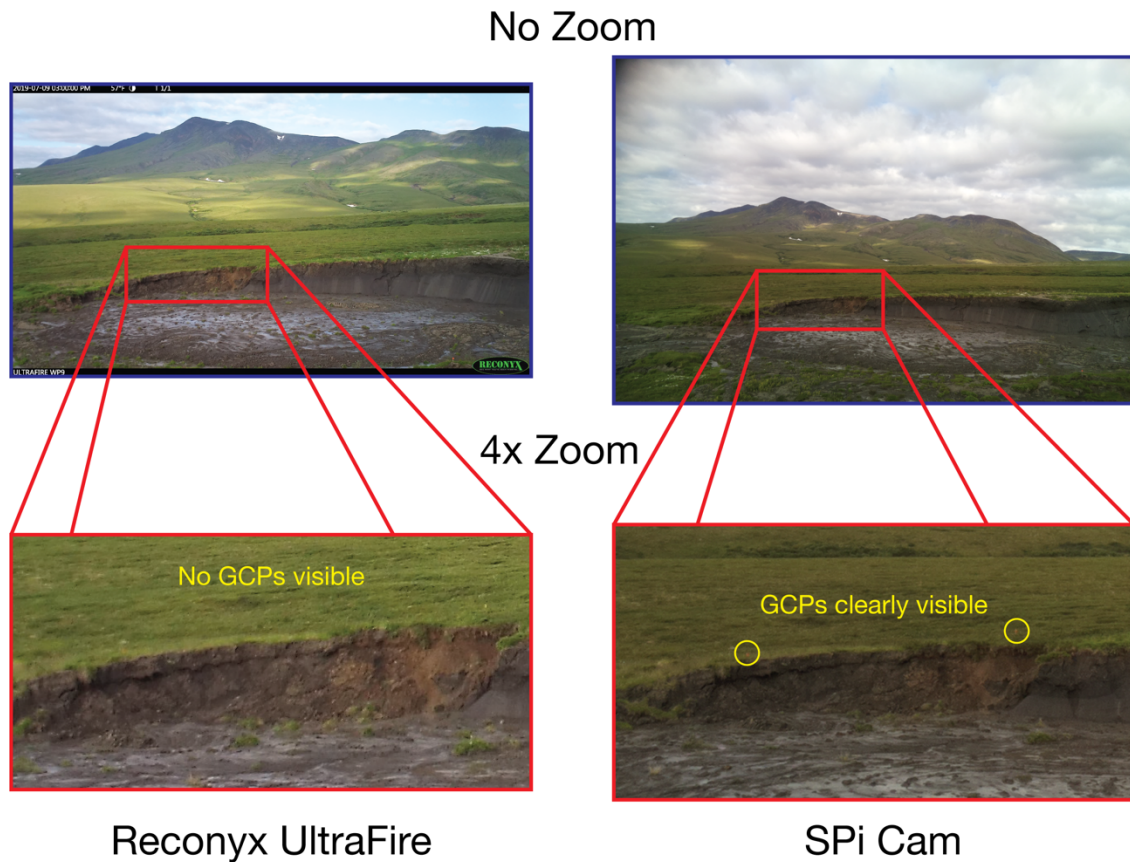


Figure 13: A comparison of image quality between the SPi Cams and the Reconyx Ultrafire.

5.4 M3C2-PM Analysis

For the topographic change detection analysis on the aerial photo survey data the registration errors were found to be between 4.6 cm and 10.3 cm. Full details of the registration errors can be found in Table 4.

Table 4: Relative registration errors of the aerial survey change detection pairs.

Survey 1 Date	Survey 2 Date	N/S Error (m)	E/W Error (m)	Elevation Error (m)	Registration Error (m)
June 5 th	June 20 th	-0.016	0.006	0.042	0.046
June 20 th	July 7 th	-0.023	0.003	0.052	0.056
July 7 th	August 7 th	-0.054	-0.058	0.008	0.079
August 7 th	September 20 th	-0.055	-0.051	0.070	0.103

Because the August 7th aerial survey had a noticeably lower precision than the other surveys, the level of detection maps for the two change detection pairs that included the August 7th survey are significantly different compared to the others. For the pairs that did not include the August 7th aerial survey, the level of detection maps appear relatively uniform with the LoD values increasing at the fringes of the survey area (Figure 15 and Appendix A 8). The LoD also increased in regions of steep topography and dense vegetation the same as in the precision maps. For the pairs that did include the August 7th survey, the level of detection maps were heavily influenced by the August 7th survey precision and therefore followed a similar pattern (Figure 16 and Appendix A 9). The LoD was lowest in the two regions where the August 7th survey had the highest precision and increased with distance from either point. Overall, the LoD for the change detection pairs that included the August 7th survey was far higher than those that did not include that survey.

Due to the fact that the August 7th survey exhibits indications of unquantifiable doming that can be seen in Figure 21 and Figure 24 the volume estimates obtained from the change detection analysis using that survey are assumed to be less accurate compared to the other

change detection pairs. However, these results were still presented because despite the inaccuracies because they provide a key piece of information on how the slump behaves late in the thaw season. The cause of the unquantifiable doming along with the other survey imprecisions will be discussed in Section 6.2.3.

Table 5: Change metrics calculated from the M3C2-PM significant change results within the extent of the slump. Values in brackets are the 95% confidence intervals.

Change Metrics	19/06/05 to 19/06/20	19/06/20 to 19/07/07	19/07/07 to 19/08/07	19/08/07 to 19/09/20
Total Volume Gained (m ³)	2673.73 (42.73)	5033.03 (63.99)	15391.83 (120.58)	8115.86 (100.48)
Total Volume Lost (m ³)	5740.85 (95.65)	8656.09 (148.84)	23048.73 (318.00)	24402.79 (254.17)
Total Volume Change (m ³)	-3067.11 (104.76)	-3623.06 (162.01)	-7656.90 (340.09)	-16286.93 (273.31)
Area with Elevation Increase (m ²)	6923.00	9444.00	22346.00	10175.00
Area with Elevation Decrease (m ²)	5565.00	6587.00	8444.00	16907.00
Total Area Experiencing Change (m ²)	12488.00	16031.00	30790.00	27082.00
Average Elevation Increase (m)	0.39 (0.01)	0.53 (0.01)	0.69 (0.01)	0.80 (0.01)
Average Elevation Decrease (m)	-1.03 (-0.02)	-1.31 (-0.02)	-2.73 (-0.04)	-1.44 (-0.02)

Table 6: Change metrics for each summary zone M3C2-PM significant change results. Values in brackets are the 95% confidence intervals.

Change Detection Pair	Zone	Total Volume Change (m³)	Area Experiencing Change (m²)	Average Elevation Change (m)
19/06/05 to 19/06/20	1	0.44 (0.22)	4	0.11 (0.06)
19/06/20 to 19/07/07	1	335.98 (19.41)	304	1.11 (0.06)
19/07/07 to 19/08/07	1	139.63 (8.6)	301	0.46 (0.03)
19/08/07 to 19/09/20	1	-0.7 (0.4)	3	-0.23 (-0.13)
19/06/05 to 19/06/20	2	209.77 (13.1)	302	0.69 (0.04)
19/06/20 to 19/07/07	2	129.5 (7.73)	306	0.42 (0.03)
19/07/07 to 19/08/07	2	42.93 (3.15)	191	0.22 (0.02)
19/08/07 to 19/09/20	2	37.76 (3.36)	132	0.29 (0.03)
19/06/05 to 19/06/20	3	11.77 (1.9)	49	0.24 (0.04)
19/06/20 to 19/07/07	3	4.77 (1)	25	0.19 (0.04)
19/07/07 to 19/08/07	3	276.53 (18.07)	256	1.08 (0.07)
19/08/07 to 19/09/20	3	-7.77 (1.64)	24	-0.32 (-0.07)
19/06/05 to 19/06/20	4	0 (0)	0	0 (0)
19/06/20 to 19/07/07	4	0 (0)	0	0 (0)
19/07/07 to 19/08/07	4	334.01 (19.6)	305	1.1 (0.06)
19/08/07 to 19/09/20	4	75.42 (8)	158	0.28 (0.09)

Based on the M3C2-PM analysis, significant topographic change was identified both within the slump as well as the surrounding area between the June 5th and 20th aerial surveys (Figure 17). The upper section of the debris tongue, below the headwall, gained up to 2 m per m² of material at the highest point with most of the area gaining at least 0.5 m (Figure 18). Overall, 12488 m² within the extent of the slump experienced significant change with a total volume change of $-3067 \pm 105 \text{ m}^3$ (Table 5). Outside of the slump extent there were noticeable apparent elevation gains up to 2.5 m per m in regions of dense vegetation and smaller gains in other vegetated areas. Additionally, there were noticeable areas of material loss in the drainage channel on the west edge of the survey area as well as the river valley south of the highway.

Between the June 20th and July 7th aerial surveys the significant topographic change was more limited to within the extent of the slump (Figure 20). The upper debris tongue again experienced a gain in material up to 2 m per m² but the area experiencing the gain was much larger and further from the headwall compared to the change that occurred between the previous two aerial surveys (Figure 19). Overall, within the slump, a total of 16031 m² experienced significant topographic change with a total volume change of $-3623 \pm 162 \text{ m}^3$ (Table 5). Outside of the significant gains were limited to regions of dense vegetation and regions of significant loss were limited to the west drainage valley and the south river channel.

Between the July 7th and August 7th aerial surveys the M3C2-PM analysis identified significant changes both within and outside of the slump extent (Figure 21). The upper portion of the debris tongue experienced smaller gains of up to 1 m per m² with most of that gain occurring further from the headwall. The mid to lower portion of the debris tongue experienced a mostly uniform gain of up to 2 m per m² gain tapering off towards the edges (Figure 22). Of all four change detection analyses performed this showed the largest changes with a total material gain of $15392 \pm 121 \text{ m}^3$, a total material loss of $23049 \pm 318 \text{ m}^3$, and a total of 30790 m² experienced significant change (Table 5). In addition, summary zones 3 and 4

experienced total volume changes of $276.53 \pm 18.07 \text{ m}^3$ and $334.01 \pm 19.6 \text{ m}^3$ respectively during this period (Table 6). Outside of the slump there were three large regions of significant change. The northern region of the survey area as well as the southeast corner experienced a uniform gain of up to 0.5 m and the southwest corner experienced a uniform loss of up to 0.5 m.

Between the August 7th and September 20th aerial surveys the M3C2-PM analysis again identified significant changes both within and outside of the slump extent (Figure 24). The upper debris tongue experienced little significant changes with some regions experiencing gains of up to 1 m per m^2 which were isolated to the fringes of where significant changes occurred between the previous aerial surveys. The mid portion of the debris tongue experienced gains of up to 3 m per m^2 mostly on the east side of the debris tongue (Figure 23). The slump experienced a total change in volume of $-16287 \pm 273 \text{ m}^3$ and 27082 m^2 within the slump experienced significant change (Table 5). Outside the extent of the slump losses of up to 1 m were experienced in areas of dense vegetation. The inverse of the changes observed in the northern region, southwest and southeast corners the previous TCD analysis were also observed.

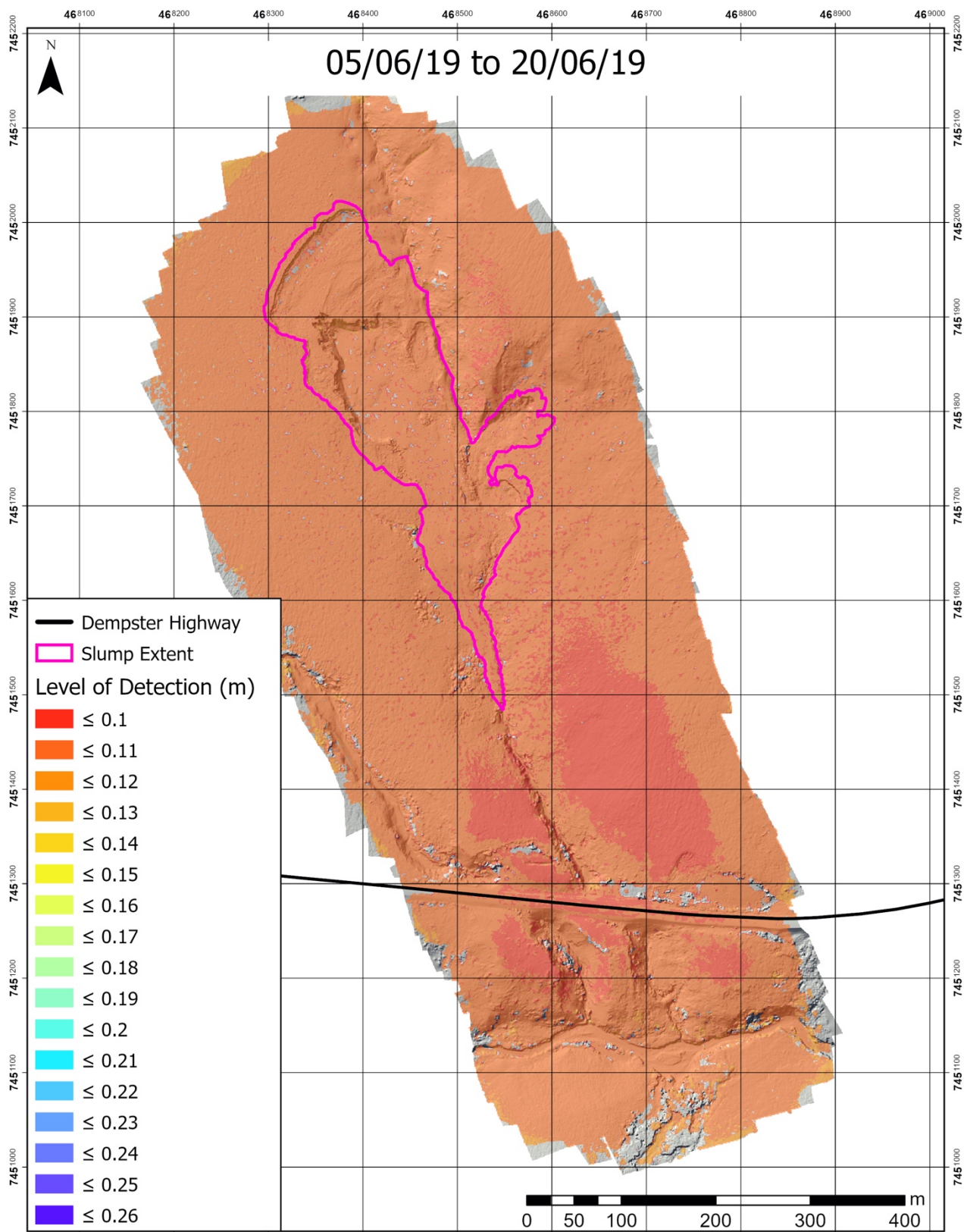


Figure 14: Level of detection map for the June 5th and June 20th aerial survey change detection pair.

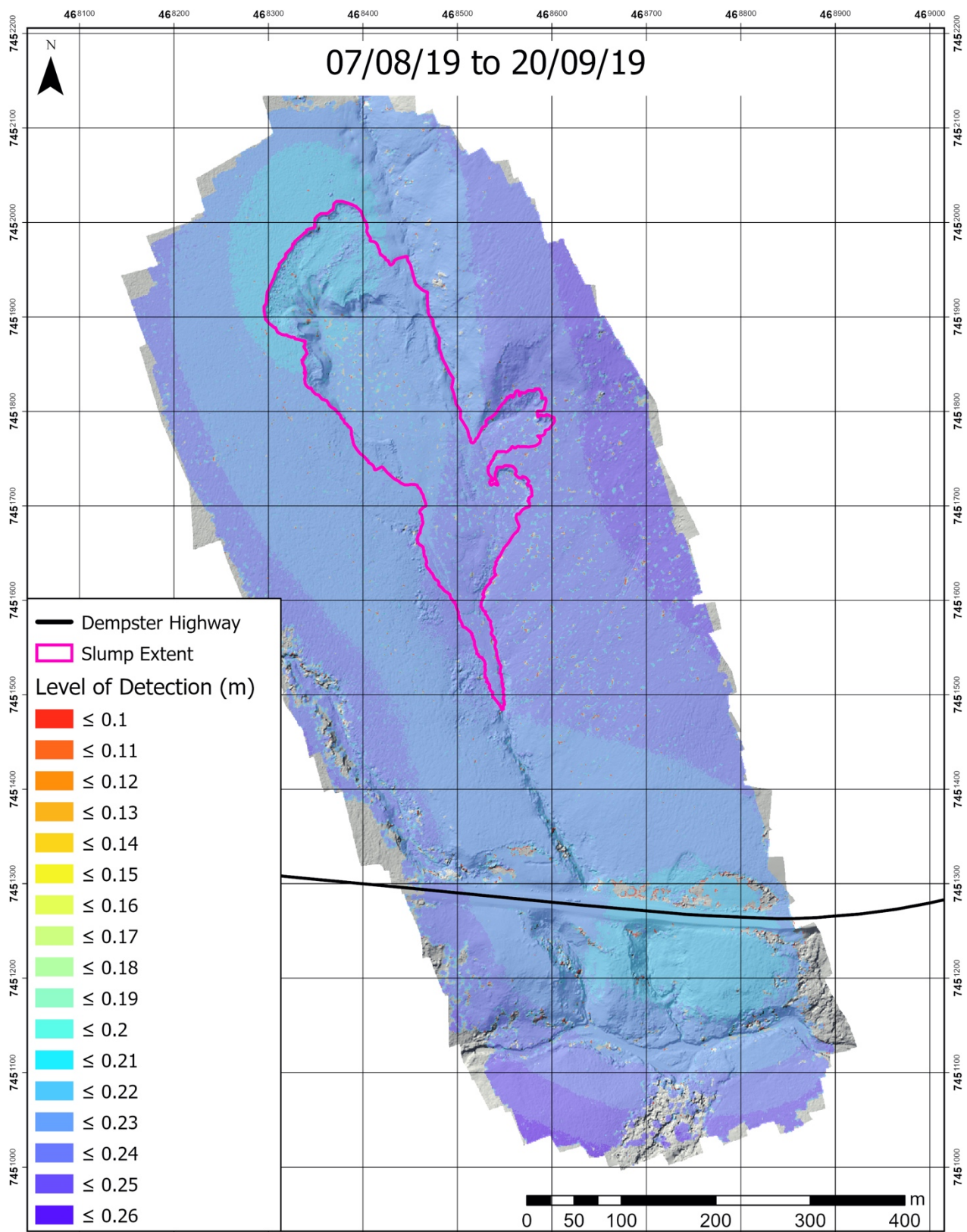


Figure 15: Level of detection map for the August 7th and September 20th aerial survey change detection pair.

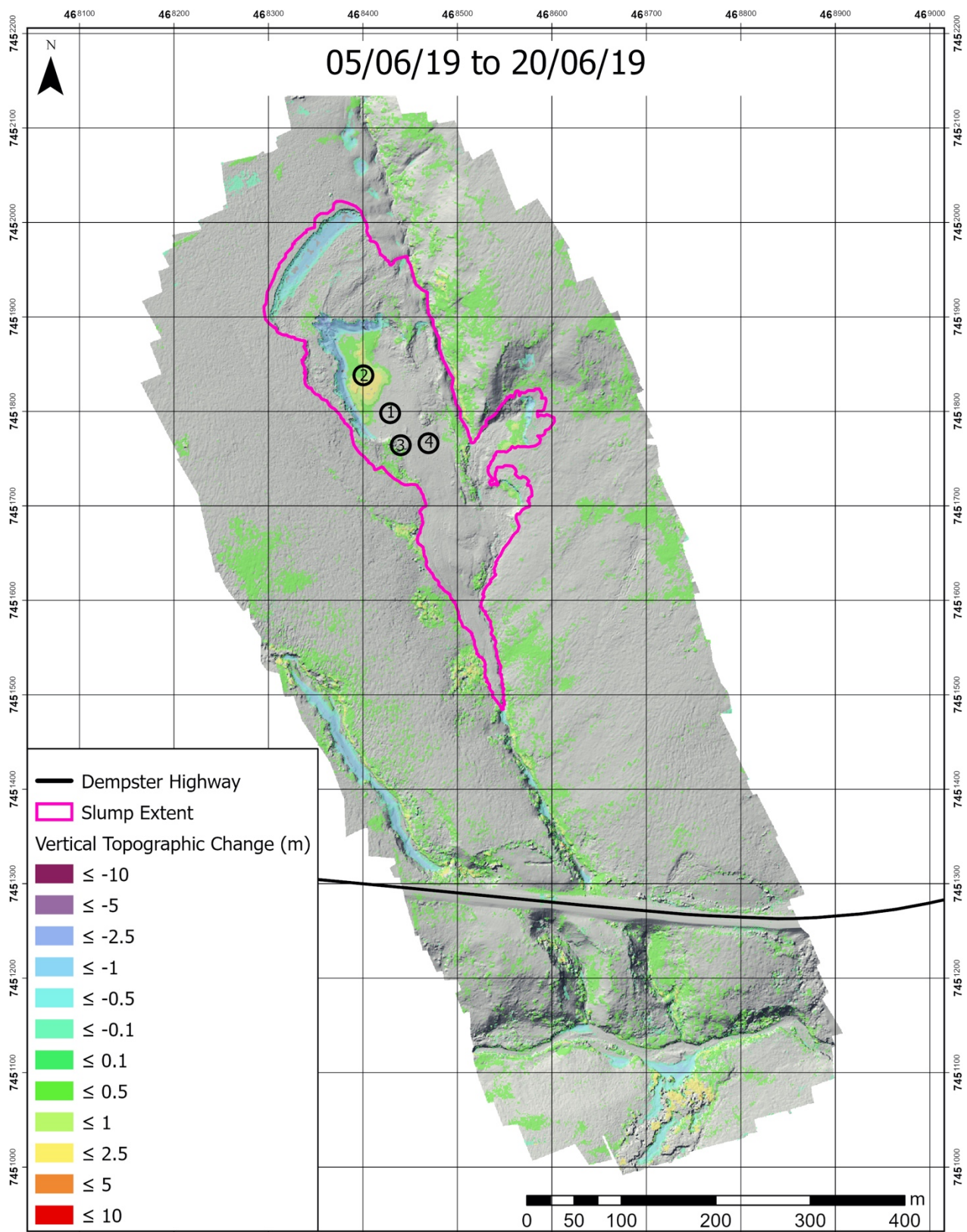


Figure 16: Significant topographic change that occurred between the June 5th survey and the June 20th survey. The numbered circles are the four summary zones.

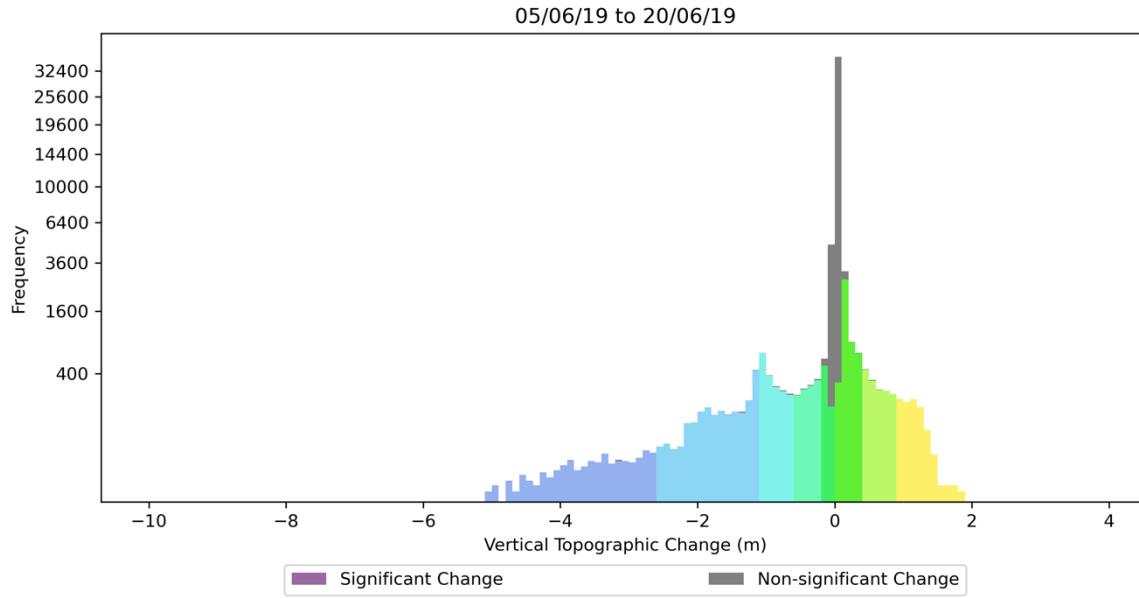


Figure 17: Distribution of vertical topographic change pixel values within the slump extent for the change that occurred between the June 5th survey and the June 20th survey. Note that an exponential y-axis used.

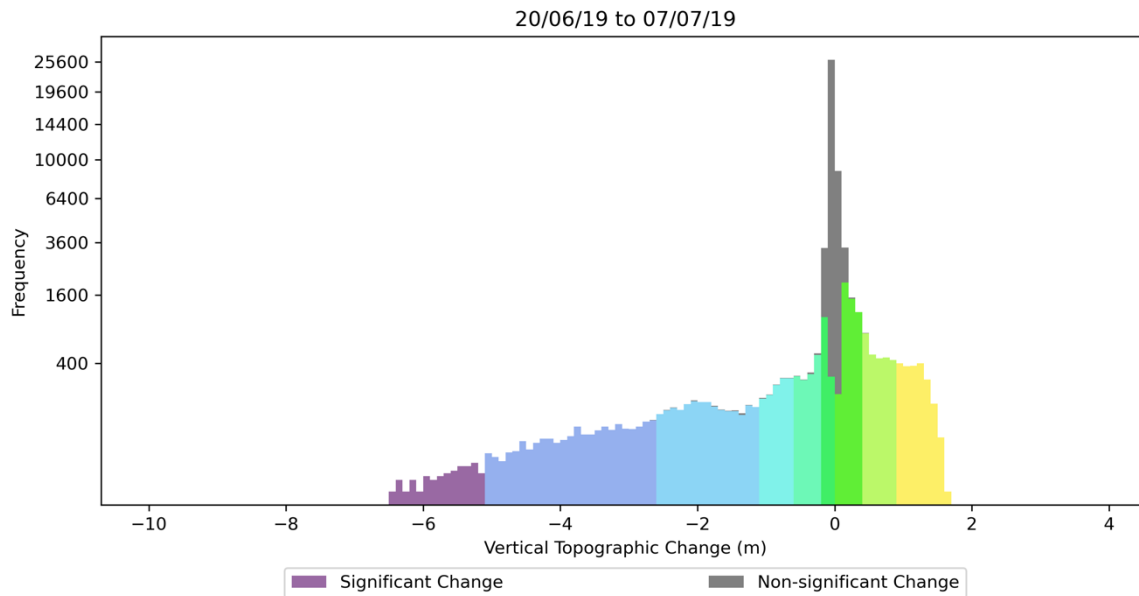


Figure 18: Distribution of vertical topographic change pixel values within the slump extent for the change that occurred between the June 20th survey and the July 7th survey. Note that an exponential y-axis used.

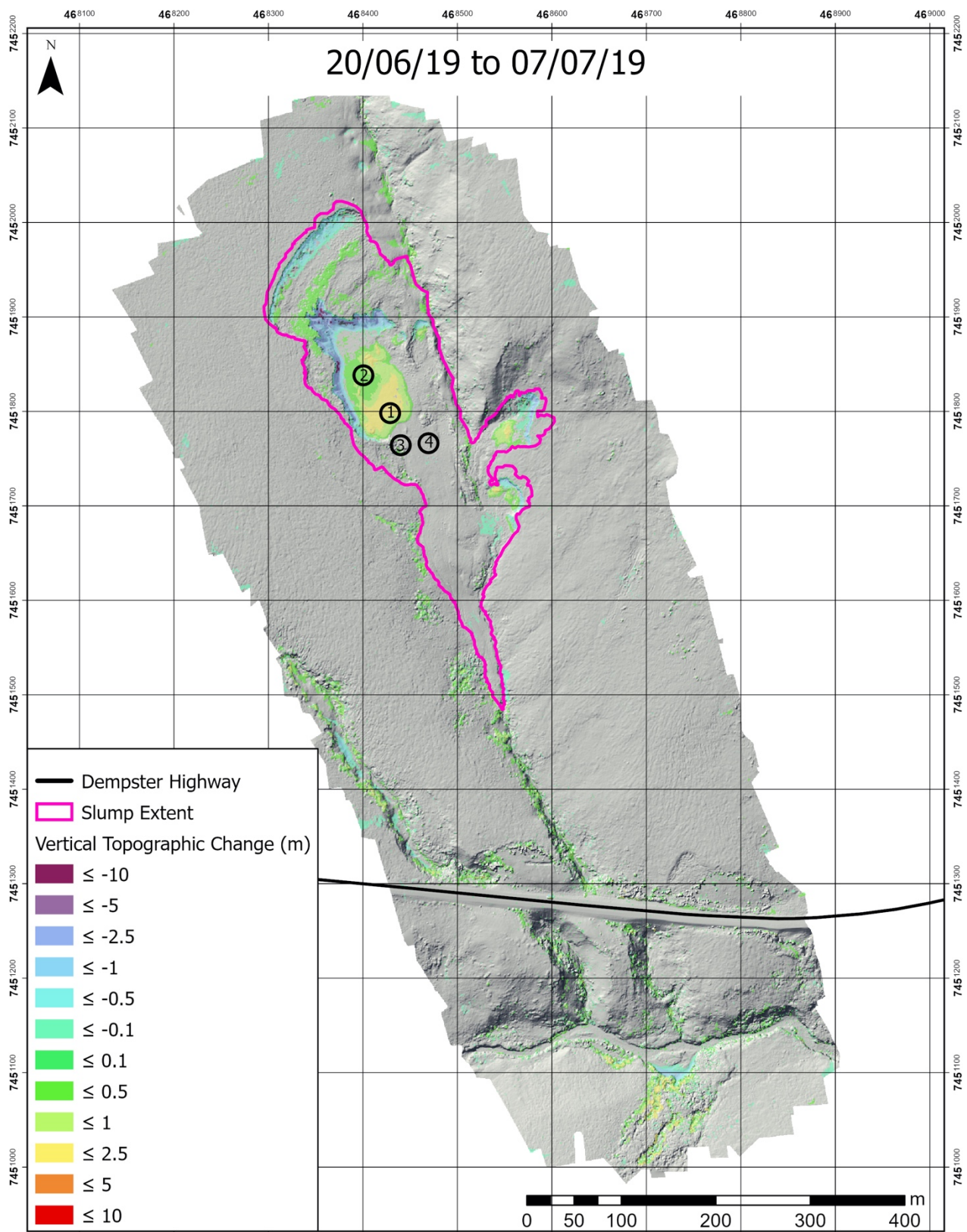


Figure 19: Significant topographic change that occurred between the June 20th survey and the July 7th survey. The numbered circles are the four summary zones.

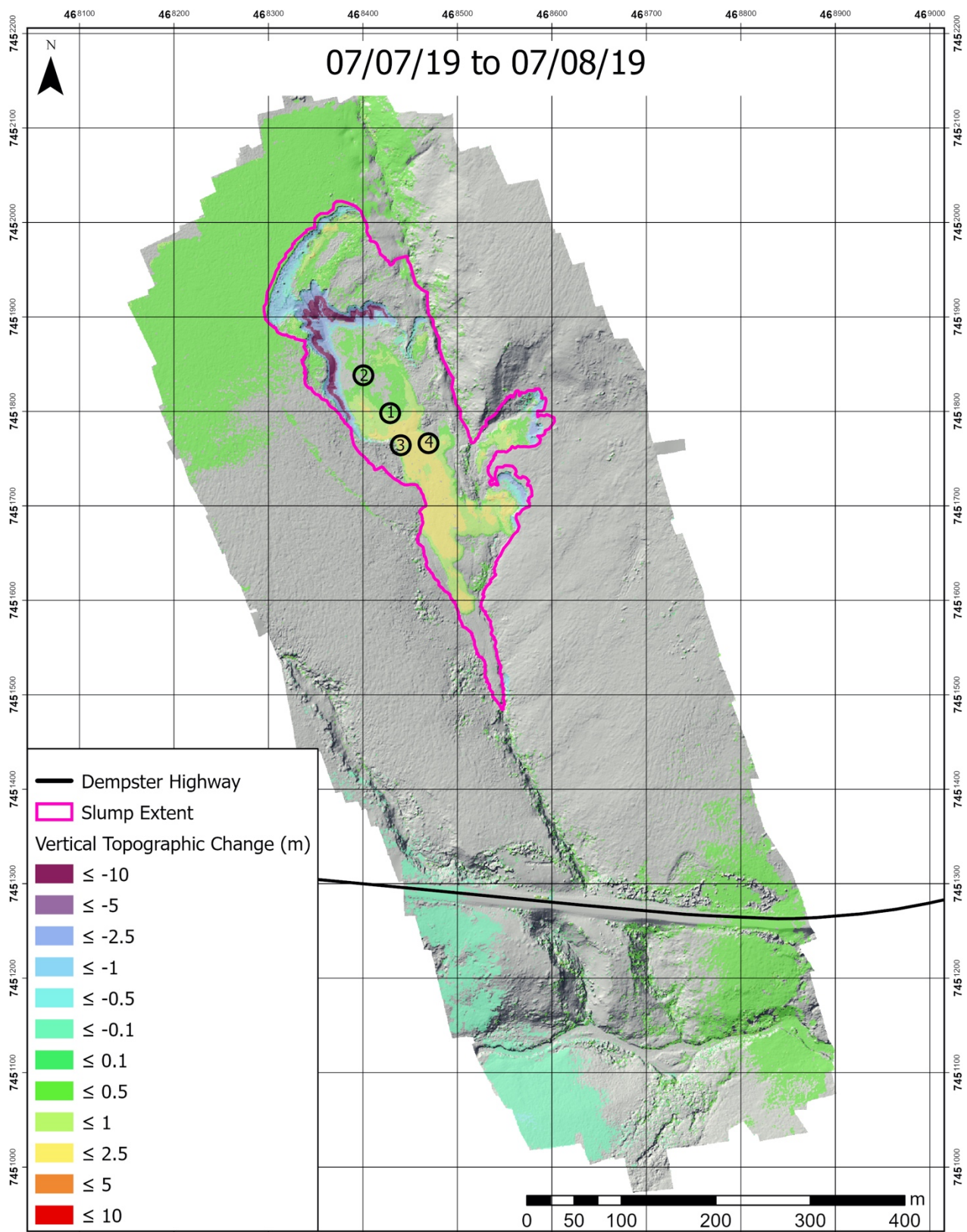


Figure 20: Significant topographic change that occurred between the July 7th survey and the August 7th survey. The numbered circles are the four summary zones.

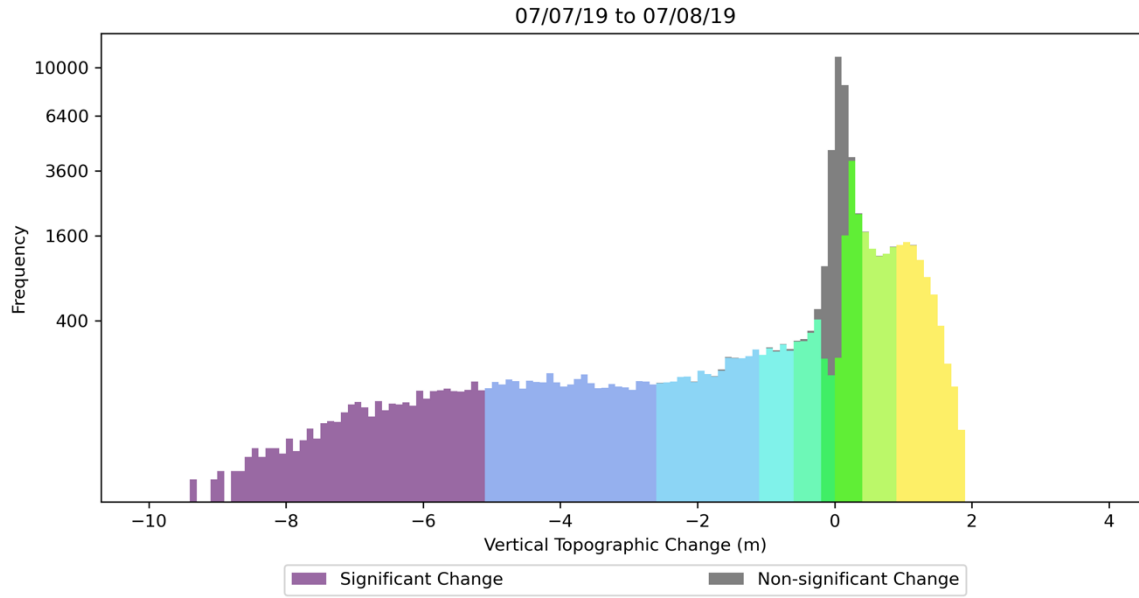


Figure 21: Distribution of vertical topographic change pixel values within the slump extent for the change that occurred between the July 7th survey and the August 7th survey. Note that an exponential y-axis used.

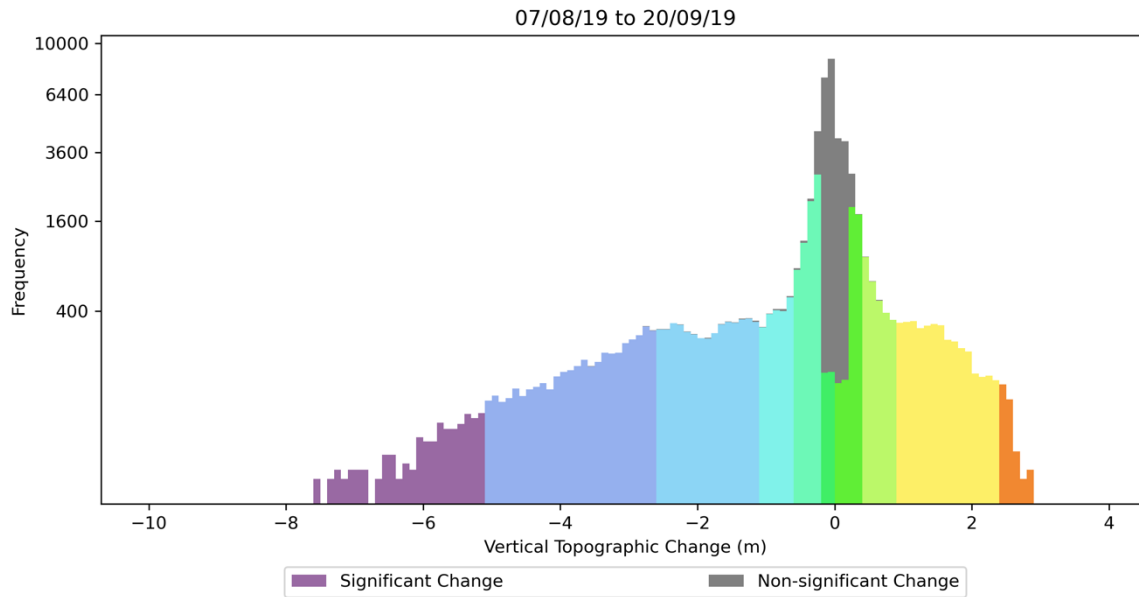


Figure 22: Distribution of vertical topographic change pixel values within the slump extent for the change that occurred between the August 7th survey and the September 20th survey. Note that an exponential y-axis used.

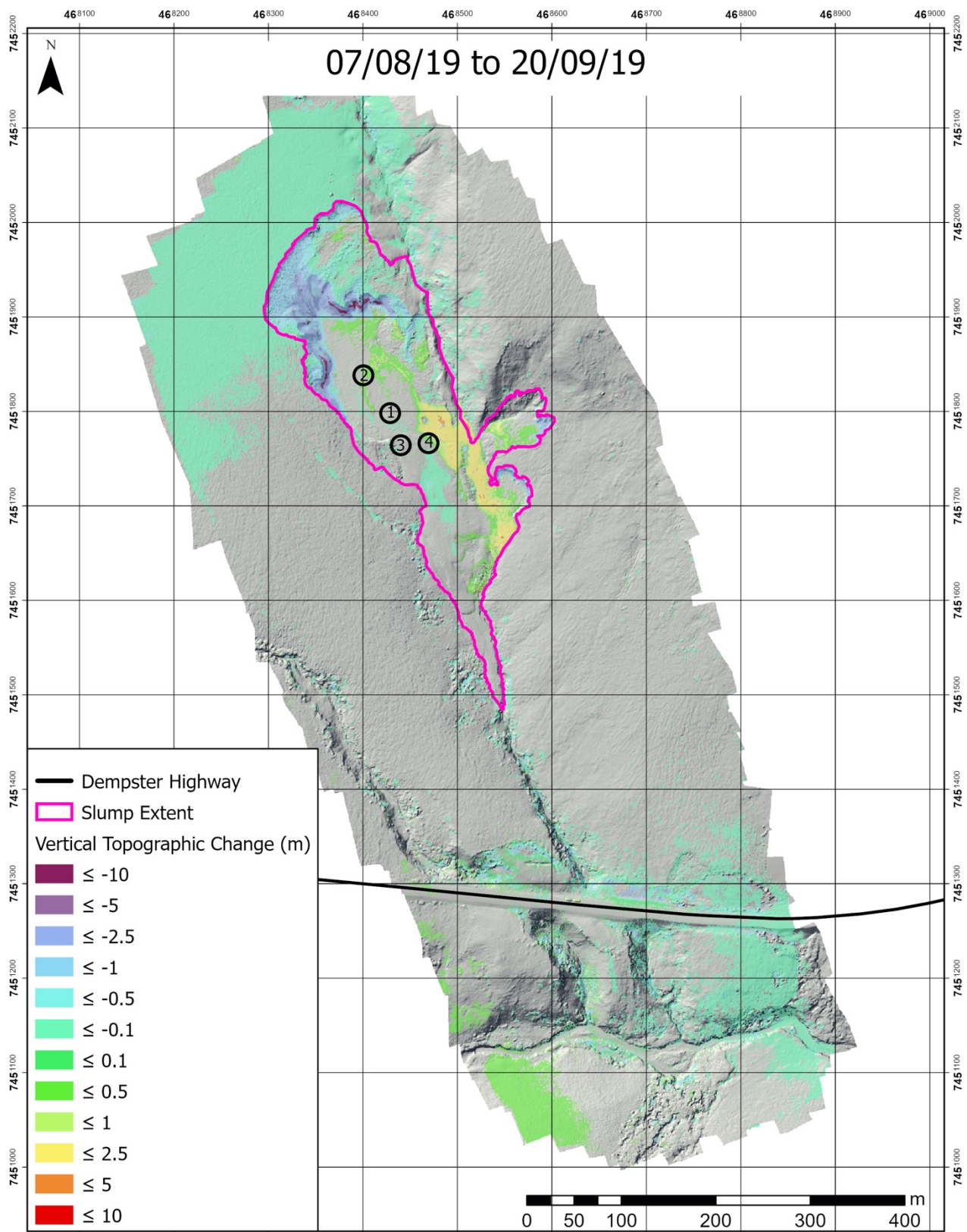


Figure 23: Significant topographic change that occurred between the August 7th survey and the September 20th survey. The numbered circles are the four summary zones.

5.5 PyTrx Analysis and Imagery Observations

Three photo series were collected by the Dr No and Kristatos SPi Cams which covered the majority of the period between the July 7th and August 7th. Kristatos did not experience any movement throughout the period of interest and therefore collected a relatively uninterrupted photo series from July 7th to August 3rd when it stopped collecting data (Figure 13). Dr No experienced multiple movement events which resulted in the photo series be split into three sections. The first two photo series which spanned July 7th to July 13th and July 14th to July 20th still captured the GCPs and were therefore able to be georeferenced and produce usable data. Unfortunately, between July 20th and 22nd Dr No rotated so drastically that only 2 GCPs were in view and therefore the data captured after this event could not be reliably georeferenced. However, these images remained useful for qualitative validation of theories on how the debris tongue developed after August 7th when there was no quantitative information on development at the daily time scale.

For the Dr No photo series between July 7th and 13th, the average georeferencing error which describes the positional precision of the velocity vectors was found to be 8.43 m. The average homography error of the photo series, which describes how well the images were aligned to each other was found to be 0.071 pixels. The average error of all of the displacements which is the difference between the forward and backtracked displacements was found to be 2.1 cm (Table 7). The Dr No photo series that spanned July 14th to 20th had the highest average errors associated with it however this was a result of a few large outlier photos skewing the results. The average georeferencing error was found to be 10.29 m. The average homography error of the photo series was found to be 1.038 pixels. The average error of all of the displacements calculated was found to be 1.9 cm (Table 7). The photo series that spanned July 7th to August 3rd captured by Kristatos had some of the lowest average errors associated with it. The average georeferencing error was found to be 9.51 m. The average homography

error of the photo series was found to be 0.020 pixels. The average error of all of the displacements calculated was found to be 2.4 cm (Table 7).

Table 7: A summary of the errors associated with the PyTrx analysis

Camera	Image Series	Georeferencing Error (m)		Homography Error (px)		Displacement Error (m)	
		Average	Standard Deviation	Average	Standard Deviation	Average	Standard Deviation
Kristatos	July 7 th , 20:30 to August 3 rd , 6:30	9.51	4.56	0.020	0.105	0.024	0.016
Dr No	July 7 th , 20:30 to July 13 th , 19:30	8.43	7.36	0.071	1.552	0.021	0.016
Dr No	July 14 th , 22:30 to July 20 th , 20:30	10.29	7.13	1.038	4.606	0.019	0.013

The results produced by the LOWESS filtering method produced smoothed results that were in agreement with the results from the manual filtering method for the data from Kristatos. However, for the datasets from Dr No the LOWESS filtering method produced results that were less in agreement with the other data, likely due to the shorter span of those datasets. The manual filtering method on both the Kristatos and Dr No data produced results that were in agreement with each other and the LOWESS filtered Kristatos data. Because of this, the manual filtering method was chosen, and the results presented have been filtered using this method. With that said, the LOWESS results from the Kristatos dataset are an easily understandable representation of how the velocity changes over time so it has been included to show the general trend in the data.

The results from summary zones three and four are the most interesting and will be discussed here. The remaining results can be found in Appendix A 10 and A 11. The results of summary zone three show two short periods when the velocity increased. The first occurred in the period approximately between July 13th and 16th and the second occurs approximately between July 25th and 28th (Figure 25). The first movement event seen in summary zone three had the highest velocity reaching (approximately 1 m/hour). The increase in velocity was

relatively linear until the maximum velocity was reached. The second movement event is seen in both summary zones three and four (Figure 25 and Figure 26). It shows a maximum velocity of approximately 0.5 m/hour in both zones. In this case, the displacement rate increases and decreases more gradually compared to the first movement event. The displacement rate increases first in summary zone three, then in summary zone four, but the decrease in displacement rates is not similarly staggered. Inspection of the imagery for both of these periods confirms that there was a noticeable increase in slump movement and acts as a qualitative validation to these results (Appendix B 4, B 5, B 7, and B 8). Additionally, rainfall events were observed in the images leading up to these movement events (Appendix B 3, B 6).

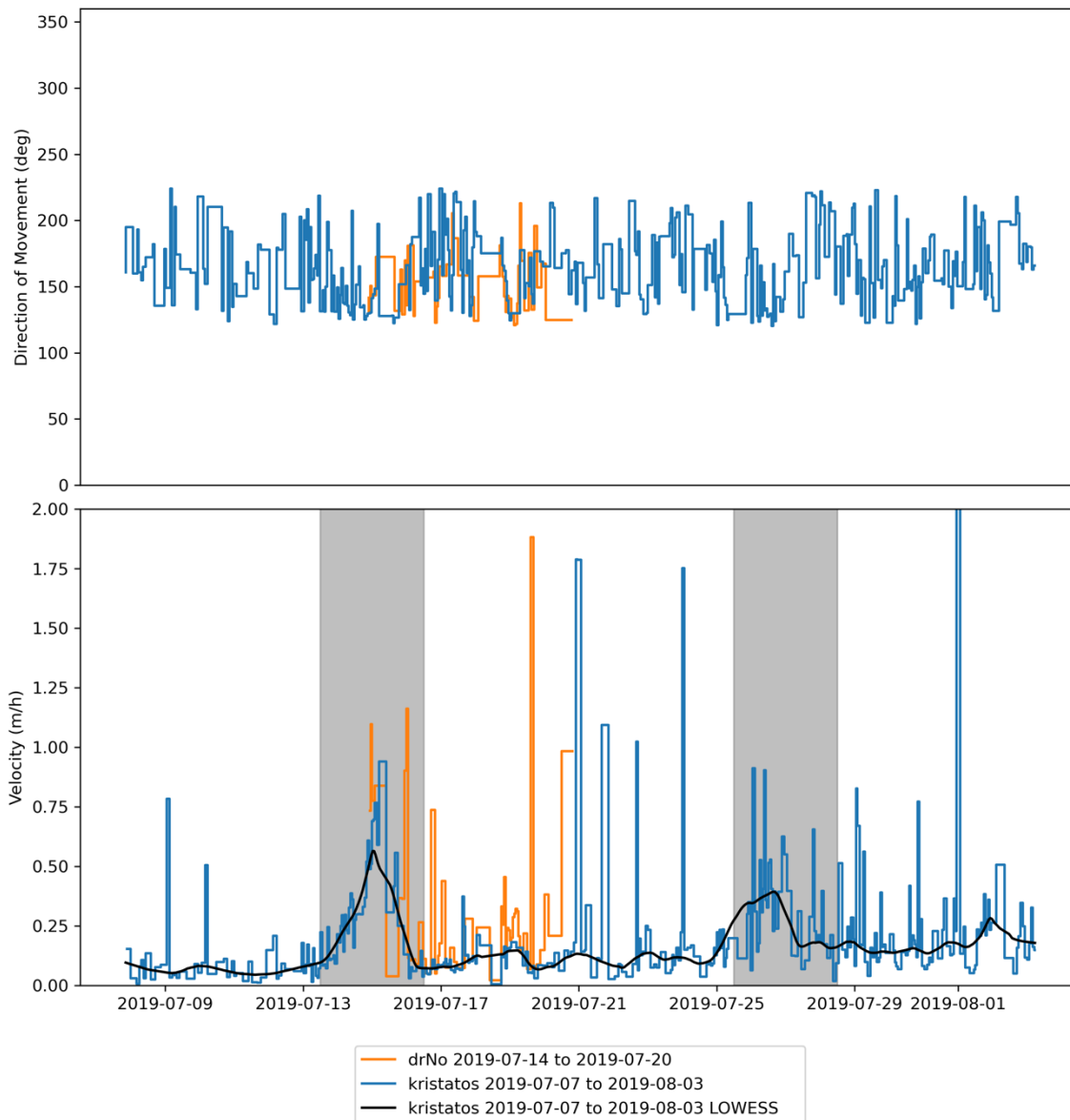


Figure 24: The filtered velocity (bottom) and direction (top) of the displacement measured by PyTrx that occurred in summary zone three. The grey regions highlight the two movement events

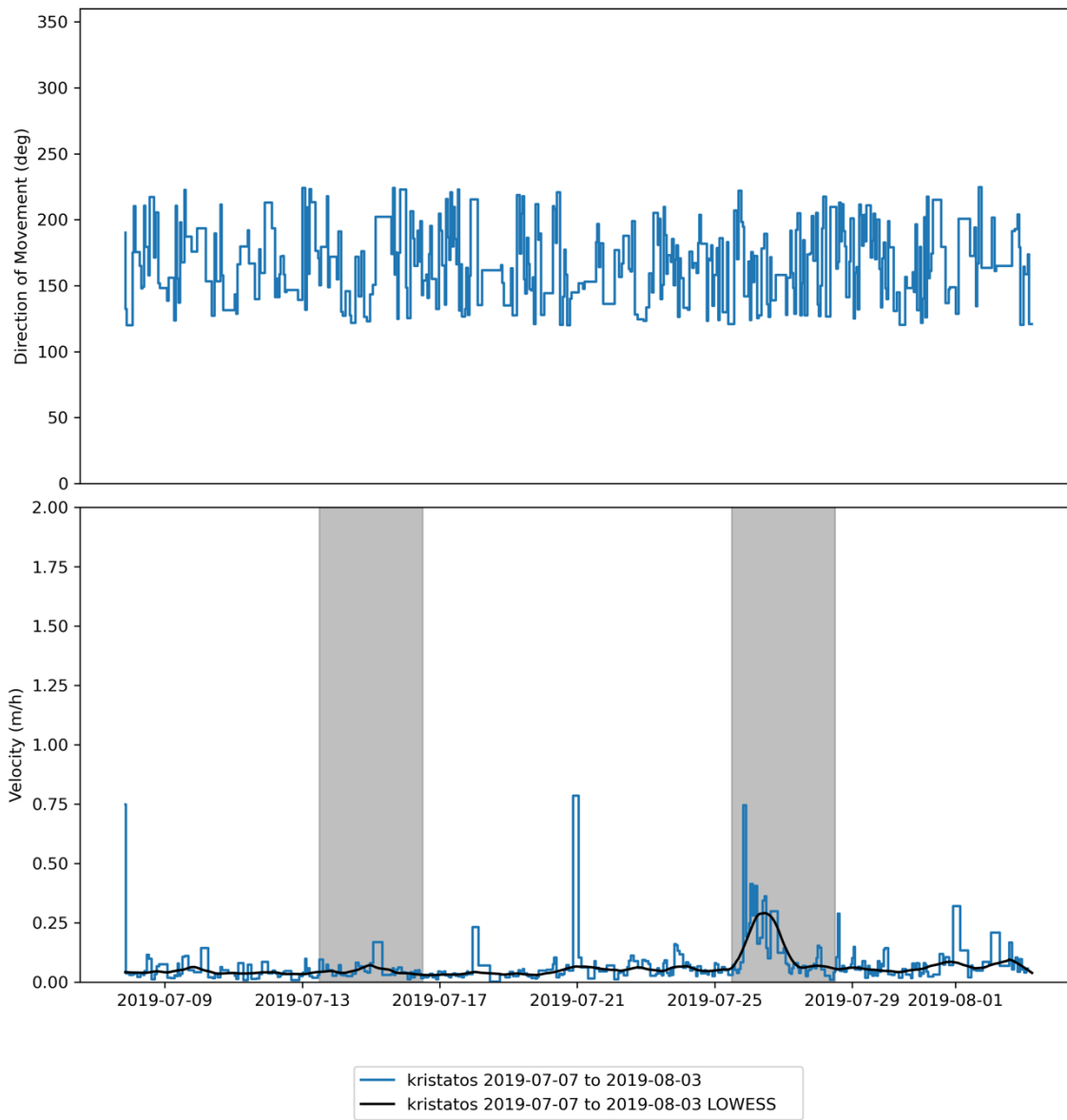


Figure 25: The filtered velocity (bottom) and direction (top) of the displacement measured by PyTrx that occurred in summary zone four. The grey regions highlight the two movement events

6 Interpretation

6.1 Debris Tongue Development

Figure 17, Figure 20, Figure 21, and Figure 24 do not show any evidence of the non-active portions debris tongue material deposited in previous years reactivating. This is first evident by the fact that there are no significant changes within the slump that are not a part of the active flow that can be seen developing through the figures. This can be interpreted as the 2019 debris tongue developing over the course of the thaw season and flowing over top of the material deposited in previous years with no reactivation of the existing material occurring. In addition to this, once a portion of the current year's debris tongue stabilized it did not reactivate. This is evident in Figure 21 and Figure 24, where Figure 21 shows a large amount of material deposited in the centre of the debris tongue. Then in Figure 24 the location of the subsequently deposited material is along the east side of the previous deposit with very little deposition occurring where the change occurred in Figure 21. This can be interpreted as the new material seen in Figure 21 stabilizing relatively quickly after its deposition. As a result, the new material identified in Figure 24, which flowed out from the headwall, was forced east and then south along a new path of least resistance. This is also supported by what is seen in the images captured by the SPi Cams. This is interesting because it shows that particular portions of the debris tongue do not remain active for very long and once stabilized, they did not reactivate in this case.

The results also show that the development of the debris tongue exhibits different behaviours at different times during the thaw season. These time periods can be divided into early and late season development stages and are discussed in the following subsections.

6.1.1 Early Season Development

The early season development stage occurred from May, when air temperatures rose to be consistently above 0°C, to mid-July, when air temperatures and precipitation typically reach their maxima. Figure 17 and Figure 20 show the change experienced during the later portion of this period, and based on these results, a reasonable prediction can be made about what occurred prior. Figure 17 shows that a small low-angle debris tongue developed at the base of the headwall. Figure 20 shows the debris tongue doubled in size and advanced significantly down slope but has maintained a similar elevation relative to the stable debris tongue. Based on these two observations it can be assumed that during this time the debris tongue developed continuously as an unconstrained feature which grew downslope in every direction it was not constrained while maintaining an elevation approximately 2 m above the material it was flowing over. This is supported by what was observed in the images captured by the SPi cams between July 7th and July 11th (Appendix B 1 and B 2).

Based on this, and the existing knowledge of how climatic variables influence retrogressive thaw slump activity, this can be extrapolated to describe the development near the beginning of the early season period (Kokelj et al., 2015; Lacelle et al., 2010). It is likely that the volume and extent of the debris tongue, during the early season period, follows something similar to an exponential curve with respect to time. Due to the cooler air and relatively low precipitation the debris tongue likely developed very slowly in May as a small pancake-like feature at the base of the headwall. Then as air temperature and precipitation increase in June, the debris tongue began to develop more rapidly, forming the feature seen in Figure 17. Finally, near the end of the early season period as air temperatures and precipitation are both reaching their maximum, the debris tongue developed rapidly. This is exemplified in Figure 20 which shows large changes in the size of the debris tongue that occurred over a 17 day period.

6.1.2 Late Season Development

The late season development stage then occurred from mid-July to late September, when air temperatures dropped consistently below 0°C. Figure 21 and Figure 24 capture the change that occurred during the entirety of this period. In addition to this, Figure 25 and Figure 26 provide insight into how the changes seen in Figure 21 occurred. These figures show that during the late season period the debris tongue development transitions from a continuously developing pancake to more pulse-like events where the debris tongue rapidly advances in a single direction over a short period of time. Figure 21 clearly shows the singular direction advance of the debris tongue and Figure 25 and Figure 26 provide context into how that development occurred. Prior to the first large movement event between July 13th and 16th movement seen in Figure 25 the displacement rate is relatively slow and consistent. This is in agreement with what is discussed as early season development above. The movement event between July 13th and 16th is then indicative of a spill-out event where the extent of the pancake-like feature is breached, and material rapidly flowed down slope along the west side of the existing debris tongue after which the movement returns to a slower rate. Then later, between July 25th and 28th, a second increase in movement is observed in both Figure 25 and Figure 26 leading to the conclusion that a second spill-out event occurred. This second spill-out event followed the path of the initial spill-out, potentially remobilizing some of the still active debris tongue material from the initial spill-out but also transported material through the central portion of the existing debris tongue. These two events likely transported the majority of the newly deposited material seen in Figure 21. The data in Table 6 supports this and shows that between July 7th and August 7th summary zones 3 and 4 experienced changes in volume that are significantly larger than the changes experienced during the time between the other surveys. This is also supported by the images captured by the SPi Cams.

Based on these observations it is reasonable to assume that the debris tongue development seen in Figure 24 was formed by a similar pulse-like movement event or a series of pulse-like movements. This is based on the fact that the new material seen in Figure 24 is deposited linearly, similar to the material deposited in Figure 21. This is also supported by the images captured by Dr No after July 20th when the camera's field of view rotated past what could be used in the PyTrx analysis. The photo series shows what appears to be a two-tiered pulse which flows around the already stabilized material (Appendix B 9, B 10, and B 11).

6.2 Other Observations

6.2.1 Surface Property Changes

In addition to the changes discussed within the extent of the slump, Figure 17-18 also show changes occurring in the surrounding stable ground. Many of these changes can be explained by various natural processes occurring in the landscape. Figure 17 and Figure 20 both show the surrounding drainage valleys experiencing significant change. When investigated further this was in fact a result of snow that was deposited in the valleys slowly melting over the course of the first three surveys. The orthophotos from the July 5th, July 20th, and June 7th aerial surveys show the snow progressively disappearing during this time period (Appendix A 1-3). The orthophotos also show snow progressively disappearing from the upper headwall of the slump. This impacts the results of the volumetric changes presented in Table 5 and inflates the volumetric loss values obtained for the first two change detection pairs. Due to the fact that the main focus of this work was on the debris tongue and not the volumetric mass balance of the slump these values were not corrected for snow melt, however it is unlikely that the corrected results would be drastically different.

Figure 17, 16 and 18 also show significant changes occurring in areas of dense vegetation. This is due to the fact that June and September are the periods of green-up and leaf loss respectively. Because SfM-based survey techniques rely on photos to generate a

model of the topography as the leaves on dense vegetation develop the view of the ground surface is obstructed and the top of the canopy is captured. This results in the top of the canopy becoming the elevation for that region and false changes being identified. This can be accounted for to some extent by using algorithms to filter out the influence of vegetation however because this thesis focuses on the debris tongue which was predominately vegetation free this step was not deemed necessary.

6.2.2 Volumetric Changes

Although it was not an objective of this thesis to investigate drivers of the volumetric changes that occurred between the aerial photo surveys this topic should be elaborated. The results of the M3C2-PM volume analyses (Table 5 and Table 6) provided confidence bounded estimates of the volumetric changes that occurred within the slump over the 2019 thaw season. The consistent negative change in total volume between all of the change detection pairs can be explained by the thawing of the ice-rich headwall. The water generated by the melting of this massive ice saturates the debris tongue material allowing it to flow down slope. As the debris tongue stabilizes the water within the material is removed from the slump through drainage or evaporation. As a result, only the soil material remains resulting in a net volumetric loss. This means that these estimates of the total change in volume are a first-order estimate of massive ice loss from the headwall, a point that has also been presented by van der Sluijs et al. (2018).

However, the estimates presented here are not as accurate as they could be. As mentioned previously there is snow that is progressively melting in the headwall regions of the first three aerial photo surveys. If an accurate estimate of massive ice loss was to be obtained the volumetric change of the melting snow would need to be removed from the total volume change. In addition, the imprecisions related to the August 7th survey propagate through the analysis in such a way that any volumetric estimate obtained using the data from that survey

are known to be inaccurate. As a result, this survey would need to be excluded from any analysis focused on estimating volumetric changes and massive ice loss.

6.2.3 Observations Related to the August 7th Imprecisions

Because of the technical issues experienced by the August 7th aerial survey, the precision of that survey compared to the others was significantly reduced. However, it also provided the opportunity to investigate how survey precision is affected when the image locations are not known precisely as well as how this lack of precision propagates through a change detection workflow. Together Figure 8 and 10 show how survey precision is heavily influenced by the number of overlapping images when the precise location of the camera is not known. Both regions of high precision in Figure 11 coincide with areas in Figure 8 where image density was slightly higher to capture the furthest extent of the survey area. These findings coincide with those presented by James et al. (2017) and demonstrate the importance of precise direct georeferencing in aerial SfM surveys with weaker network geometries.

Figure 16 and Appendix A 9 highlight how the imprecision of the August 7th survey influenced the level of detection calculations and therefore the change detection analysis. However, Figure 21 and 18 also show signs of unrepresented errors propagating through the change detection analysis. The changes shown in the northern region, southwest corner and south east corner of Figure 21 and then the reversal of that change in Figure 24 are indicative of doming in the August 7th survey. This doming is difficult to quantify as it is the result of systemic errors inherent to the SfM workflow (James et al., 2017). But the properties of the August 7th survey do coincide with the findings of James et al. (2017) for surveys with parallel flight lines (weak network geometries) and a strong network of ground control points. The James et al. (2017) findings show that doming is present in simulated surveys with two sets of parallel flight lines that do not have photo position information and a strong network of GCPs. The August 7th survey, like all other surveys in this work consists of one set of parallel flight

lines. But unlike the other surveys the lack of a nearby base station caused more imprecision in the photo locations of the August 7th survey. This resulted in the SfM workflow being less constrained and as a result the systemic errors a point cloud with some amount of doming.

These findings also make the case for M3C2-PM to become the new standard in topographic change detection because errors like these can be identified and tracked. In a DoD workflow the only evaluation of error are the georeferencing and registration errors (Table 3 and 4) and these are taken as uniform across the entire survey area. If that was done in this case the results obtained by processing the August 7th survey would contain large amounts of unquantified errors and could result in misinterpretation of the processes occurring in the slump. Additionally, a user would have little knowledge of the errors present in the August 7th data as the error metrics presented in Table 3 and 4 for that date appear quite similar compared to the other surveys.

7 Discussion

7.1 Material Deposited in Previous Years

To my knowledge, this is the first study where the M3C2-PM algorithm has been used to perform a change detection analysis on a retrogressive thaw slump. This method provides insight on how errors propagate within and between the surveys and results in the ability to determine the statistical significance of the topographic change. In this case the LoD values for all change detection pairs within the extent of the slump were less than or equal to 0.24 m (Figure 16). Therefore, it is not very likely that the relation between monitoring period and data quality limits the ability to detect change in this study. In the case of the M3C2-PM results, the rate of topographic change that would have eluded detection was less than approximately 25 cm/month. Given the majority of the changes observed were much larger it is likely that little to no change went undetected. This supports and validates the interpretation that there was little to no reactivation of the material deposited by the debris tongue in previous years. This study provides the first quantitative evidence to show that stabilized debris tongue material does not reactivate and as such provides a new understanding of how the debris tongue develops overtime.

7.2 Debris Tongue Development

This thesis presents the first breakdown of debris tongue development stages which describe how rate and timing of debris tongue movement as well as material deposition vary spatially and temporally during the thaw season. In the early season development stage, a pancake-like debris tongue begins to consistently develop and grow, flowing away from the headwall in every direction it is not constrained. This development begins slow, but near the end of the early season development stage, the volume change of the pancake over a 17 day period is approximately 1.9 times larger than that of the previous 15 day period (Table 5). The

debris tongue then transitions into the late season development stage when the debris tongue movement was pulse-like. The debris tongue material then rapidly advanced in a single direction over a short period of time followed by a period of relatively little movement. The velocities of these rapid movement events ranged from approximately 0.25 to 1 m/hour and occurred over approximately a 3 day period. These pulse-like movement events contributed to the majority of debris tongue deposition material with the double pulse events observed in Figure 25 depositing up to 15392 m³ of material (Table 5).

This is not the first time changes in the style of debris tongue movement have been presented. The results presented by Kokelj et al. (2015) show slow consistent movement in June transitioning to periods of rapid movement interspersed by lower rates of movement in July and August. These results mirror those described in this thesis. However, they only span the summer months of the thaw season and are qualitative observations based on data from time-lapse cameras focused on a portion of the debris tongue and therefore can only provide limited insight into the change experienced. With the addition of the aerial photo surveys, improvement of the data processing methods to produce quantitative results, and the expansion of the monitoring period, these development stages can be described quantitatively and in more detail. This provides a new understanding of how retrogressive thaw slump debris tongues develop over the course of a thaw season which can inform new research as well as the development of numerical models.

In addition, this thesis builds off the methods of Kokelj et al. (2015) by improving the methods to extract qualitative data from a similar field set up. This represents a novel advance in retrogressive thaw slump monitoring by demonstrating a semi-automated method of collecting quantitative debris tongue velocity metrics without the need for frequent site visits or placing monitoring devices on the active debris tongue.

7.3 Limitations

Although this work presents some novel findings there are some limitations to the interpretation of the results. Most notably, the change detection results which were produced using the August 7th survey are known to be far less accurate than the other change detection results. Therefore, the volume estimates produced by these change detection results only provide a general idea of the actual volume changes that occurred after July 7th.

Additionally, the fact that the GCPs and the photo surveys were in separate but very similar local coordinate systems due to the fact that the PPP errors were not propagated through the workflow creates an issue surrounding the georeferencing and coregistration of the datasets. However, because the PPK and PPP errors of all surveys were no larger than 10 cm, the same GCPs were used in for processing each survey, and the data was aggregated to a 1 meter resolution before producing the final results, this issue was avoided. This is because the PPP uncertainties that were not propagated throughout the workflow are an order of magnitude smaller than the final aggregation of the data, and therefore propagating the PPP errors in the x and y directions would have had a negligible effect. In addition, using the same GCPs for processing each survey insured that each survey was tied to the same local coordinate system and therefore propagating the PPP errors in the z direction would have had a negligible effect.

There are also limitations to the information that can be extracted from the results of the PyTrx analysis. Because there are no in situ measurements of debris tongue movement and all measurements were calculated remotely, it is next to impossible to independently validate this data. The current method is to process data from multiple cameras and use the agreement between the data sets as well as manual inspection of the input data to validate observed movement. However, with only two cameras as a proof of concept, this method is not entirely robust, and the addition of more cameras will increase the strength of these results. The data

produced is also noisy and the filtering workflow can be improved to extract a signal from the noise generated from poorly georeferenced images or incorrectly matched key-points within the PyTrx workflow.

These findings are also limited to the type of retrogressive thaw slump that was examined in this study. Slump CRB is a highly-active medium-sized retrogressive thaw slump whose debris tongue behaviour is being described in this work. These findings have the ability to provide insight into the behaviour of other retrogressive thaw slumps. However, these features are incredibly diverse in both size, and activity. Therefore, these findings may lose validity as the characteristics of another slump deviate from those of CRB.

8 Conclusion

The aim of this thesis was to quantitatively investigate the movement and deposition of a debris tongue belonging to a highly-active medium-sized retrogressive thaw slump at the daily and monthly time scales and metre-level spatial scale over the course of one thaw season. This was achieved by answering two research questions each supported by a technical objective which contribute to a deeper understanding of retrogressive thaw slump debris tongue movement and deposition.

This thesis showed that in this case the debris tongue material deposited in previous years does not move or change. This was done using the M3C2-PM algorithm to perform the change detection analysis which resulted in LoD value ranging from 0.11 m to 0.24 m. Considering the topographic change resulting from debris tongue movement is often an order of magnitude larger than the maximum LoD value obtained, it can be confidently said that there was no movement or change of the previously deposited material.

This thesis also showed that the debris tongue movement and deposition can be described by two development stages. The early season development stage where the debris tongue moves gradually as a pancake-like feature. And the late season development stage where pulse-like flow events rapidly transport new material downslope following the path of least resistance. These events account for the majority of debris tongue material deposited during the entire thaw season and transport material at rates up to 1 m/hour. With the ability to extract quantitative information from the time-lapse camera data as well as the aerial surveys this work builds off the current knowledge and is able to more fully describe the development stages of debris tongue movement.

This provides a new understanding on how retrogressive thaw slump debris tongues develop over the course of a thaw season which can inform future research. Future work could include expanding on the PyTrx case study to include the data collected by all of the SPi Cams to produce a debris tongue velocity dataset with precision estimates. The success of PyTrx analysis also sets the stage for a fully quantitative study that builds off both this work and the work of Kokelj et al. (2015). This work also highlights the benefit of using the M3C2-PM method to calculate topographic change and can serve as a template for how this can be operationalized. Future research can also use these findings as the basis for developing numerical models and advanced early warning systems for retrogressive thaw slumps that pose a significant threat to infrastructure, such as slump CRB.

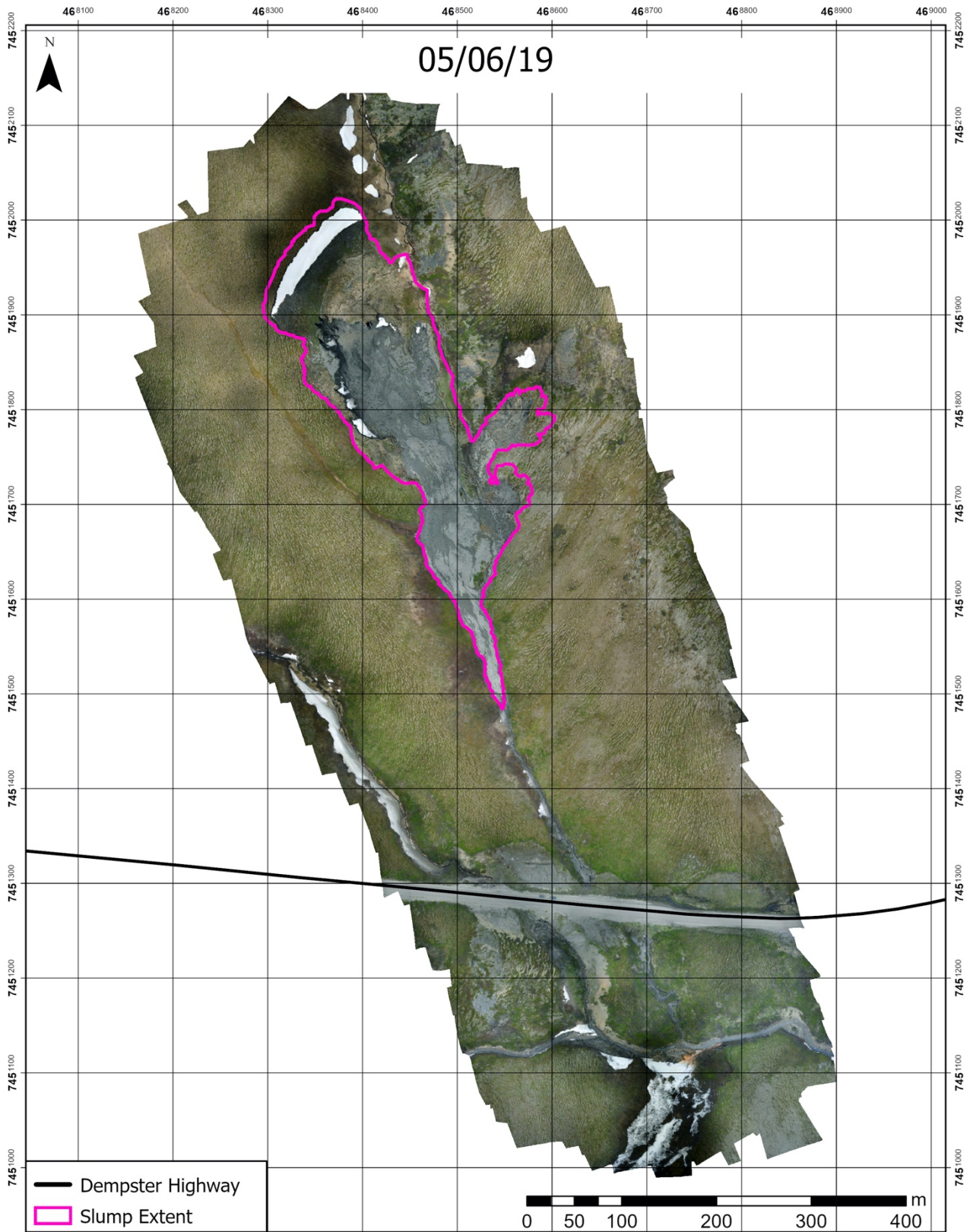
References

- Armstrong, L., Lacelle, D., Fraser, R. H., Kokelj, S. V., & Knudby, A. (2018). Thaw slump activity measured using stationary cameras in time-lapse and structure-from-motion. *Arctic Science*, 4(4), 1–18. <https://doi.org/10.1139/as-2018-0016>
- Bernard, T. G., Lague, D., & Steer, P. (in review 2020). Beyond 2D inventories: synoptic 3D landslide volume calculation from repeat LiDAR data. *Earth Surface Dynamics Discussion [Preprint]*, c, 1–28.
- Burn, C. R. (2000). The thermal regime of a retrogressive thaw slump near Mayo, Yukon Territory. *Canadian Journal of Earth Sciences*, 37(7), 967–981. <https://doi.org/10.1139/e00-017>
- Burn, C. R., & Lewkowicz, A. G. (1990). Canadian landform examples - 17 Retrogressive thaw slumps. *Canadian Geographer*, 34(3), 273–276. <https://doi.org/10.1111/j.1541-0064.1990.tb01092.x>
- Duk-Rodkin, A., & Hughes, O. L. (1992). *Surficial geology, Fort McPherson - Bell River, Yukon - Northwest Territories* (p. Map 1745A). Geological Survey of Canada. <https://doi.org/10.4095/183998>
- Environment Canada. (2019). *Fort McPherson 1981-2010 Climate Normals*. https://climate.weather.gc.ca/climate_normals/results_1981_2010_e.html?searchType=stnName&txtStationName=Fort+McPherson&searchMethod=contains&txtCentralLatMin=0&txtCentralLatSec=0&txtCentralLongMin=0&txtCentralLongSec=0&stnID=1648&dispBack=1
- European Space Agency. (n.d.). *Navipedia*. Retrieved July 23, 2020, from https://gssc.esa.int/navipedia/index.php/Main_Page
- Heginbottom, J. A., Dubreuil, M. H., & Harker, P. T. (1995). Permafrost Map of Canada. In *National Atlas of Canada* (p. MCR 4177). <https://doi.org/10.4095/294672>
- How, P., Hulton, N. R. J., & Buie, L. (2018). PyTrx: A Python toolbox for deriving velocities, surface areas and line measurements from oblique imagery in glacial environments. *Geoscientific Instrumentation, Methods and Data Systems Discussions*, July, 1–26. <https://doi.org/10.5194/gi-2018-28>
- How, P., Hulton, N. R. J., Buie, L., & Benn, D. I. (2020). PyTrx: A Python-based monoscopic terrestrial photogrammetry toolset for glaciology. *Frontiers in Earth Science*, 8(February), 1–17. <https://doi.org/10.3389/feart.2020.00021>
- Hugenholtz, C., Walker, J., Kucharczyk, M., Myshak, S., Brown, O., Nesbit, P., & Barchyn, T. (2016). Spatial accuracy of UAV-derived orthoimagery and topography: Comparing photogrammetric models processed with direct georeferencing and ground control points. *Geomatica*, 70(1), 21–30. <https://doi.org/10.5623/cig2016-102>
- IPCC. (2019). *IPCC special report on the ocean and cryosphere in a changing climate* (H.-O. Pörtner, D. C. Roberts, V. Masson-Delmotte, P. Zhai, M. Tignor, E. Poloczanska, K. Mintenbeck, A. Alegría, M. Nicolai, A. Okem, J. Petzold, B. Rama, & N. M. Weyer (eds.); Issue September). <https://doi.org/https://www.ipcc.ch/report/srocc/>
- James, M. R., Robson, S., & Smith, M. W. (2017). 3-D uncertainty-based topographic change detection with structure-from-motion photogrammetry: precision maps for ground control and directly georeferenced surveys. *Earth Surface Processes and Landforms*, 42(12), 1769–1788. <https://doi.org/10.1002/esp.4125>
- Kokelj, S. V., & Jorgenson, M. T. (2013). Advances in thermokarst research. *Permafrost and Periglacial Processes*, 24(2), 108–119. <https://doi.org/10.1002/ppp.1779>
- Kokelj, S. V., Lacelle, D., Lantz, T. C., Tunnicliffe, J., Malone, L., Clark, I. D., & Chin, K. S.

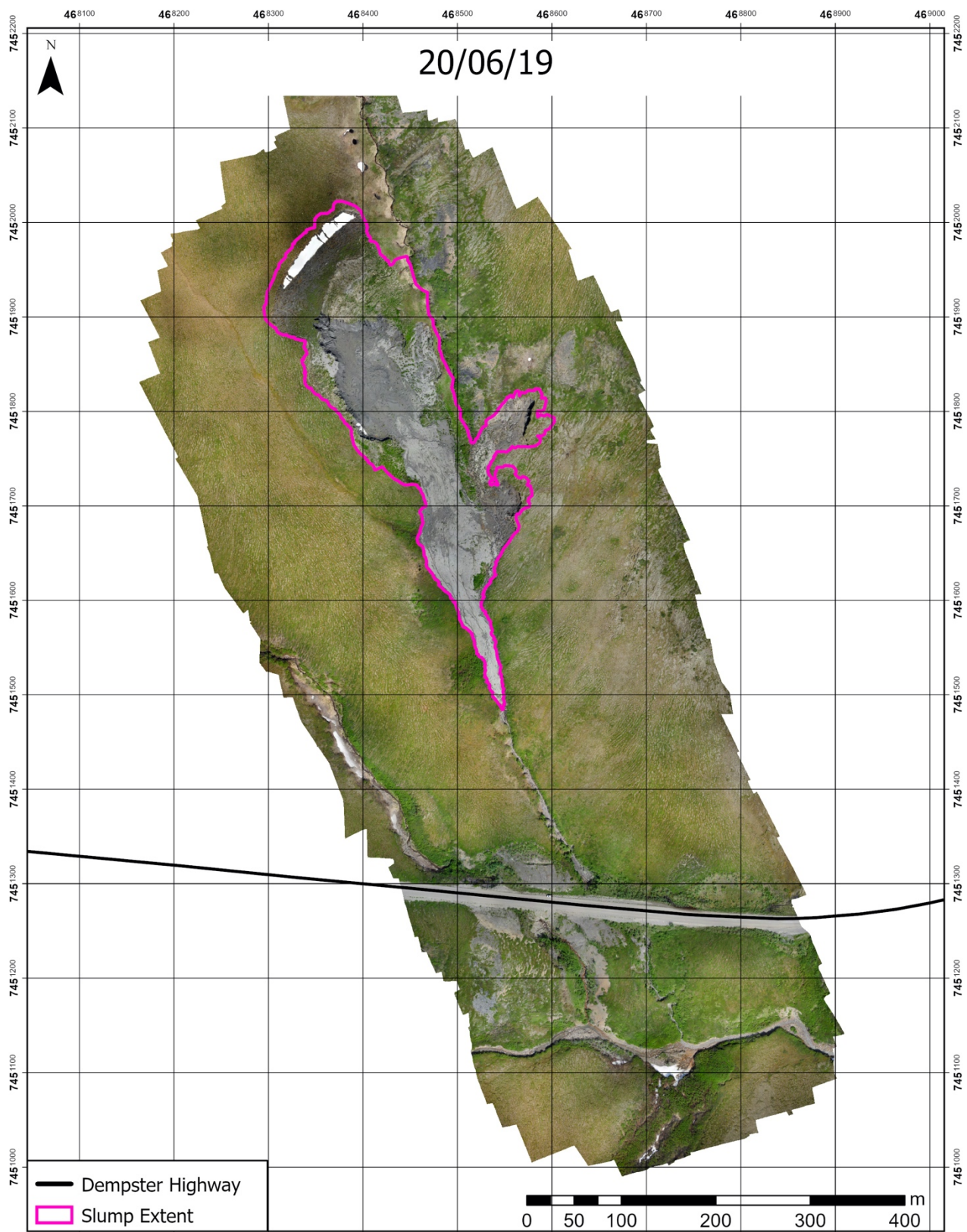
- (2013). Thawing of massive ground ice in mega slumps drives increases in stream sediment and solute flux across a range of watershed scales. *Journal of Geophysical Research: Earth Surface*, 118(2), 681–692. <https://doi.org/10.1002/jgrf.20063>
- Kokelj, S. V., Lantz, T. C., Kanigan, J., Smith, S. L., & Coutts, R. (2009). Origin and polycyclic behaviour of tundra thaw slumps, Mackenzie Delta region, Northwest Territories, Canada. *Permafrost and Periglacial Processes*, 20(2), 173–184. <https://doi.org/10.1002/ppp.642>
- Kokelj, S. V., Tunnicliffe, J., Lacelle, D., Lantz, T. C., Chin, K. S., & Fraser, R. H. (2015). Increased precipitation drives mega slump development and destabilization of ice-rich permafrost terrain, northwestern Canada. *Global and Planetary Change*, 129, 56–68. <https://doi.org/10.1016/j.gloplacha.2015.02.008>
- Lacelle, D., Bjornson, J., & Lauriol, B. (2010). Climatic and geomorphic factors affecting contemporary (1950-2004) activity of retrogressive thaw slumps on the Aklavik Plateau, Richardson Mountains, NWT, Canada. *Permafrost and Periglacial Processes*, 21(1), 1–15. <https://doi.org/10.1002/ppp.666>
- Lacelle, D., Brooker, A., Fraser, R. H., & Kokelj, S. V. (2015). Distribution and growth of thaw slumps in the Richardson Mountains–Peel Plateau region, northwestern Canada. *Geomorphology*, 235, 40–51. <https://doi.org/10.1016/j.geomorph.2015.01.024>
- Lague, D., Brodu, N., & Leroux, J. (2013). Accurate 3D comparison of complex topography with terrestrial laser scanner: Application to the Rangitikei canyon (N-Z). *ISPRS Journal of Photogrammetry and Remote Sensing*, 82, 10–26. <https://doi.org/10.1016/j.isprsjprs.2013.04.009>
- Lantz, T. C., & Kokelj, S. V. (2008). Increasing rates of retrogressive thaw slump activity in the Mackenzie Delta region, N.W.T., Canada. *Geophysical Research Letters*, 35(6), L06502. <https://doi.org/10.1029/2007GL032433>
- Lewkowicz, A. G. (1987). Headwall retreat of ground-ice slumps, Banks Island, Northwest Territories. *Canadian Journal of Earth Sciences*, 24(6), 1077–1085. <https://doi.org/10.1139/e87-105>
- Longuet-Higgins, H. C. (1987). A computer algorithm for reconstructing a scene from two projections. In *Readings in Computer Vision* (pp. 61–62). <https://doi.org/10.1016/b978-0-08-051581-6.50012-x>
- Lucieer, A., de Jong, S. M., & Turner, D. (2014). Mapping landslide displacements using structure-from-motion (SfM) and image correlation of multi-temporal UAV photography. *Progress in Physical Geography*, 38(1), 97–116. <https://doi.org/10.1177/0309133313515293>
- Mallalieu, J., Carrivick, J. L., Quincey, D. J., Smith, M. W., & James, W. H. M. (2017). An integrated structure-from-motion and time-lapse technique for quantifying ice-margin dynamics. *Journal of Glaciology*, 63(242), 937–949. <https://doi.org/10.1017/jog.2017.48>
- Malone, L., Lacelle, D., Kokelj, S. V., & Clark, I. D. (2013). Impacts of hillslope thaw slumps on the geochemistry of permafrost catchments (Stony Creek watershed, NWT, Canada). *Chemical Geology*, 356, 38–49. <https://doi.org/10.1016/j.chemgeo.2013.07.010>
- Mancini, F., Dubbini, M., Gattelli, M., Stecchi, F., Fabbri, S., & Gabbianelli, G. (2013). Using unmanned aerial vehicles (UAV) for high-resolution reconstruction of topography: The structure from motion approach on coastal environments. *Remote Sensing*, 5(12), 6880–6898. <https://doi.org/10.3390/rs5126880>
- MikroElektronika. (n.d.). *GPS Click - Breakout Board for u-blox LEA-6s*. Retrieved March 30, 2019, from <https://www.mikroe.com/gps-click>
- Natural Resources Canada. (n.d.). *Geodetic tools and applications*. Retrieved July 23, 2020, from <https://www.nrcan.gc.ca/maps-tools-publications/tools/geodetic-reference-systems-tools/tools-applications/10925>

- Norris, D. K. (1985). *Geology of the Northern Yukon and Northwestern District of Mackenzie* (p. "A" Series Map 1581A). Geological Survey of Canada. <https://doi.org/10.4095/120537>
- O'Neill, H. B., & Burn, C. R. (2017). Impacts of variations in snow cover on permafrost stability, including simulated snow management, Dempster Highway, Peel Plateau, Northwest Territories. *Arctic Science*, 3(2), 150–178. <https://doi.org/10.1139/as-2016-0036>
- O'Neill, H. B., Burn, C. R., Kokelj, S. V., & Lantz, T. C. (2015). "Warm" tundra: atmospheric and near-surface ground temperature inversions Across an alpine treeline in continuous permafrost, Western Arctic, Canada. *Permafrost and Periglacial Processes*, 26(2), 103–118. <https://doi.org/10.1002/ppp.1838>
- O'Neill, H. Brendan, Wolfe, S. A., & Duchesne, C. (2019). New ground ice maps for Canada using a paleogeographic modelling approach. *Cryosphere*, 13(3), 753–773. <https://doi.org/10.5194/tc-13-753-2019>
- SenseFly. (n.d.). *GCPs vs RTK vs PPK: When to use what and why*. Retrieved July 23, 2020, from <https://waypoint.sensefly.com/gcps-rtk-ppk-when-what-why/>
- Smith, M. W., Carrivick, J. L., & Quincey, D. J. (2015). Structure from motion photogrammetry in physical geography. *Progress in Physical Geography*, 40(2), 247–275. <https://doi.org/10.1177/0309133315615805>
- Swanson, D. K., & Nolan, M. (2018). Growth of retrogressive thaw slumps in the Noatak Valley, Alaska, 2010–2016, measured by airborne photogrammetry. *Remote Sensing*, 10(7), 2010–2016. <https://doi.org/10.3390/rs10070983>
- Turner, D., Lucieer, A., & de Jong, S. M. (2015). Time series analysis of landslide dynamics using an Unmanned Aerial Vehicle (UAV). *Remote Sensing*, 7(2), 1736–1757. <https://doi.org/10.3390/rs70201736>
- van der Sluijs, J., Kokelj, S. V., Fraser, R. H., Tunnicliffe, J., & Lacelle, D. (2018). Permafrost terrain dynamics and infrastructure impacts revealed by UAV photogrammetry and thermal imaging. *Remote Sensing*, 10(11), 1734. <https://doi.org/10.3390/rs10111734>
- Wang, B., Paudel, B., & Li, H. (2016). Behaviour of retrogressive thaw slumps in northern Canada—three-year monitoring results from 18 sites. *Landslides*, 13(1), 1–8. <https://doi.org/10.1007/s10346-014-0549-y>
- Westoby, M. J., Brasington, J., Glasser, N. F., Hambrey, M. J., & Reynolds, J. M. (2012). "Structure-from-motion" photogrammetry: A low-cost, effective tool for geoscience applications. *Geomorphology*, 179, 300–314. <https://doi.org/10.1016/j.geomorph.2012.08.021>
- Wingtra. (n.d.). *What's the difference between PPK and RTK drones, and which one is better?* Retrieved July 23, 2020, from <https://wingtra.com/ppk-drones-vs-rtk-drones/>

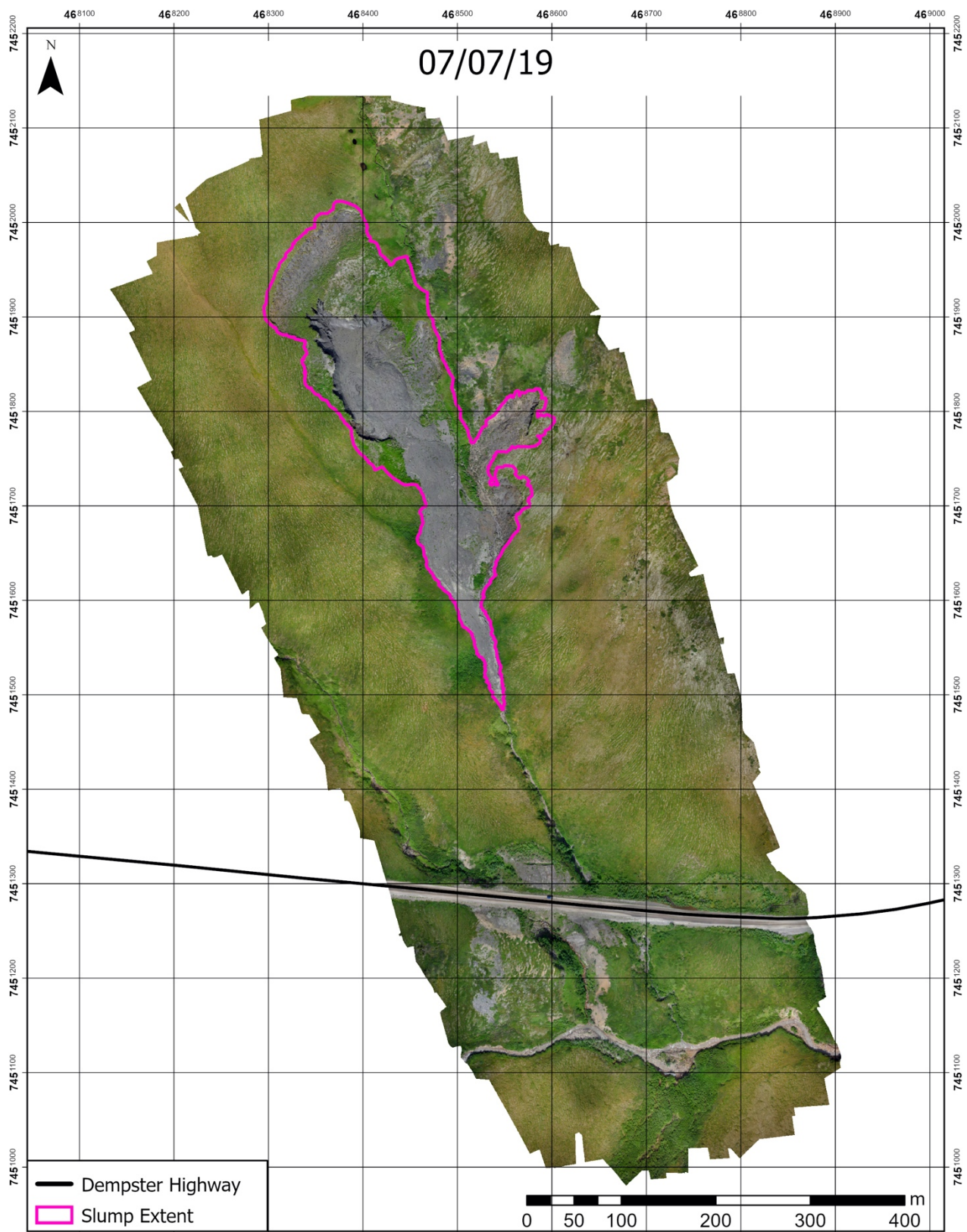
Appendix A: Additional Figures



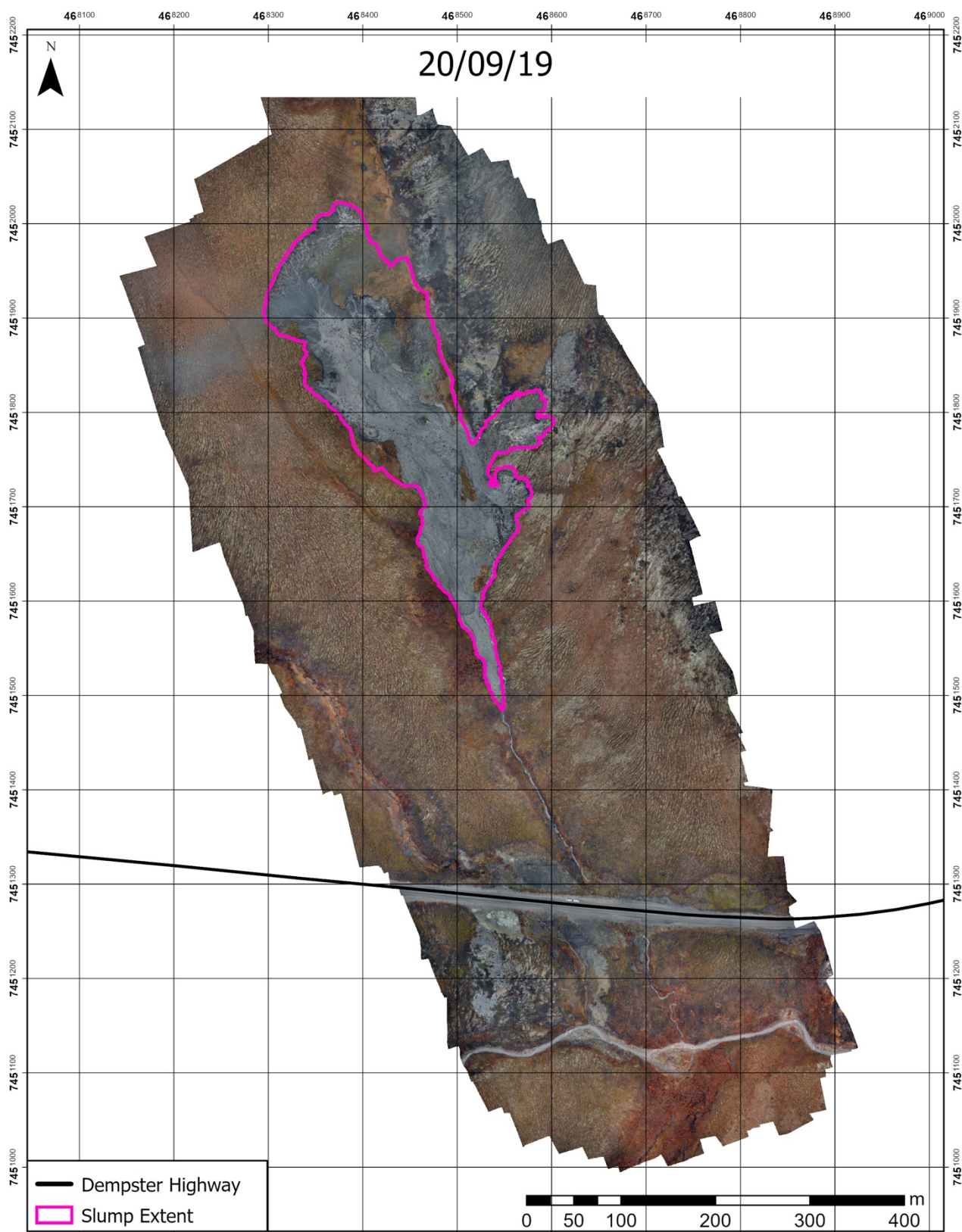
A 1: Orthoimage of slump CRB generated from the June 5th aerial survey.



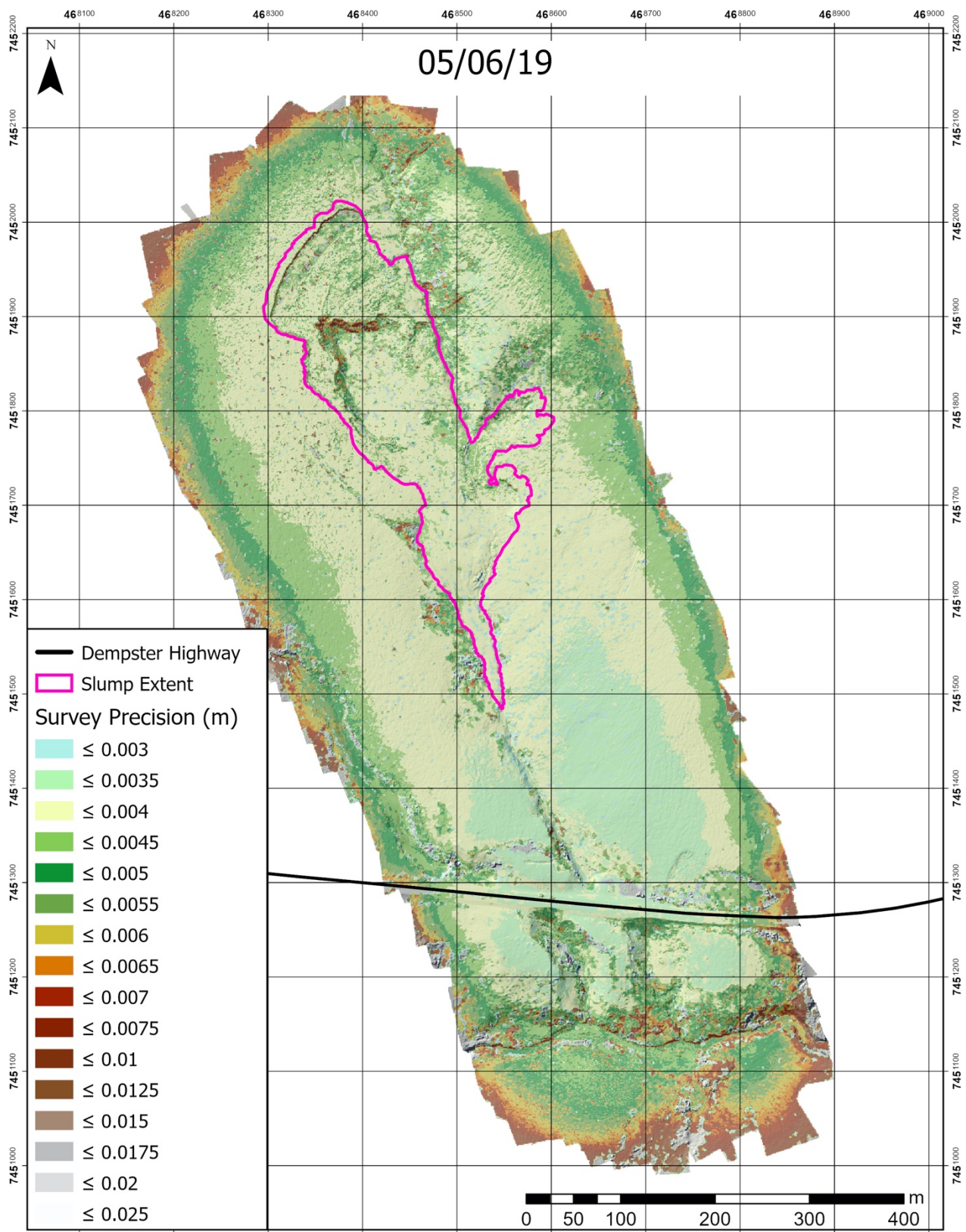
A 2: Orthoimage of slump CRB generated from the June 20th aerial survey.



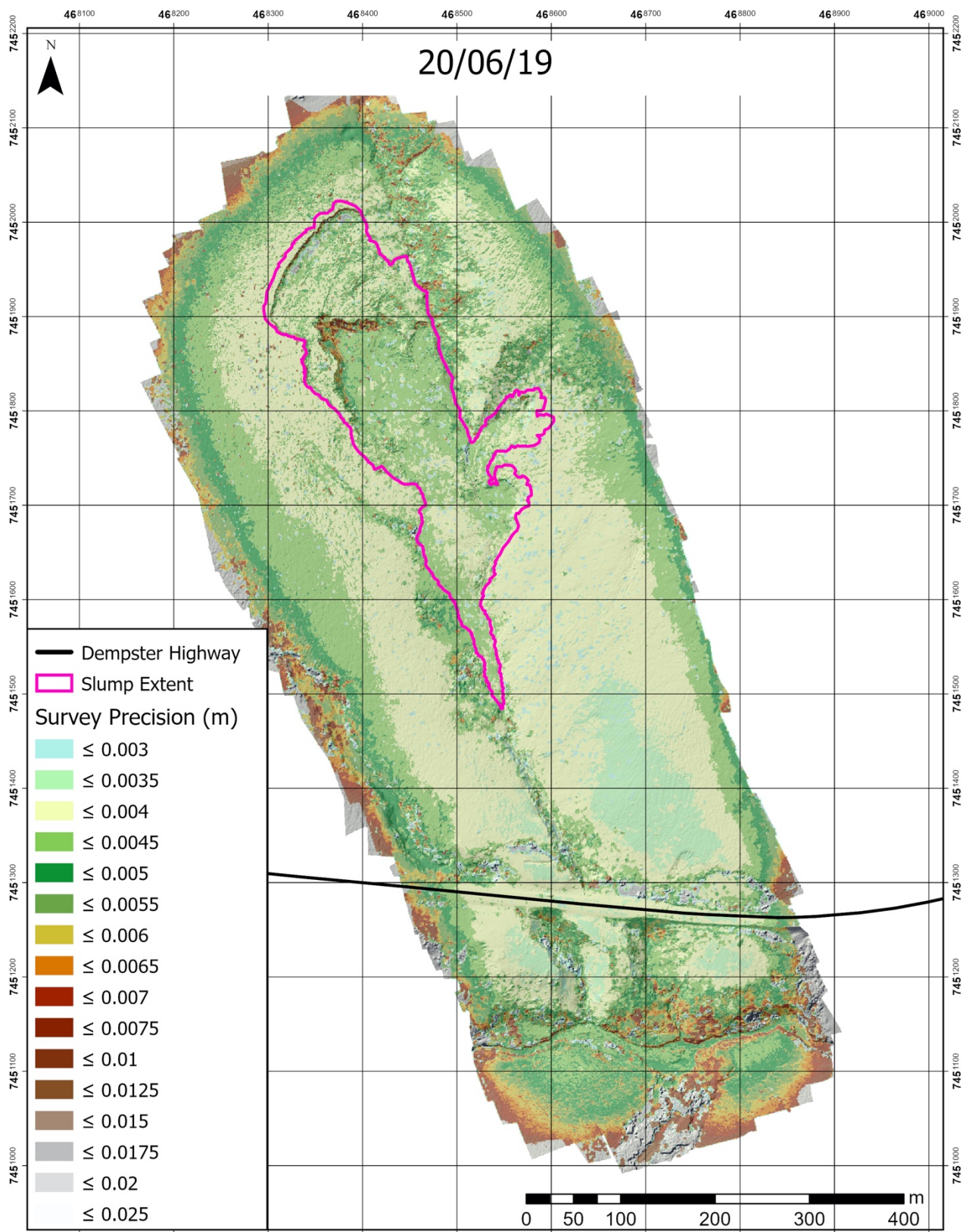
A 3: Orthoimage of slump CRB generated from the August 7th aerial survey.



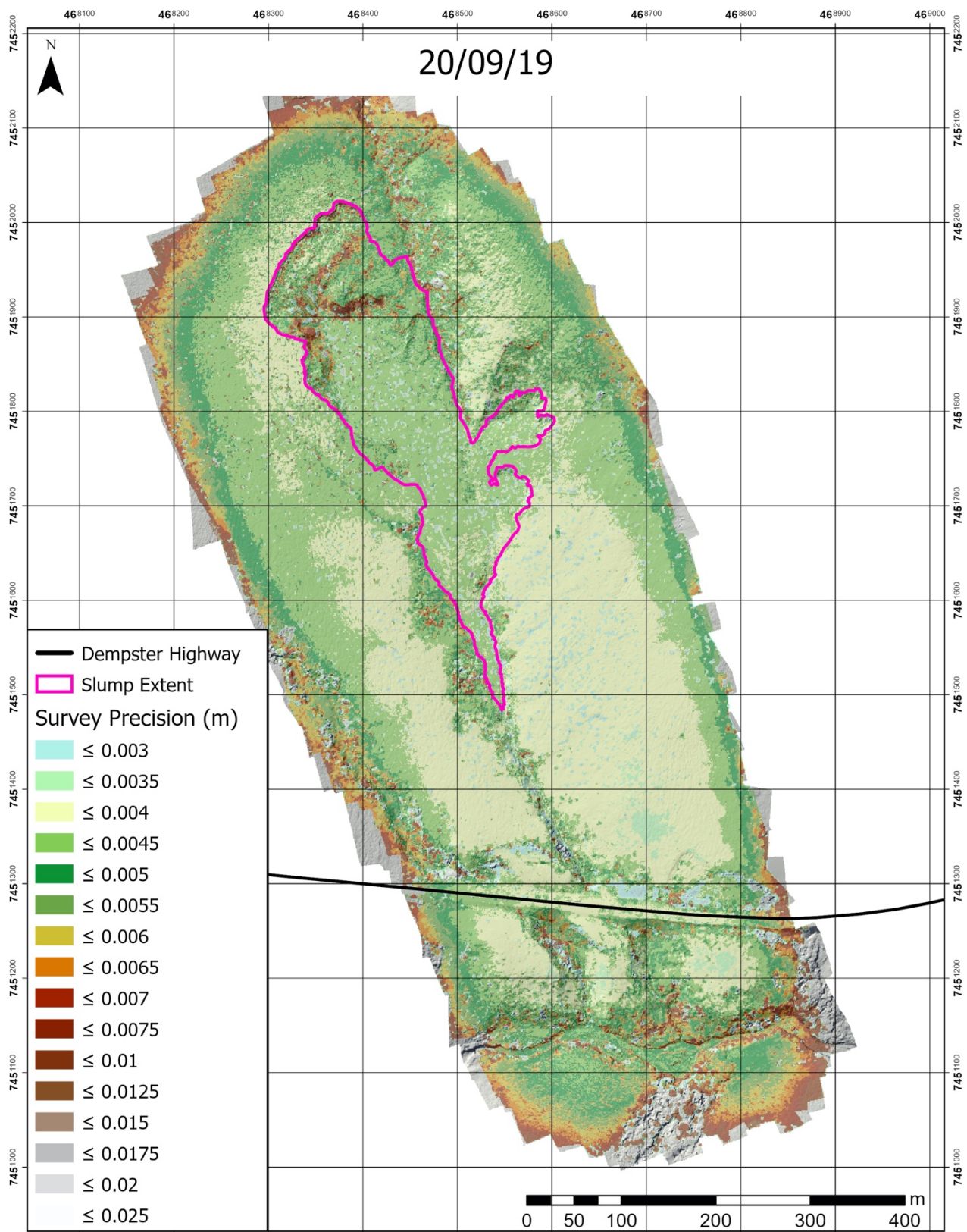
A 4: Orthoimage of slump CRB generated from the June 20th aerial survey.



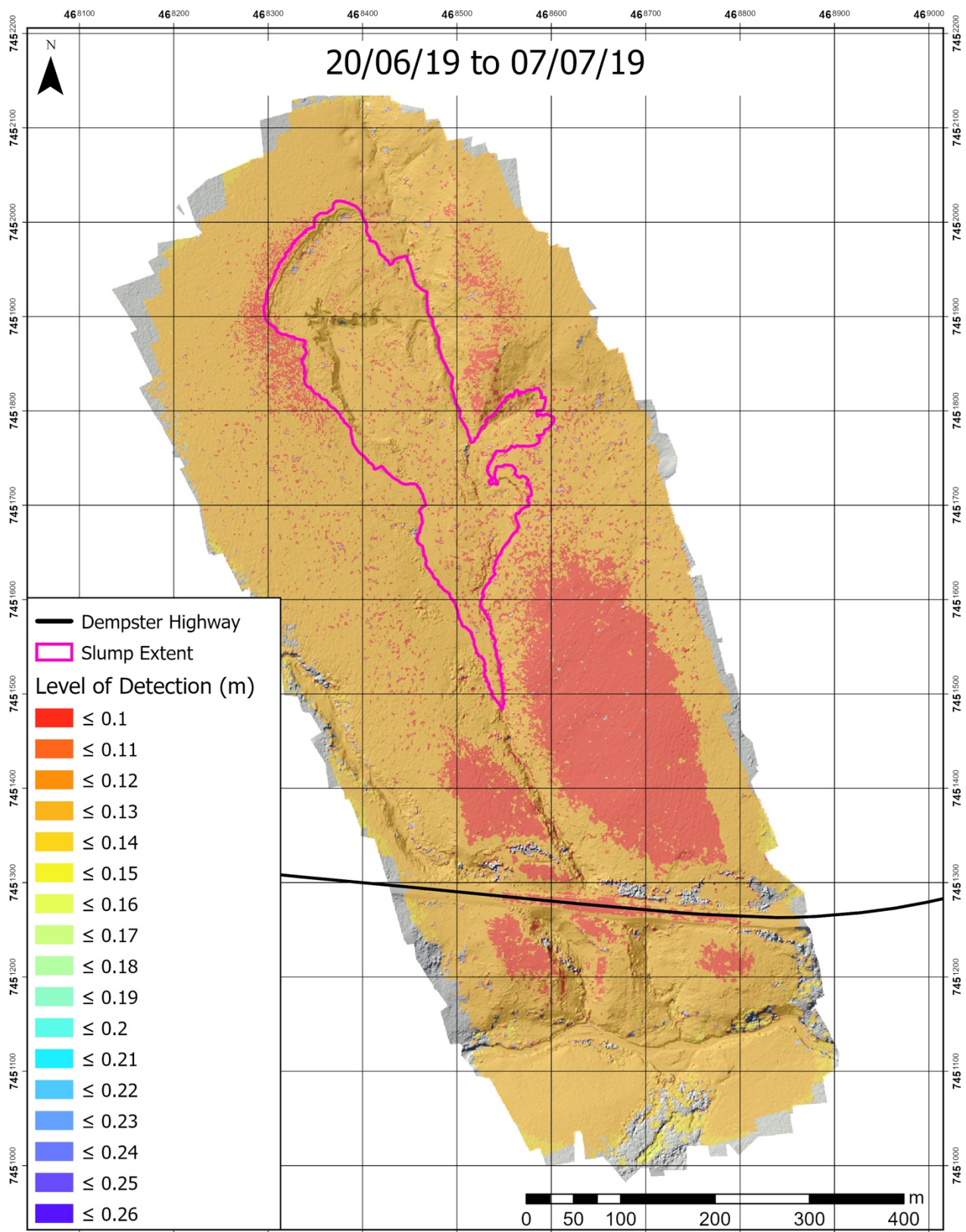
A 5: Precision map generated from the Monte Carlo analysis of the June 5th survey.



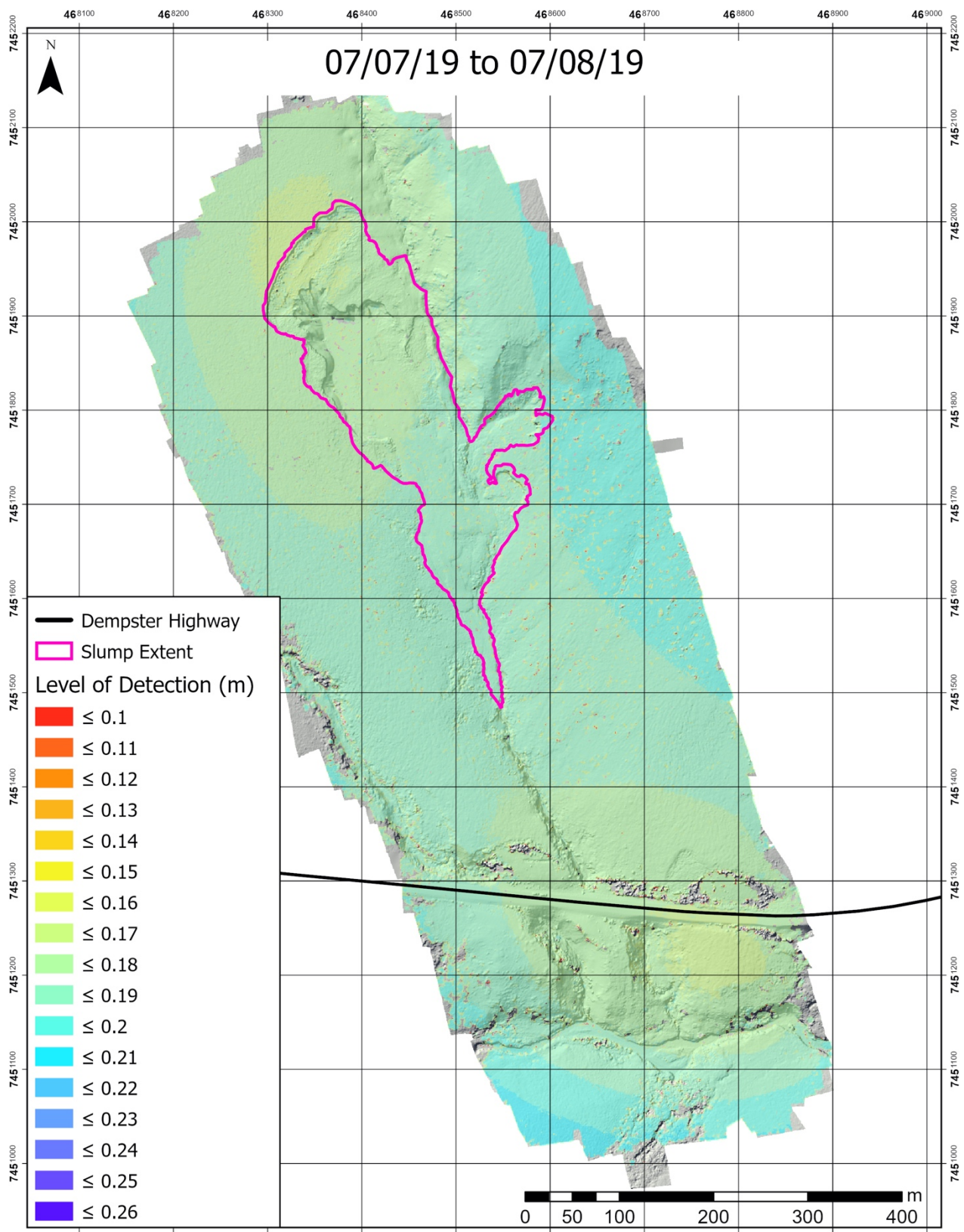
A 6: Precision map generated from the Monte Carlo analysis of the June 20th survey.



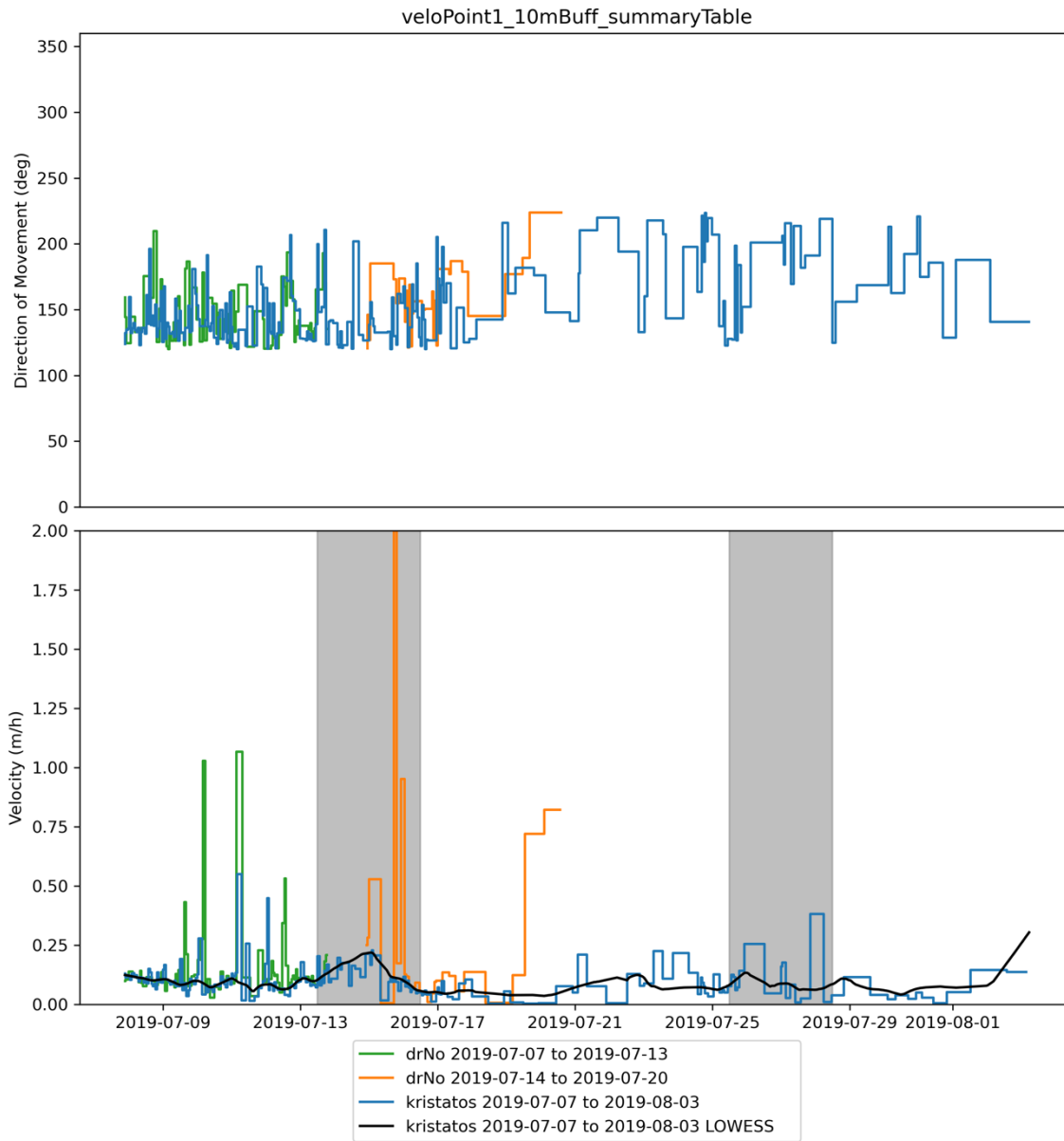
A 7: Precision map generated from the Monte Carlo analysis of the September 20th survey.



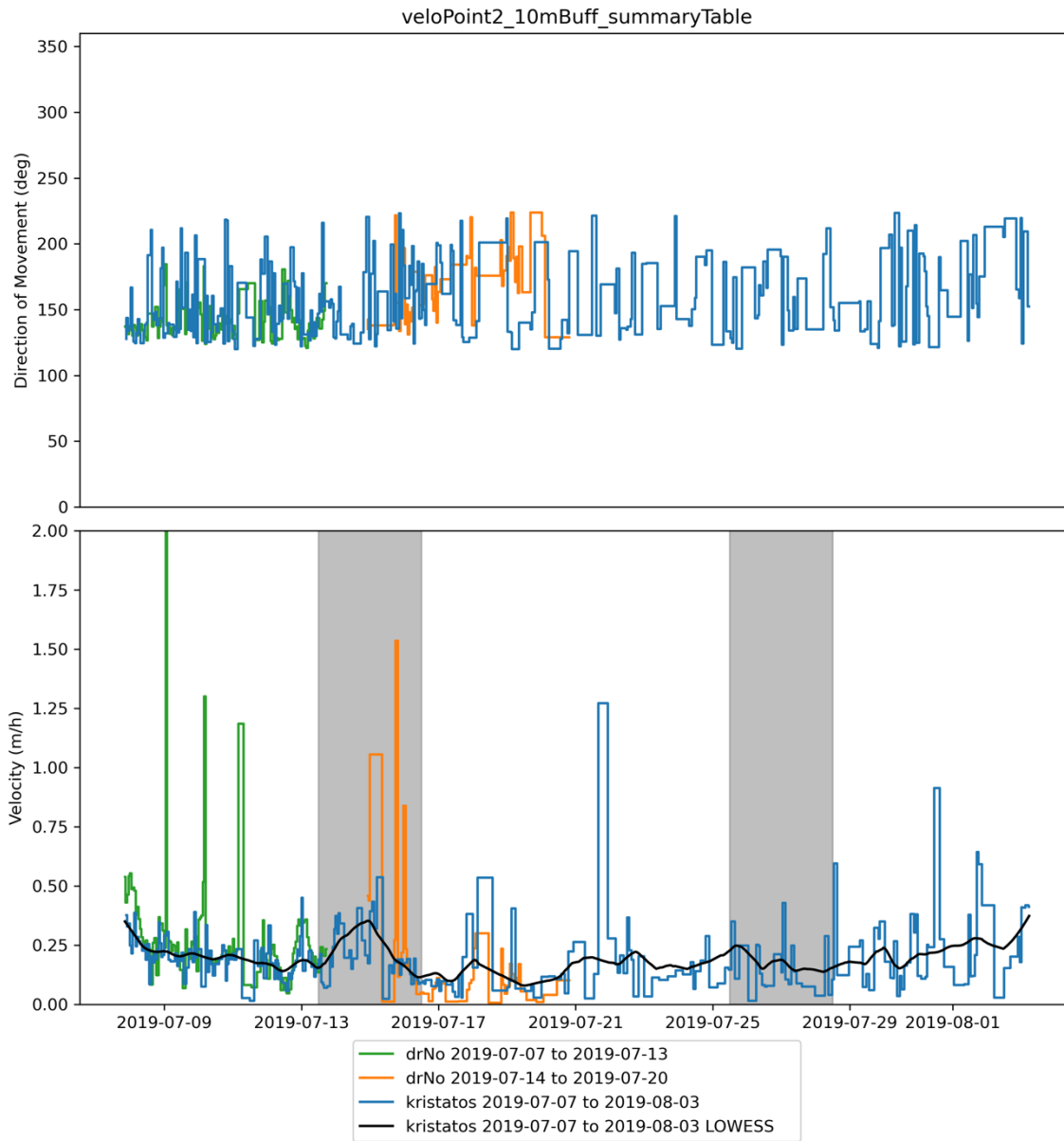
A 8: Level of detection map for the June 20th and July 7th aerial survey change detection pair.



A 9: Level of detection map for the July 7th and August 7th aerial survey change detection pair.



A 10: The velocity and direction of movement measured by PyTrx that occurred in summary zone one.



A 11: The velocity and direction of movement measured by PyTrx that occurred in summary zone two.

Appendix B: SPi Cam Photos



B 1: Image taken by Kristatos on July 7th, 2019 at 21:30. This shows the initial state of the debris tongue when SPi Cam monitoring began.



B 2: Image taken by Kristatos on July 11th, 2019 at 04:30. Note the advance of the debris tongue compared to the above image.



B 3: Image taken by Kristatos on July 11th, 2019 at 12:30. The low visibility indicates a dense rainstorm and fog covered the landscape at this time.



B 4: Image taken by Kristatos on July 13th, 2019 at 05:30. This image is used as a reference to compare to the following image.



B 5: Image taken by Kristatos on July 16th, 2019 at 13:30. Note the large advance of the debris tongue in comparison to the previous image.



B 6: Image taken by Kristatos on July 21st, 2019 at 19:30. This image is obscured by water on the camera lens indicating a rainfall event occurred.



B 7: Image taken by Kristatos on July 25th, 2019 at 12:30. Note how the debris tongue has advanced in comparison to Appendix B 6.



B 8: Image taken by Kristatos on July 26th, 2019 at 18:30. Note the advance of the debris tongue towards the camera in comparison to the previous image.



B 9: Image taken by Dr No on August 8th, 2019 at 22:30. This image is used as a reference for the following image.



B 10: Image taken by Dr No on August 10th, 2019 at 16:30. Note the advance of the debris tongue downslope and towards the camera in comparison to the previous image. In particular note the vegetated mound almost buried in the lower right corner.



B 11: Image taken by Dr No on August 16th, 2019 at 18:30. Note the advance of the debris tongue downslope compared to the previous image.